Synthesis and Characterization of Doping Modulated Graphene-based materials for Device applications

A thesis submitted

by

Jai Shree Bhardwaj
Roll No: 176151006

In partial fulfillment of the requirement for the award of the degree of Doctor of Philosophy

School of Energy Science and Engineering
Indian Institute of Technology, Guwahati
Guwahati – 781 039, Assam, India

July 2025

DECLARATION

The work contained in this thesis entitled **"Synthesis and Characterization of Doping Modulated Graphene-based materials for Device applications"** has been carried out by me under the supervision of Dr. Pratima Agarwal, Professor, Department of Physics, Indian Institute of Technology, Guwahati, Assam, India. This thesis does not contain any materials previously submitted for the award of any degree or diploma.

Date:

Jai Shree Bhardwaj
Roll No: 176151006
School of Energy Science and Engineering
Indian Institute of Technology Guwahati
Guwahati-781039, Assam, India

भारतीय प्रौद्योगिकी संस्थान गुवाहाटी
Indian Institute of Technology Guwahati
North Guwahati, Guwahati
PIN- 781 039, Assam State, INDIA
Phone: +91 361 2583000 Extn 2702, 2582702
Fax: +91 361 2690 762 (Institute), 2582749 (Department)

Dr. Pratima Agarwal
Professor
Department of Physics
E-mail:pratima@iitg.ernet.in

Dated: July 29, 2025

Certificate

This is certified that the work contained in this thesis entitled "**Synthesis and Characterization of Doping Modulated Graphene Based Materials for Device Applications"** submitted by **Ms. Jai Shree Bhardwaj**, a Ph. D. student at School of Energy Science and Engineering, Indian Institute of Technology, Guwahati, Assam, India, for the award of the degree of Doctor of Philosophy has been carried out under my supervision. This work has not been submitted elsewhere for the award of any degree or diploma.

Pratima Agarwal

(Dr. Pratima Agarwal)

Dedicated

to

my grandfather (late)

&

My parents, husband, siblings and entire family

Acknowledgement

I sincerely thank my PhD supervisor, Prof. Pratima Agarwal, for giving me the opportunity to pursue my doctoral research under her guidance. Her constant support, insightful discussions, and unwavering encouragement have been invaluable throughout my journey. From fundamental concepts to device physics and experimental designs, she has played a pivotal role in shaping my understanding. I am deeply grateful for the numerous learning opportunities she provided, which have greatly contributed to the successful completion of this work.

I extend my gratitude to my doctoral committee members Prof. Alika Khare (Chairman), Dr. Gaurav Trivedi, Dr. Harsh Chaturvedi (late), and Dr. Pankaj Kalita for their regular review of my research work, constructive suggestions, and valuable discussions at various stages of my journey. I also express my sincere thanks to the present and former Heads of the School of Energy Science and Engineering and the Department of Physics for their encouragement and for granting me access to departmental facilities throughout my research. I am also thankful to Prof. Mahua De (late), Prof. Pankaj Kalita, Prof. V Katiyar, and Prof. PSG Pattader for the guidance and exposure during coursework. My thanks also go to all faculty members and office staff of the School of Energy Science and Engineering.

I would like to acknowledge my lab seniors Dr. Ramakrishna Madaka, Dr. Asha Yadav, Dr. Venkanna Kanneboina, Dr. Pilik Basumatary, Dr. Juhi Kumari, Dr. Manvendra Singh Gangwar, Dr. Himangshu Deka, and my current and past labmates Mr. Anterdipan Singh, Mr. Rahul, Mr. Tulsi, Mr. Ashish, Ms. Keerthana, Mr. Bishwajeet, Mr. Vivek Ghritlahre, Dr. Shubhangi Bhardwaj, Dr. Niharika Gogoi, Mr. Ankit Kumar Singh, Mr. Gaurav Singh, Mr. Rohan Ghosh, Ms. Vaishnavi Chouksey, Mr. Dharmendra Singh Samota, Mr. Mahipal Singh Rathore, Ms. Kaushalya Kumari, Mr. Kazuki Tanaka, Mr. Nisarg Vyas, Mr. Jay Kumawat,

Mr. Yogesh, Ms. Nikita, Ms. Lakshmi for providing a congenial environment and supporting me at various stages of my research.

I am thankful to CIF, IIT Guwahati for access to their facilities, and to the technical officers Mr. Madhurjya Borah, Dr. Sidananda Sarma, Mr. Chandan Borgohain, and Mr. Kh. Kesho Singh for their assistance.

I feel fortunate to have had the support of my friends Mr. Abhishek, Dr. Chandan, Dr. Dipanwita, Dr. Shweta, Dr. Roushni, Dr. Sashmita, Dr. Prajna, Dr. Sumit from IIT Guwahati, as well as Ms. Neha, Ms. Amrapali, Ms. Astha, Ms. Kavisha, Ms. Sonam, Dr. Ashutosh, Mr. Vivek, and Mr. Nishant, who stood by me during my research journey.

I am grateful to all the research scholars of the School of Energy Science and Engineering and the Department of Physics for their help and for the wonderful moments we shared.

Last but certainly not least, I thank my family my father Mr. Kumar Sundram Bhardwaj, mother Mrs. Kanchan Bhardwaj, father-in-law Mr. Shaligram Chaudhary, mother-in-law Mrs. Subodh Kumari, husband Mr. Rishabh Raj, sisters Dr. Smita Bhardwaj and Ms. Rashmi Bhardwaj, brother Mr. Awanish Bhardwaj, brothers-in-law Mr. Pallav Kumar and Mr. Vinay Mishra, sister-in-law Ms. Arti, to my 1-month-old little nephew and my entire family who stood by me through all my struggles. Their unwavering support, inspiration, and motivation have been the backbone of my doctoral journey.

Finally, I thank God for all His blessings, without which nothing would have been possible.

Jai Shree Bhardwaj

IIT Guwahati

PREFACE

Graphene, a two-dimensional material composed of a single layer of carbon atoms arranged in a hexagonal lattice, has attracted significant research attention owing to its extraordinary electrical, mechanical, and optical properties. Despite these exceptional features, certain inherent limitations, such as the absence of a bandgap and challenges in tuning its electronic properties, restrict its direct application in devices like supercapacitors and photovoltaics. The present research focuses on addressing these challenges by developing graphene-based materials with controlled doping, and exploring their potential for device applications, specifically in supercapacitors and graphene-silicon heterojunction solar cells.

One effective approach employed in this study involves the synthesis of graphene oxide (GO) from graphite, followed by its reduction to reduced graphene oxide (rGO), which exhibits properties comparable to pristine graphene. To further enhance its electronic properties, stable p-type and n-type doping has been achieved through heteroatom substitution in GO and rGO. This method allows modulation of the bandgap and control over carrier concentrations, which significantly improves the electrical conductivity and enables the material's application in energy devices. Particularly, boron doping in graphene-based materials has demonstrated improved charge-discharge characteristics for supercapacitor applications. Systematic studies on the structural, electrical, electrochemical, and thermal properties of these graphene-based materials have been undertaken to evaluate their suitability for various applications.

Chapter 1 presents an extensive literature review aligned with the objectives of this research. It covers the synthesis of graphene-based materials, including GO, rGO, and their boron doping via chemical methods for supercapacitor applications. It also reviews graphene growth techniques using Hot Wire Chemical Vapor Deposition (HWCVD) and Plasma Enhanced Chemical Vapor Deposition (PECVD) on nickel and silicon substrates, emphasizing the critical role of metal catalysts and the challenges in direct graphene growth on silicon for semiconductor devices. Furthermore, advancements in graphene-silicon heterojunction solar cells are discussed, identifying the research gaps addressed in this thesis.

Chapter 2 describes the experimental methodologies adopted in this research. It details the chemical routes for synthesizing graphene-based materials and the CVD systems used for graphene growth on various substrates. Additionally, this chapter outlines the characterization techniques utilized to study the structural, morphological, and electrical properties of thin films and fabricated solar cells. Chapter 3 focuses on the synthesis and characterization of

doped and undoped graphene-based materials via chemical routes. Comparative analyses of rGO produced by chemical and thermal reduction methods are presented. The bulk synthesis of boron-doped reduced graphene oxide (B-rGO) using boric acid as a doping source is also discussed. The chapter highlights the enhancement in specific capacitance and structural modifications induced by doping, supported by XRD, Raman, FETEM, FTIR, and EDAX analyses. Additionally, nitrogen-doped rGO samples were prepared, and their structural and electrical properties were evaluated. Thermal kinetics studies were conducted to understand the degradation mechanisms and stability of the prepared materials. Chapter 4 describes the growth of single and multilayer graphene films on nickel substrates by HWCVD. The influence of deposition parameters such as temperature, gas flow ratios, and deposition time on the number of graphene layers and film uniformity is systematically studied using AFM and Raman spectroscopy. The optimized films were then transferred to silicon substrates using a chemical etching process for further device fabrication. Chapter 5 reports the direct deposition of large-area, high-quality graphene on silicon substrates without metal catalysts using PECVD and HWCVD techniques. The chapter discusses the tuning of the graphene work function by controlling the number of layers through deposition parameter variation. The quality and uniformity of the films were verified using Raman, XPS, FESEM, AFM, and KPFM analyses. Fabricated graphene-silicon heterojunction solar cells exhibited an efficiency of 1%, validating the feasibility of the approach. Chapter 6 presents simulation studies of graphene-silicon heterojunction solar cells using the AFORS-HET software. The impact of varying the thickness of the intrinsic a-Si:H layer, the n-type doping concentration of graphene, and the number of graphene layers on the device performance was systematically analyzed. The optimized structure achieved a theoretical power conversion efficiency of 18.59%, with significant improvements in Voc, Jsc, and fill factor. Chapter 7 concludes the thesis by summarizing the key findings of each chapter and outlining potential directions for future research based on the outcomes of this work.

LIST OF ABBREVIATIONS AND SYMBOLS

a-Si:H	Hydrogenated amorphous silicon
AFM	Atomic force microscopy
AFORS-HET	Automat FOR Simulation of HETero-structures
APCVD	Ambient pressure chemical vapor deposition
BET	Brunauer-Emmett-Teller
B-rGO	Boron doped reduced Graphene Oxide (doping in r-GO)
CB	Conduction Band
C-C	Carbon-carbon
CNT	Carbon nanotubes
CPD	Contact potential difference
CV	Cyclic Voltammetry
DTG	Derivative Thermogravimetry
EDX	Energy dispersive x-ray
EDLC's	Electrochemical double-layer capacitors
FETEM	Field emission transmission electron microscopy
FESEM	Field emission scanning electron microscopy
FTIR	Fourier transform infrared microscopy
GHG	Greenhouse gas
GO	Graphene Oxide
HRTEM	High-Resolution Transmission Electron Microscopy
HWCVD	Hot Wire Chemical Vapor Deposition
IEA	International Energy Agency
ITO	Indium tin oxide
IPCE	Incident Photon-to-Current Efficiency
KPFM	Kelvin Probe Force Microscopy
LED	Light emitting diode
MWCNT	Multi walled CNT
N-rGO	Nitrogen doped reduced Graphene oxide
PCE	Power Conversion efficiency
PECVD	Plasma Enhanced Chemical Vapor Deposition
PV	Photovoltaic
r-BGO	Boron doped reduced Graphene Oxide (doping in GO)

r-GO	Reduced Graphene Oxide
r-GO(T)	Thermally reduced graphene oxide
r-GO(C)	Chemically reduced graphene oxide
SAED	Selected Area Electron Diffraction
SBH	Schottky barrier height
Sccm	Standard cubic centimeters per minute
SE	Spectroscopic ellipsometry
SiC	Silicon carbide
SWCNT	Single walled CNT
TCE	Transparent conductive electrode
TCO	Transparent conducting oxide
TGA	Thermogravimetric Analysis
T_s	Substrate temperature
XPS	X-ray photoelectron spectroscopy
XRD	X-ray diffraction
UV-Vis-NIR	Ultraviolet visible near infrared
VB	Valance band
VGNH	Vertical graphene nano hills
0D	0-dimensional
1D	1-dimensional
2D	2-dimensional
3D	3-dimensional
J_{sc}	Short circuit current density
V_{oc}	Open circuit voltage
FF	Fill factor
η	Efficiency
T_{max}	Maximum temperature
E_a	Activation energy
E_f	Fermi level
H	Planks constant
I_D	Intensity of the D-band
I_G	Intensity of the G-band
I_{2D}	Intensity of the 2D-band

σ	Conductivity
T	thickness of the film
K	Boltzmann constant
T	Temperature in kelvin

TABLE OF CONTENT

LIST OF FIGURES

LIST OF TABLES

Chapter 1

Introduction

1.1. The Growing Need for Renewable Energy

The global surge in energy consumption has created an urgent need for sustainable and reliable energy sources. Rapid population growth, urbanization, and industrial expansion are pushing the limits of the current fossil fuel-based energy infrastructure.[1, 2] According to the International Energy Agency (IEA), worldwide energy demand is projected to rise by more than 25% by 2040, driven primarily by emerging economies.[3] Traditionally, this demand has been met by coal, oil, and natural gas, which still dominate the global energy mix. However, these finite resources are associated with environmental degradation, rising greenhouse gas (GHG) emissions, and climate change.[4] The continued reliance on fossil fuels is contributing to global warming, melting polar ice caps, and triggering extreme weather events, threatening ecosystems and human livelihoods.[3, 5, 6]

Beyond environmental concerns, fossil fuel dependence also leads to economic volatility, with price fluctuations and geopolitical tensions over energy reserves creating instability.[6-9] These

challenges highlight the need to transition toward renewable energy sources that are both sustainable and environmentally friendly. Solar, wind, hydro, geothermal, and biomass offer cleaner alternatives that can significantly reduce carbon footprints. Among these, solar energy is particularly promising due to its abundance, accessibility, and scalability.[10, 11]

The Sun delivers approximately 173,000 terawatts (TW) of solar power to the Earth's surface at any given moment, more than 10,000 times the planet's total energy consumption.[3] With photovoltaic (PV) technology, a portion of this vast energy can be harnessed and converted into electricity. As the cost of solar panels continues to decline and their efficiency improves, solar power is becoming an increasingly viable solution for both grid-scale and off-grid energy generation.[12-14] However, the intermittency of solar energy (only generating power during daylight hours) creates a pressing need for efficient energy storage systems that can store excess energy and release it when solar power generation is not possible.[11, 15, 16]

1.2. Importance of Carbon and Its Allotropes in Energy Applications

Carbon, as the fourth most abundant element on Earth by mass, exhibits exceptional versatility due to its ability to form a wide range of allotropes with distinct physical, chemical, and electronic properties.[17-19] This adaptability arises from carbon's capacity to form strong carbon-carbon (C-C) bonds in three different hybridization states: sp, sp^2, and sp^3. The resulting diversity in bonding configurations enables carbon to exist in various dimensional forms, ranging from 0-dimensional (0D) fullerenes, 1-dimensional (1D) carbon nanotubes (CNTs), and 2-dimensional (2D) graphene to 3-dimensional (3D) graphite and diamond structures.[20-24]

The ability of carbon to adopt different hybridization states and structural geometries results in a remarkable array of physical, chemical, and electronic properties. For example, carbon materials can exhibit characteristics ranging from insulating (diamond) to conducting

(graphite), from rigid and hard (diamond) to soft and lubricating (graphite), and from transparent (diamond) to opaque (graphite).[25, 26] This remarkable versatility makes carbon-based materials highly attractive for diverse energy-related applications, including supercapacitors, batteries, and solar cells.

Carbon exists in several allotropic forms, each possessing distinct properties that make them suitable for specific applications, particularly in energy storage and conversion. Diamond (3D) is composed of sp^3-hybridized carbon atoms arranged in a tetrahedral lattice, diamond is renowned for being the hardest natural material. It also exhibits exceptional thermal conductivity, making it valuable for heat management applications. However, due to the absence of free electrons, diamond is an electrical insulator and hence unsuitable for electronic energy applications.[27-32] Graphite (3D), in contrast consists of sp^2-hybridized carbon atoms arranged in stacked hexagonal layers. The weak van der Waals forces between the layers allow them to slide easily, giving graphite it's lubricating properties. Graphite also offers high in-plane electrical conductivity due to the free π-electrons, making it widely used in electrodes for batteries and supercapacitors. It's chemical stability and low cost further enhance its appeal in energy storage systems.[33, 34] Fullerenes (0D) are cage-like carbon structures, such as C_{60} (buckminsterfullerene), consist of hexagonal and pentagonal carbon rings arranged in spherical or ellipsoidal shapes. Fullerenes display unique electronic and optical properties, making them suitable for organic solar cells and molecular electronics. Their small size and electron affinity also make them promising for nanoscale energy storage applications.[35, 36] Carbon Nanotubes (1D) are cylindrical nanostructures formed by rolling graphene sheets into single-walled (SWCNTs) or multi-walled (MWCNTs) tubes. They exhibit exceptional tensile strength, electrical conductivity, and thermal stability, making them ideal for high-performance energy devices. CNTs are widely employed in supercapacitor electrodes and as additives in battery electrodes to enhance conductivity and mechanical stability.[37-43] Among the carbon

allotropes, graphene has attracted the most attention due to its extraordinary electronic, mechanical, and thermal properties. It consists of a single layer of sp^2-hybridized carbon atoms arranged in a honeycomb lattice. It's high electrical conductivity, large surface area, flexibility, and chemical stability make it a highly promising material for next-generation energy storage and conversion technologies, including supercapacitors and solar cells.[44-46]

1.3. Graphene as a Promising Material

Graphene stands out due to its exceptional properties and extensive application potential. It is a strictly two-dimensional (2D) material composed of a single atomic layer of sp^2-hybridized carbon atoms arranged in a honeycomb lattice**.** This unique structure gives graphene a zero-bandgap semi metallic nature, characterized by a slight overlap between its conduction band (CB) and valence band (VB) [47, 48]**.**

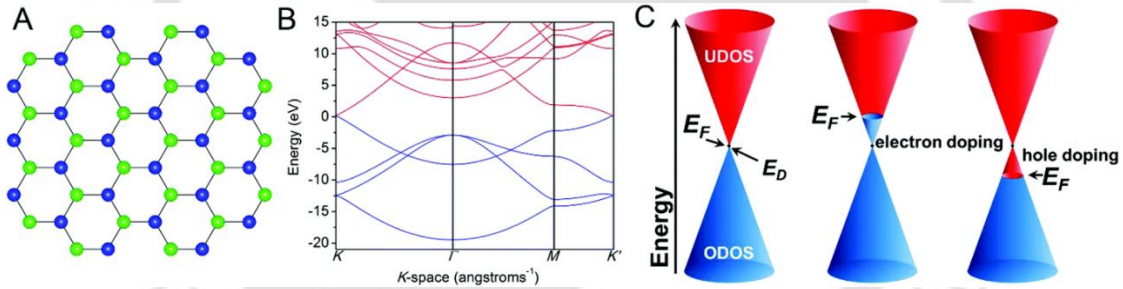

Fig. 1.1: (a) Hexagonal arrangement of carbon lattice (b) E-K diagram of single layered Graphene (c)Dirac cones depicting fermi level displacement after doping [49]

As a result, electrons in graphene behave like massless Dirac fermions, enabling ultra-fast charge transport with minimal scattering.[50-54] These remarkable electronic properties, combined with its high electrical conductivity, superior thermal conductivity, exceptional mechanical strength, optical transparency, and flexibility, make graphene highly attractive for advanced energy storage, optoelectronics, and next-generation technologies**.**[55-57]

Graphene's extraordinary characteristics stem from its 2D atomic structure and sp^2-hybridized bonding, which result in a remarkably high surface-to-volume ratio.[58-61] This makes it particularly suitable for applications requiring extensive surface interactions, such as supercapacitors and batteries. One of its most notable features is its exceptional electrical conductivity, with electron mobility reaching up to 200,000 $cm^2/V \cdot s$, far surpassing that of copper or silicon.[62-66] This outstanding conductivity makes graphene highly effective for rapid charge transport in supercapacitors and solar cells, enhancing their overall efficiency and performance.

In addition to its conductivity, graphene offers a large theoretical surface area (~2630 m^2/g), which provides abundant active sites for charge accumulation.[67-70] This makes it particularly valuable for energy storage applications, where higher surface area translates into greater capacitance and energy density. Graphene's mechanical strength is equally impressive, with a tensile strength of approximately 130 GPa, making it significantly stronger than steel while retaining exceptional flexibility.[71, 72] This combination of strength and pliability makes it an ideal candidate for flexible and wearable energy devices. [73-76] Its transparency, coupled with high conductivity and flexibility, offers a superior alternative to traditional indium tin oxide (ITO) electrodes, particularly in flexible and stretchable photovoltaic applications. These remarkable properties position graphene as a transformative material for future energy storage and conversion technologies, with the potential to significantly enhance both performance and efficiency.

Graphene's unique properties make it highly suitable for energy storage and solar energy conversion applications. Graphene offers distinct advantages over conventional materials used in energy applications. The large surface area and high conductivity of graphene make it an ideal electrode material for supercapacitors, which store energy through electrostatic charge

separation. Graphene electrodes offer higher capacitance and faster charge-discharge cycles compared to conventional carbon-based materials, significantly improving the device's power and energy density.[77-79] Additionally, its chemical stability ensures long-term performance without degradation, making graphene-based supercapacitors highly durable and efficient.[80-82]. Compared to carbon black electrodes, graphene exhibits lower internal resistance, enhancing the device's overall efficiency.[83, 84]

In solar cells, graphene-based heterojunctions with semiconductors, such as silicon, enhance charge separation and carrier mobility, improving the overall power conversion efficiency.[85] [86]. Additionally, graphene serves as an alternative to indium tin oxide (ITO), which is traditionally used as the transparent conductive electrode (TCE).[87, 88] Graphene's flexibility, transparency, and conductivity make it particularly advantageous for flexible and wearable photovoltaic devices.[89, 90] Additionally, while silicon-based solar cells dominate the market, they face efficiency limitations.[91] Incorporating graphene layers into solar cells enhances charge transport efficiency, reduces recombination losses, and boosts overall performance.[92] As research advances, the use of graphene-based materials in energy applications is expected to enhance efficiency, reduce costs, and improve the performance of renewable energy systems, paving the way for more sustainable and efficient energy solutions.[93, 94]

Graphene can be synthesized through various techniques, including mechanical exfoliation, chemical synthesis, epitaxial growth on silicon carbide (SiC), and chemical vapor deposition (CVD).[95, 96] Other approaches, such as unzipping carbon nanotubes and pyrolysis of sodium ethoxide, have also been explored for graphene synthesis.[97] However, these methods often require complex procedures and may not be feasible for large-scale production.[98] Among all the synthesis methods, CVD is regarded as one of the most promising techniques due to its ability to produce high-quality graphene on a large scale.[99, 100] CVD involves the deposition

of carbon atoms from a gaseous precursor onto a substrate, resulting in uniform and crystalline graphene layers. However, the bulk synthesis of graphene using CVD remains costly, prompting significant research interest in alternative, cost-effective methods for graphene-based material synthesis.[100, 101] One effective alternative involves the synthesis of graphene oxide (GO) from graphite, followed by its reduction to reduced graphene oxide (r-GO). This approach offers a practical route to graphene-like materials, as r-GO exhibits electronic and structural characteristics similar to pristine graphene.[102, 103] Furthermore, chemically synthesized r-GO can be produced at a lower cost and in larger quantities, broadening its applicability in commercial and research domains.

To harness graphene's properties for specific applications, it is crucial to control its electronic structure and tailor its characteristics. This can be achieved by modulating the carrier concentration through Fermi level (EF) tuning and doping. By adjusting the doping type (n-type or p-type), graphene's properties can be engineered to suit various applications, including photodetectors, photovoltaic devices, sensors, light-emitting diodes (LEDs), and supercapacitors [104]

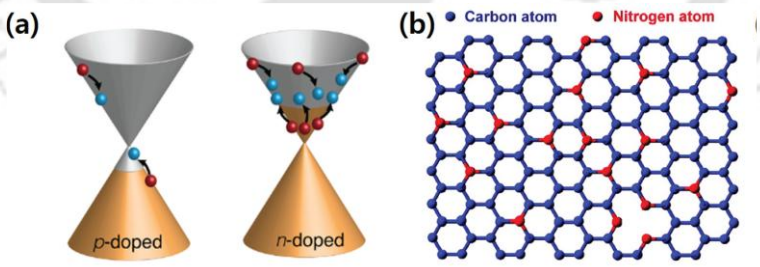

Fig. 1.2: (a) P or n-type doping in Graphene (b) doping by heteroatom substitution into Graphene [105]

Heteroatom substitution is a stable and effective method for achieving p-type and n-type doping in graphene.[106, 107] Through this approach, the electron and hole concentrations can be precisely controlled, enabling targeted bandgap tuning and enhanced electronic performance.

Introducing boron atoms into the graphene lattice increases hole concentration, imparting p-type characteristics. Boron-doped graphene exhibits improved electrical conductivity and facilitates a fast charge-discharge process, making it highly suitable for supercapacitors, battery technologies, and organic pollutant removal applications.[6]

N-type doping can be achieved by incorporating nitrogen atoms into the graphene lattice. Various nitrogen-containing precursors, including ammonia (NH_3), urea, melamine, and dimethylformamide (DMF), are commonly used for nitrogen doping due to their non-toxicity, low cost, and availability. Nitrogen-doped graphene offers enhanced electron mobility and stability, which is advantageous for electronic devices, catalysts, and energy storage systems.[108]

1.4. General Applications

Due to extra ordinary and wide range of properties, graphene-based materials are expected to have varieties of applications, as shown in fig. 1.3.

Graphene based materials could be potentially applied to various optoelectronic devices, ranging from solar cells to touch screens due to their unique optical, electronic and structural properties.[10] The high carrier mobility, excellent bendability, good transparency, and high electrical transport behavior makes it an extraordinary candidate for transparent electrodes and carrier transporting layers for PV solar cells.[11] Also, graphene coated glass hold good promise for thermochromic windows that benefit from the light interference effect of the changing layer thickness.[12] A large-area graphene film with high electrical quality grown on a copper substrate by chemical vapor deposition (CVD), is used to fabricate dual-gated field effect transistors, with Al_2O_3 as the gate dielectric. Quartz wafers, spin-coated by graphene oxide (GO) and annealed at a high-temperature (e.g. 1000°C), exhibited a high-transparency, and showed great potential as heating, defrosting and antifogging devices.[13]

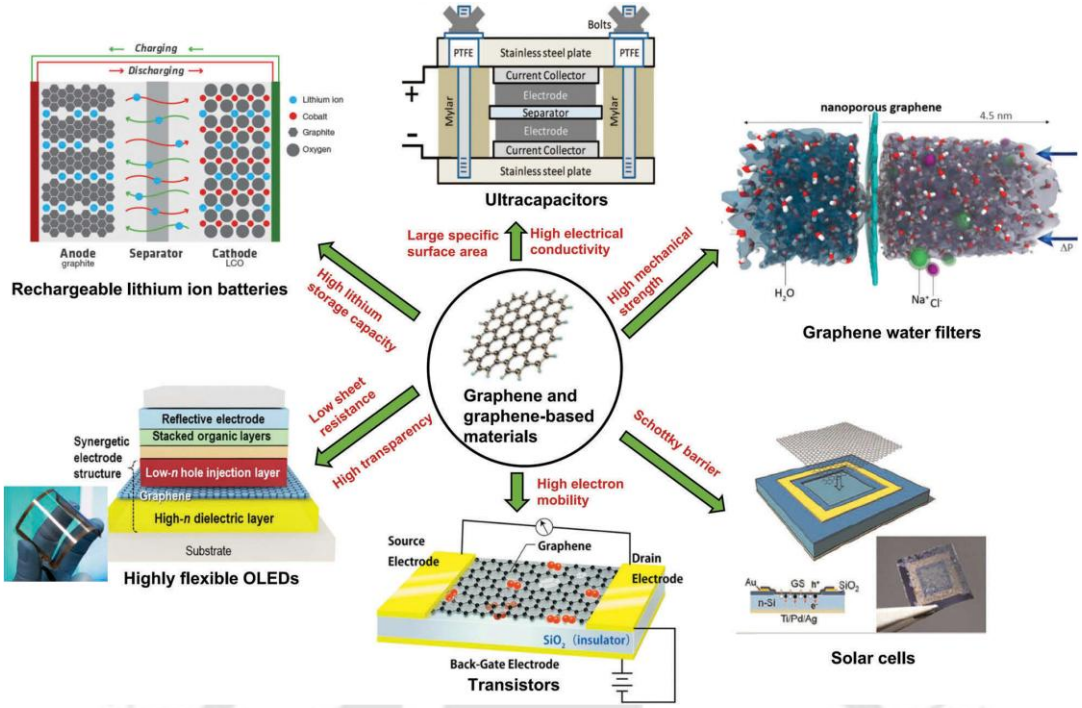

Fig. 1.3: Different applications of Graphene-based materials [3]

The construction of ultrathin PV devices is a promising way to decrease the material consumption and growth time if the high efficiency of the device can be maintained. The ultrathin devices present the advantages of being light-weight, flexible, and provide efficient transport and collection of photo-generated carriers.

Due to large surface area and high electrical conductivity, chemically modified graphene shows good performance in double layer capacitors.[14] By optimization of the structure (i.e. interlayer spacing, thickness and morphology of graphene nanosheets) and by incorporation of carbon nanotubes or C60 molecules, the lithium storage capacity of graphene nanosheets could be increased up to above 700mAh/g, making them suitable for use in rechargeable lithium-ion batteries.[15]

Beyond these, graphene based materials exhibit potential applications in a) catalysis, owing to their high specific surface area and accessibility to the surface; b) gas sensors, owing to the sensitivity and selectivity of graphene towards various gas molecules; c) waste energy

harvesting, because of their unique shape and characteristics such as high conductivity, light weight, high-stiffness and axial strength; d) protective coatings owing to the high intrinsic mechanical strength and anti-corrosion ability; e) antibacterial packing etc.[16,17]

1.5. Energy generation and storage applications

1.5.1. Graphene on silicon for PV applications

Two-dimensional graphene, which is one atom thick, is a versatile material with ultra-wideband applications such as optoelectronics and photonics [60]. Graphene's remarkable properties such as its tunable work function, flexibility, exceptional conductivity, optical transparency, and high stability are primarily responsible for its widespread application [109]. The first graphene/n-Si PV solar cell was demonstrated by Li et al. in 2011, with the Schottky Barrier Height (SBH) of ~0.78eV, an ideality factor of ~1.5 and an open-circuit voltage of 0.42–0.48V [110]. The depletion width of the device was estimated to be 0.5-0.7μm, which can be further enlarged to improve the IPCE (Incident Photon-to-Current Efficiency). The solar energy conversion efficiency was 1.65% for the solar cell (active area of 0.1cm^2), indicating that the interface quality, uniformity, and balancing between the transparency and conductivity should be carefully considered for further performance improvement. [110] Single layer graphene/n-Si Schottky junction solar cells that under AM1.5 illumination exhibit a power conversion efficiency (PCE) of 8.6%. This performance, achieved by doping the graphene with bis-(trifluoromethanesulfonyl)amide. A significant improvement in the power conversion efficiency (PCE) and the environmental stability of n-Graphene/p-Si solar cells is indicated through effective n-doping of graphene, using low work function oxide capping layers, AlO_x deposited through atomic layer deposition, is particularly effective for such doping and in addition serves as an antireflection coating and a cell encapsulating layer [111]. In recent years, high-efficiency solar cells fabricated by transferring graphene onto silicon were reported, but the device active area was very small and polymer residues were unavoidable in the transfer

process [112]. Its scalable process for industrial application is limited due to the unreliability of the graphene transfer. Moreover, the traditional chemical vapor deposition (CVD) process for the growth of superior graphene also requires an additional cost for a sacrificial Cu layer as metal catalyst [113]. The industrial mass production of graphene-based solar cells can be available with the direct growth plasma-enhanced chemical vapor deposition (PECVD) technique [112]. Another challenge for graphene-silicon junction solar cell is to have high transparency to pass more photons while keeping low sheet resistance. In order to overcome a trade-off relationship between the transmittance and conductivity another form of directly grown graphene has been considered in this study. A vertical graphene nano hills (VGNH) or graphene nanowalls can be grown by the PECVD process directly on silicon substrates. Since the work function of the graphene is dependent upon a number of layers, it should be controlled to achieve a large carrier density, open-circuit voltage, and built-in potential [112]. However, precisely controlling the number of layers of VGNH is another challenge. The graphene-based solar cell by using ambient pressure chemical vapor deposition (APCVD) was also attempted by Bi et al., but it required a very high temperature of 1200°C to achieve few layers of graphene. Such high temperatures are undesirable to make it cost-effective, and many substrates including glass cannot sustain this high temperature [114]. Liu et al. [115] demonstrated that a network of VGNH facilitates rapid collection of charge carriers with a reduction in joules heating. However, the maximum efficiency of these solar cells was 5.1% after doping, with a small active area of 0.09 cm^2. Similarly, Jiao et al. [116] used VGNH on textured substrates and achieved 6.6% efficiency after introducing silver nanowires. On the other hand, photodetectors were fabricated using VGNH, and high responsivity of 0.52 A/W ultralow current noise was demonstrated confirming the excellent junction quality.

1.5.2. Graphene-based materials for electrochemical applications

Graphene-based materials have found widespread application in energy conversion and storage because of its excellent and tuneable electrical, mechanical, and electrochemical properties. Large specific surface area, high power density, and rapid charge-discharge rates makes graphene-based materials suitable for EDLC's (Electrochemical double-layer capacitors) [102, 103, 106, 117, 118]. Graphene can be synthesized by a variety of methods, such as chemical vapor deposition, chemical exfoliation, and reduction of Graphene oxide by thermal or chemical routes. The electrical characteristics of graphene can be modified by different heteroatom doping such as boron, nitrogen, phosphorus, and sulphur. Doping graphene-based materials enhances their electrochemical characteristics by altering the charge distribution, which facilitates the transfer of charge between neighboring carbon atoms [119-124]. Because of their identical atomic radii and valency, nitrogen and boron atoms can readily substitute carbon atoms. There are two types of current heteroatom doping techniques for graphene: post-treatment techniques and in-situ synthesis techniques. Thermal annealing of graphene oxide with heteroatom precursors, plasma treatments, ultrasound-assisted doping, and arc-discharge are few examples [125-129]. Boron doping of 5.93% in graphene framework is reported via hydrogen induced thermal reduction method [130]. An increment from 53 F/g to 113 F/g is observed by boron-doping of Graphene Oxide by hydrothermal method [117]. Jing et al. [131] used in-situ alternating voltage electrochemical exfoliation to create nitrogen-doped graphene with a nitrogen content of 4.5 at%. When applied to lithium-ion batteries, the B-doped graphene's specific capacitance was 1.7 times more than the pristine graphene. By the hydrothermal technique, Das et al. [132] reported N-doped reduced GO (N-rGO) electrodes with an N-doping level of 7 at.%. Heteroatom-doped graphene has been produced in the last few years using plasma-assisted techniques [125-129]. An excellent specific capacitance value of 448F/g is obtained in boron-doped graphene oxide by chemical route doping and further

thermal reduction [106]. Wu et al. reported rf-plasma treated B-doped r-GO and N-doped r-GO with specific capacitance of 345 F/g and 365 F/g at respectively [133]. Co-doping of boron and nitrogen heteroatom by dielectric barrier discharge plasma treatment method have shown high specific capacitance value of 350 F/g [134]. Similarly, N and S co-doped GO by radio-frequency plasma treatment has shown specific capacitance value of 307.4 F/g at 1A/g having 83% retention after 10,000 cycles [125]. With the help of an H_2 plasma treatment, Seo et al. [135] synthesized vertically aligned graphene nanosheets on porous nickel foam, resulting in a three-electrode cell arrangement with a high specific capacitance of 230 F g^{-1} at a scan rate of 10 mV s^{-1}. A few more straightforward and cost-effective doping methods are hydrothermal and high-temperature thermal.

1.6. Motivation and objective of the present thesis:

- Synthesis of Graphene oxide from Graphite and then reducing it to Reduced Graphene Oxide (r-GO), can be an effective approach as r-GO have similar signature as that of Graphene. Further, substitution with heteroatom in Graphene oxide or reduced Graphene oxide is a stable approach for making p and n type doping in the Graphene lattice. From this method, the electron and hole concentration can be controlled. Here, basically band gap tuning is done to modulate electronic properties which gave excellent electrical conductivity. The boron doping into Graphene materials provide fast charge-discharge process in supercapacitors. Studies on structural, electrical, electrochemical and thermal properties of these Graphene-based materials is also very important for its further applications.
- The most popular and promising way to synthesize graphene is CVD because it can produce high-quality graphene on a large scale. Among different CVD systems, HWCVD (Hot Wire Chemical Vapor Deposition) is an effective approach for deposition of large-area uniform Graphene film on metal substrates such as Nickel and Copper which can be

further transferred to silicon for various opto-electronic applications. Deposition and structural, optical and electrical studies of multi-layer graphene on Nickel substrates and further optimization of its transfer mechanism to silicon substrate is important.

- Large-area, high-quality graphene directly on silicon substrate without metallic catalyst for its application in various semiconductor devices is an emerging field. For the deposition of Graphene film by CVD, we generally need metal catalyst, that's why we generally deposit it to Ni/Cu substrate and then transfer it. But the transfer process involves wear and tear which damages the Graphene film. So, direct growth of Graphene on Silicon substrates is important. Graphene films are deposited by PECVD (Plasma Enhanced Chemical Vapor Deposition) and HWCVD (Hot wire Chemical Vapor Deposition). The work function tunning of Graphene film by varying the number of layers of Graphene through variation in the deposition parameters and further fabrication Graphene-Silicon heterojunction solar cells is our approach.
- To better understand the mechanism of charge carrier transport and band diagram formed across the interface, simulation studies for the Graphene-Silicon heterojunction solar cells have also been conducted, AFORS-HET software is used for the simulation studies. It assists in directing us towards the best strategy for achieving better device performance and also gives us a clearer understanding of the various factors to be considered while fabricating the devices.

Thesis Outline

Chapter 1: Introduction

Our work is focused on usage of Graphene based materials for energy applications, so firstly literature survey is about synthesis of Graphene based materials such as Graphene Oxide, reduced Graphene Oxide, and its doping with boron source by chemical routes for supercapacitor application. Afterwards, we have deposited Graphene by HWCVD and PECVD on Nickel and Silicon substrate so we have discussed the literature about role of metal catalyst in the growth of Graphene and direct growth on silicon substrates for semiconductor application. Literature regarding fabrication of Graphene silicon heterojunction solar cells is also discussed.

Chapter 2: Experimental Details

This chapter presents brief description of chemical routes followed for the synthesis of Graphene-based materials; CVD systems used for graphene growth on different substrates such as hot wire/filament chemical vapor deposition (HWCVD), plasma-enhanced chemical vapor deposition (PECVD) and description of rf-sputtering used for ITO deposition for fabrication of solar cells. This chapter also contains a brief description of characterization techniques (XRD, FESEM, FETEM, AFM, KPFM, XPS etc.) used for the study of different properties of thin films and solar cells.

Chapter 3: Synthesis and Characterization of doped and undoped Graphene-based materials by chemical route

The synthesis of Graphene Oxide by Modified Hummer's method and its further conversion to reduced Graphene Oxide is discussed here. We have followed two routes for the reduction

process, one is chemical reduction and another one is thermal reduction. The comparative analysis of the r-GO samples produced by two techniques based on specific surface area, electrical conductivity and other structural properties are also discussed. Further, bulk synthesis of boron-doped reduced graphene oxide (B-rGO) as an electrode material for supercapacitors by using Boric acid (H_3BO_3) as boron source is also discussed. The structural properties of B-rGO, in comparison with Graphene Oxide (GO), Graphite and reduced Graphene Oxide(r-GO) has been studied by XRD, Raman and FETEM analysis. The boron doping of ~9% has been confirmed by EDAX analysis. An increase in inter-layer spacing from 0.23nm to 0.28nm has been observed in BrGO due to intercalation of boron atom in the lattice. FTIR studies also confirmed the doping due to presence of B-C and B-O bond. We have reported an increased specific capacitance of 326.56 F/g for B-rGO compared to GO (137.88 F/g) and r-GO (108.85 F/g). Nitrogen doped r-GO samples (melamine as nitrogen source) have also been prepared for which doping has been confirmed by FTIR and EDX. The corresponding structural properties have also been studied by XRD and Raman and electrical conductivity is also calculated. For all the chemically prepared samples i.e. GO, r-GO, B-rGO and r-BGO, thermal kinetics study is done to know the activation energies and entropy change at various stages of degradation with temperature.

Chapter 4: Growth of multi-layer Graphene by HWCVD on Ni substrate

This chapter describes the growth of single and multi-layer Graphene by HWCVD (Hot wire Chemical Vapor Deposition) on Nickel substrate. We have briefly discussed the growth mechanism and its transfer process from Nickel substrate to Silicon. The variation on the number of layers of Graphene and uniformity of the films with respect to deposition parameters such as substrate temperature, process pressure, CH_4/H_2 gas flow rates, deposition time and filament to substrate distance is studied by AFM and Raman analysis. Here the number of layers is varied from 2-10. It is observed that by increasing the hydrogen concentration the number of

layers of Graphene decreased this could be due to better dissociation of CH_4 with hydrogen. The optimization is also done by increasing the deposition temperature and further annealing the film. Afterwards, Grapheme films were transferred on silicon substrates using chemical etching process.

Chapter 5: Work function tunning of directly grown multi-layer Graphene on Silicon Substrate by PECVD and HWCVD and Solar cell fabrication

This chapter reports the production of large-area, high-quality graphene directly on silicon substrate without a metallic catalyst for application in semiconductor devices. Graphene films are deposited by PECVD (Plasma Enhanced Chemical Vapor Deposition) and HWCVD (Hot Wire Chemical Vapor Deposition) with tunable work function based on the number of graphene layers. This is achieved by varying deposition parameters such as process pressure, temperature, and time. Graphene quality is confirmed by Raman and XPS studies. Film uniformity is verified by FESEM, and surface roughness by AFM. EDAX is used to study the C/Si ratio. Work function is measured by surface potential mapping via KPFM. A variation from 4.15 eV to 4.54 eV is observed by altering RF power and gas flow rates of methane and hydrogen. A solar cell is fabricated with structure Ag/ITO/Gr/n-Si/Ag, achieving 1% efficiency, 25.52 mA/cm² current density, 0.13 V open circuit voltage (V_{oc}), and 0.29 FF

Chapter 6: Simulation studies on graphene/a-Si:H(i)/c-Si(H) solar cells: role of doping concentration, thickness of intrinsic layer and number of layers of Graphene

This chapter presents the simulation studies of Graphene/ silicon heterojunction solar cells using a user-friendly software AFORS-HET (Automat FOR Simulation of HETero structures) v-2.5 under AM1.5 illumination and power density of 100mW/cm^2. Firstly, we have simulated n-graphene/Silicon hetero-structure Ag/ITO/n-Graphene/c-Si(p)/Ag. Ag/ITO/n-Graphene/a-Si:H/c-Si(p)/Ag Here, the thickness of a-Si:H i-layer from 0 to 20nm,

the n-type doping concentration of Graphene from $1 \times 10^{10}cm^{-3}$ to $1 \times 10^{20}cm^{-3}$ to get the optimized results. Corresponding to that, we studied the band diagram and hence barrier height, quantum efficiency etc. The best power conversion efficiency (PCE) obtained is 18.59% where the open circuit voltage (V_{oc}) is 611.8 mV, short circuit current (J_{sc}) is 37.04 mA/cm^2 and fill factor (FF) is 82.03% corresponding to i-layer thickness 5nm, single layer graphene and n-type doping concentration of $1 \times 10^{20}cm^{-3}$.

Chapter 7: Conclusion and future scope

This chapter summarizes the contents of each chapter and gives the conclusion based on the work reported in this thesis. The thesis work is concluded with the scope for future work from the present investigation.

1.7. References

1. Wang, J. and W. Azam, *Natural resource scarcity, fossil fuel energy consumption, and total greenhouse gas emissions in top emitting countries.* Geoscience Frontiers, 2024. **15**(2): p. 101757.
2. Hassan, Q., S. Algburi, A.Z. Sameen, H.M. Salman, and M. Jaszczur, *Green hydrogen: A pathway to a sustainable energy future.* International Journal of Hydrogen Energy, 2024. **50**: p. 310-333.
3. Available from: https://www.energy.gov/articles/top-6-things-you-didnt-know-about-solar-energy.
4. Hassan, Q., P. Viktor, T. J. Al-Musawi, B. Mahmood Ali, S. Algburi, H.M. Alzoubi, A. Khudhair Al-Jiboory, A. Zuhair Sameen, H.M. Salman, and M. Jaszczur, *The renewable energy role in the global energy Transformations.* Renewable Energy Focus, 2024. **48**: p. 100545.
5. Nunes, L.J.R., *The Rising Threat of Atmospheric CO2: A Review on the Causes, Impacts, and Mitigation Strategies.* Environments, 2023. **10**(4): p. 66.
6. Ofremu, G.O., B.Y. Raimi, S.O. Yusuf, B.A. Dziwornu, S.G. Nnabuife, A.M. Eze, and C.A. Nnajiofor, *Exploring the Relationship between Climate Change, Air Pollutants and Human Health: Impacts, Adaptation, and Mitigation Strategies.* Green Energy and Resources, 2024: p. 100074.
7. Wang, Q., X. Wang, and R. Li, *Geopolitical risks and energy transition: the impact of environmental regulation and green innovation.* Humanities and Social Sciences Communications, 2024. **11**(1): p. 1272.
8. Tabash, M.I., U. Farooq, M.A.S. Al-Faryan, and W.K. Wong, *Effect of geopolitical risk on energy consumption policy: New empirical evidence from BRICS.* Heliyon, 2024. **10**(19): p. 38049.
9. Vakulchuk, R., I. Overland, and D. Scholten, *Renewable energy and geopolitics: A review.* Renewable and Sustainable Energy Reviews, 2020. **122**: p. 109547.
10. Jayabal, R., *Towards a carbon-free society: Innovations in green energy for a sustainable future.* Results in Engineering, 2024. **24**: p. 103121.

11. Hassan, Q., S. Algburi, A.Z. Sameen, H.M. Salman, and M. Jaszczur, *A review of hybrid renewable energy systems: Solar and wind-powered solutions: Challenges, opportunities, and policy implications.* Results in Engineering, 2023. **20**: p. 101621.
12. Ukoba, K., K.O. Yoro, O. Eterigho-Ikelegbe, C. Ibegbulam, and T.C. Jen, *Adaptation of solar energy in the Global South: Prospects, challenges and opportunities.* Heliyon, 2024. **10**(7): p. 28009.
13. C.J, R., K.H. Lim, J.C. Kurnia, S. Roy, B.J. Bora, and B.J. Medhi, *Towards sustainable power generation: Recent advancements in floating photovoltaic technologies.* Renewable and Sustainable Energy Reviews, 2024. **194**: p. 114322.
14. Hasan, M.M., S. Hossain, M. Mofijur, Z. Kabir, I.A. Badruddin, T.M. Yunus Khan, and E. Jassim, *Harnessing Solar Power: A Review of Photovoltaic Innovations, Solar Thermal Systems, and the Dawn of Energy Storage Solutions.* Energies, 2023. **16**(18): p. 6456.
15. Jafarizadeh, H., E. Yamini, S.M. Zolfaghari, F. Esmaeilion, M.E.H. Assad, and M. Soltani, *Navigating challenges in large-scale renewable energy storage: Barriers, solutions, and innovations.* Energy Reports, 2024. **12**: p. 2179-2192.
16. Sayed, E., A. Olabi, A. Alami, A. Radwan, A. Mdallal, A. Rezk, and M. Abdelkareem, *Renewable Energy and Energy Storage Systems.* Energies, 2023. **16**(3): p. 1415.
17. Johnson, A.P., H.V. Gangadharappa, and K. Pramod, *Graphene nanoribbons: A promising nanomaterial for biomedical applications.* J Control Release, 2020. **325**: p. 141-162.
18. Nasir, S., M.Z. Hussein, Z. Zainal, and N.A. Yusof, *Carbon-Based Nanomaterials/Allotropes: A Glimpse of Their Synthesis, Properties and Some Applications.* Materials (Basel), 2018. **11**(2): p. 295.
19. Farmani, Z., A. Vetere, N. Pfander, C.W. Lehmann, and W. Schrader, *Naturally Occurring Allotropes of Carbon.* Anal Chem, 2024. **96**(7): p. 2968-2974.
20. Saleh, H.M. and A.I. Hassan, *Synthesis and Characterization of Nanomaterials for Application in Cost-Effective Electrochemical Devices.* Sustainability, 2023. **15**(14): p. 10891.
21. Vejpravova, J., *Mixed sp(2)-sp(3) Nanocarbon Materials: A Status Quo Review.* Nanomaterials (Basel), 2021. **11**(10): p. 2469.
22. Georgakilas, V., J.A. Perman, J. Tucek, and R. Zboril, *Broad family of carbon nanoallotropes: classification, chemistry, and applications of fullerenes, carbon dots, nanotubes, graphene, nanodiamonds, and combined superstructures.* Chem Rev, 2015. **115**(11): p. 4744-4822.
23. Zhang, W., C. Chai, Q. Fan, Y. Song, and Y. Yang, *A novel two-dimensional sp-sp2-sp3 hybridized carbon nanostructure with a negative in-plane Poisson ratio and high electron mobility.* Computational Materials Science, 2020. **185**: p. 109904.
24. Georgakilas, V., M. Otyepka, A.B. Bourlinos, V. Chandra, N. Kim, K.C. Kemp, P. Hobza, R. Zboril, and K.S. Kim, *Functionalization of graphene: covalent and non-covalent approaches, derivatives and applications.* Chem Rev, 2012. **112**(11): p. 6156-6214.
25. Okwundu, O.S., E.U. Aniekwe, and C.E. Nwanno, *Unlimited potentials of carbon: different structures and uses (a Review).* Metallurgical and Materials Engineering, 2018. **24**(3): p. 145-171.
26. Das, S., R. Seelaboyina, V. Verma, I. Lahiri, J.Y. Hwang, R. Banerjee, and W. Choi, *Synthesis and characterization of self-organized multilayered graphene–carbon nanotube hybrid films.* Journal of Materials Chemistry, 2011. **21**(20): p. 7289.
27. Shang, Y., M. Yao, Z. Liu, R. Fu, L. Yan, L. Yang, Z. Zhang, J. Dong, C. Zhai, X. Hou, L. Fei, G. Zhang, J. Ji, J. Zhu, H. Lin, B. Sundqvist, and B. Liu, *Enhancement of short/medium-range order and thermal conductivity in ultrahard sp(3) amorphous carbon by C(70) precursor.* Nat Commun, 2023. **14**(1): p. 7860.
28. Ku, Y., W. Huang, X. Li, L. Wan, K. Zhang, L. Yan, Y. Guo, S. Cheng, and C. Shan, *Rational design of diamond through microstructure engineering: From synthesis to applications.* Carbon Energy, 2024. **6**(7): p. 1-29.
29. Brazhkin, V.V. and V.L. Solozhenko, *Myths about new ultrahard phases: Why materials that are significantly superior to diamond in elastic moduli and hardness are impossible.* Journal of Applied Physics, 2019. **125**(13): p. 130901.
30. Slepickova Kasalkova, N., P. Slepicka, and V. Svorcik, *Carbon Nanostructures, Nanolayers, and Their Composites.* Nanomaterials (Basel), 2021. **11**(9): p. 2368.

31. Li, Y., L. Yang, X. Jiang, Y. Lu, C. Han, Y. Tang, and N. Yang, *Diamond Nanostructures at Different Dimensions: Synthesis and Applications.* Advanced Functional Materials, 2024. **34**(30): p. 14558.
32. Field, J.E., *The mechanical and strength properties of diamond.* Rep Prog Phys, 2012. **75**(12): p. 126505.
33. Jara, A.D., A. Betemariam, G. Woldetinsae, and J.Y. Kim, *Purification, application and current market trend of natural graphite: A review.* International Journal of Mining Science and Technology, 2019. **29**(5): p. 671-689.
34. Tomanik, E., W. Christinelli, R.M. Souza, V.L. Oliveira, F. Ferreira, and B. Zhmud, *Review of Graphene-Based Materials for Tribological Engineering Applications.* Eng, 2023. **4**(4): p. 2764-2811.
35. Schwerdtfeger, P., L.N. Wirz, and J. Avery, *The topology of fullerenes.* Wiley Interdiscip Rev Comput Mol Sci, 2015. **5**(1): p. 96-145.
36. Chiang, L.Y., R.B. Upasani, and J.W. Swirczewski, *Versatile nitronium chemistry for C60 fullerene functionalization.* Journal of the American Chemical Society, 2002. **114**(26): p. 10154-10157.
37. Maheswaran, R. and B.P. Shanmugavel, *A Critical Review of the Role of Carbon Nanotubes in the Progress of Next-Generation Electronic Applications.* J Electron Mater, 2022. **51**(6): p. 2786-2800.
38. Nurazzi, N.M., F.A. Sabaruddin, M.M. Harussani, S.H. Kamarudin, M. Rayung, M.R.M. Asyraf, H.A. Aisyah, M.N.F. Norrrahim, R.A. Ilyas, N. Abdullah, E.S. Zainudin, S.M. Sapuan, and A. Khalina, *Mechanical Performance and Applications of CNTs Reinforced Polymer Composites-A Review.* Nanomaterials (Basel), 2021. **11**(9): p. 2186.
39. Aqel, A., K.M.M.A. El-Nour, R.A.A. Ammar, and A. Al-Warthan, *Carbon nanotubes, science and technology part (I) structure, synthesis and characterisation.* Arabian Journal of Chemistry, 2012. **5**(1): p. 1-23.
40. Oladunni, J., J.H. Zain, A. Hai, F. Banat, G. Bharath, and E. Alhseinat, *A comprehensive review on recently developed carbon based nanocomposites for capacitive deionization: From theory to practice.* Separation and Purification Technology, 2018. **207**: p. 291-320.
41. Rahman, G., Z. Najaf, A. Mehmood, S. Bilal, A. Shah, S. Mian, and G. Ali, *An Overview of the Recent Progress in the Synthesis and Applications of Carbon Nanotubes.* C, 2019. **5**(1): p. 3.
42. Patel, D.K., H.B. Kim, S.D. Dutta, K. Ganguly, and K.T. Lim, *Carbon Nanotubes-Based Nanomaterials and Their Agricultural and Biotechnological Applications.* Materials (Basel), 2020. **13**(7): p. 1679.
43. Kolahdouz, M., B. Xu, A.F. Nasiri, M. Fathollahzadeh, M. Manian, H. Aghababa, Y. Wu, and H.H. Radamson, *Carbon-Related Materials: Graphene and Carbon Nanotubes in Semiconductor Applications and Design.* Micromachines (Basel), 2022. **13**(8): p. 1257.
44. Singh, R., H. Rawat, A. Kumar, Y. Gandhi, V. Kumar, S.K. Mishra, and C.V. Narasimhaji, *Graphene and its hybrid nanocomposite: A Metamorphoses elevation in the field of tissue engineering.* Heliyon, 2024. **10**(13): p. 33542.
45. Allen, M.J., V.C. Tung, and R.B. Kaner, *Honeycomb carbon: a review of graphene.* Chem Rev, 2010. **110**(1): p. 132-45.
46. Zhong, Y., Z. Zhen, and H. Zhu, *Graphene: Fundamental research and potential applications.* FlatChem, 2017. **4**: p. 20-32.
47. Novoselov, K.S., *Nobel Lecture: Graphene: Materials in the Flatland.* Reviews of Modern Physics, 2011. **83**(3): p. 837-849.
48. Miro, P., M. Audiffred, and T. Heine, *An atlas of two-dimensional materials.* Chem Soc Rev, 2014. **43**(18): p. 6537-54.
49. Schultz, B.J., R.V. Dennis, V. Lee, and S. Banerjee, *An electronic structure perspective of graphene interfaces.* Nanoscale, 2014. **6**(7): p. 3444-3466.
50. Mics, Z., K.J. Tielrooij, K. Parvez, S.A. Jensen, I. Ivanov, X. Feng, K. Mullen, M. Bonn, and D. Turchinovich, *Thermodynamic picture of ultrafast charge transport in graphene.* Nat Commun, 2015. **6**: p. 7655.
51. Pachoud, A., M. Jaiswal, Y. Wang, B.H. Hong, J.H. Ahn, K.P. Loh, and B. Ozyilmaz, *Multiple virtual tunneling of Dirac fermions in granular graphene.* Sci Rep, 2013. **3**: p. 3404.

52. Avouris, P., *Electron transport and excitations in graphene.* Procedia Chemistry, 2011. **3**(1): p. 352-362.
53. Ullal, C.K., J. Shi, and R. Sundararaman, *Electron mobility in graphene without invoking the Dirac equation.* American Journal of Physics, 2019. **87**(4): p. 291-295.
54. Sang, M., J. Shin, K. Kim, and K.J. Yu, *Electronic and Thermal Properties of Graphene and Recent Advances in Graphene Based Electronics Applications.* Nanomaterials (Basel), 2019. **9**(3): p. 374.
55. Mondal, H., M. Hossain, M. Rahaman, S. Amin, M. Hossain, M. Hasan Mahasin, and P. Mondal, *Optoelectronics Based Dynamic Advancement of Graphene: Characteristics and Applications.* Crystals, 2018. **8**(4): p. 171.
56. Althumayri, M., R. Das, R. Banavath, L. Beker, A.M. Achim, and H. Ceylan Koydemir, *Recent Advances in Transparent Electrodes and Their Multimodal Sensing Applications.* Adv Sci (Weinh), 2024. **11**(38): p. 2405099.
57. Kang, J.H., S. Choi, Y.J. Park, J.S. Park, N.S. Cho, S. Cho, B. Walker, D.S. Choi, J.-W. Shin, and J.H. Seo, *Cu/graphene hybrid transparent conducting electrodes for organic photovoltaic devices.* Carbon, 2021. **171**: p. 341-349.
58. Yusaf, T., A.S.F. Mahamude, K. Farhana, W.S.W. Harun, K. Kadirgama, D. Ramasamy, M.K. Kamarulzaman, S. Subramonian, S. Hall, and H.A. Dhahad, *A Comprehensive Review on Graphene Nanoparticles: Preparation, Properties, and Applications.* Sustainability, 2022. **14**(19): p. 12336.
59. George, J. and D. Bhattacharyya, *Graphene: an introduction*, in *Recent Advances in Graphene and Graphene-Based Technologies*. 2023. p. 1-24.
60. Lei, Y., T. Zhang, Y.C. Lin, T. Granzier-Nakajima, G. Bepete, D.A. Kowalczyk, Z. Lin, D. Zhou, T.F. Schranghamer, A. Dodda, A. Sebastian, Y. Chen, Y. Liu, G. Pourtois, T.J. Kempa, B. Schuler, M.T. Edmonds, S.Y. Quek, U. Wurstbauer, S.M. Wu, N.R. Glavin, S. Das, S.P. Dash, J.M. Redwing, J.A. Robinson, and M. Terrones, *Graphene and Beyond: Recent Advances in Two-Dimensional Materials Synthesis, Properties, and Devices.* ACS Nanosci Au, 2022. **2**(6): p. 450-485.
61. Yang, G., L. Li, W.B. Lee, and M.C. Ng, *Structure of graphene and its disorders: a review.* Sci Technol Adv Mater, 2018. **19**(1): p. 613-648.
62. Kim, T., S. Fan, S. Lee, M.K. Joo, and Y.H. Lee, *High-mobility junction field-effect transistor via graphene/MoS(2) heterointerface.* Sci Rep, 2020. **10**(1): p. 13101.
63. Mir, S.H., V.K. Yadav, and J.K. Singh, *Recent Advances in the Carrier Mobility of Two-Dimensional Materials: A Theoretical Perspective.* ACS Omega, 2020. **5**(24): p. 14203-14211.
64. Thodkar, K. and F. Gramm, *Enhanced Mobility in Suspended Chemical Vapor-Deposited Graphene Field-Effect Devices in Ambient Conditions.* ACS Appl Mater Interfaces, 2023. **15**(31): p. 37756-37763.
65. Bolotin, K.I., K.J. Sikes, Z. Jiang, M. Klima, G. Fudenberg, J. Hone, P. Kim, and H.L. Stormer, *Ultrahigh electron mobility in suspended graphene.* Solid State Communications, 2008. **146**(9-10): p. 351-355.
66. Dutta, T., N. Yadav, Y. Wu, G.J. Cheng, X. Liang, S. Ramakrishna, A. Sbai, R. Gupta, A. Mondal, Z. Hongyu, and A. Yadav, *Electronic properties of 2D materials and their junctions.* Nano Materials Science, 2024. **6**(1): p. 1-23.
67. Liu, C., Z. Yu, D. Neff, A. Zhamu, and B.Z. Jang, *Graphene-based supercapacitor with an ultrahigh energy density.* Nano Lett, 2010. **10**(12): p. 4863-4868.
68. Alekseeva, O.K., I.V. Pushkareva, A.S. Pushkarev, and V.N. Fateev, *Graphene and Graphene-Like Materials for Hydrogen Energy.* Nanotechnol Russ, 2020. **15**(3): p. 273-300.
69. Du, Y., M. Wang, X. Ye, B. Liu, L. Han, S.H.M. Jafri, W. Liu, X. Zheng, Y. Ning, and H. Li, *Advances in the Field of Graphene-Based Composites for Energy–Storage Applications.* Crystals, 2023. **13**(6): p. 912.
70. Zhou, Q., M. Shi, M. Wu, N. Zhao, P. Shi, Y. Zhu, A. Wang, C. Ye, C.-T. Lin, and L. Fu, *Optimizing Graphene Dopants for Direct Electrocatalytic Quantification of Small Molecules and Ions.* Catalysts, 2023. **14**(1): p. 8.
71. Zhai, H., J. Liu, Z. Liu, and Y. Li, *Functional Graphene Fiber Materials for Advanced Wearable Applications.* Advanced Fiber Materials, 2025. **25**: p. 00512.

72. Shen, C. and S.O. Oyadiji, *The processing and analysis of graphene and the strength enhancement effect of graphene-based filler materials: A review.* Materials Today Physics, 2020. **15**: p. 100257.
73. Neves, A.I., T.H. Bointon, L.V. Melo, S. Russo, I. de Schrijver, M.F. Craciun, and H. Alves, *Transparent conductive graphene textile fibers.* Sci Rep, 2015. **5**: p. 9866.
74. Woo, Y.S., *Transparent Conductive Electrodes Based on Graphene-Related Materials.* Micromachines (Basel), 2018. **10**(1): p. 13.
75. Pang, S., Y. Hernandez, X. Feng, and K. Mullen, *Graphene as transparent electrode material for organic electronics.* Adv Mater, 2011. **23**(25): p. 2779-2795.
76. Peksu, E., C. Yener, C.G. Unlu, and H. Karaagac, *Exploring graphene's potential as a transparent conductive layer in Cu2ZnSnS4 superstrate solar cells.* Journal of Alloys and Compounds, 2024. **976**: p. 172979.
77. Ahmad, F., M. Zahid, H. Jamil, M.A. Khan, S. Atiq, M. Bibi, K. Shahbaz, M. Adnan, M. Danish, F. Rasheed, H. Tahseen, M.J. Shabbir, M. Bilal, and A. Samreen, *Advances in graphene-based electrode materials for high-performance supercapacitors: A review.* Journal of Energy Storage, 2023. **72**.
78. Sahoo, P.K., N. Kumar, A. Jena, S. Mishra, C.P. Lee, S.Y. Lee, and S.J. Park, *Recent progress in graphene and its derived hybrid materials for high-performance supercapacitor electrode applications.* RSC Adv, 2024. **14**(2): p. 1284-1303.
79. Chen, S., W. Wang, X. Zhang, and X. Wang, *High-Performance Supercapacitors Based on Graphene/Activated Carbon Hybrid Electrodes Prepared via Dry Processing.* Batteries, 2024. **10**(6).
80. Pathak, M., S.M. Jeong, and C.S. Rout, *Graphene hybrids for supercapacitor applications.* Chem Commun (Camb), 2025. **61**(49): p. 8803-8829.
81. Yu, J., Z. Zhao, Z. Zhang, J. Huang, and P. Tan, *Resolving the true origin of mossy morphology in aqueous Zn batteries.* EES Batteries, 2026.
82. Ahmad, N., A. Rinaldi, M. Sidoli, G. Magnani, A. Morenghi, S. Scaravonati, V. Vezzoni, L. Pasetti, L. Fornasini, F. Ridi, C. Milanese, M. Riccò, and D. Pontiroli, *High performance quasi-solid-state supercapacitor based on activated carbon derived from asparagus waste.* Journal of Energy Storage, 2024. **99**.
83. Choi, C.J., T.H. Kim, H.W. Kim, D.M. Jeon, and J. Han, *Improving Electrochemical Performance of Ultrahigh-Loading Cathodes via the Addition of Multi-Walled Carbon Nanotubes.* Nanomaterials (Basel), 2025. **15**(3).
84. Rapisarda, M., A. Damasco, G. Abbate, and M. Meo, *Carbon Black and Reduced Graphene Oxide Nanocomposite for Binder-Free Supercapacitors with Reduced Graphene Oxide Paper as the Current Collector.* ACS Omega, 2020. **5**(50): p. 32426-32435.
85. Zhong, Y., Y. Xiao, Q. Chen, and H. Zhu, *Heterojunction solar cells based on graphene woven fabrics and silicon.* Journal of Materiomics, 2018. **4**(2): p. 135-138.
86. Singh, E. and H.S. Nalwa, *Stability of graphene-based heterojunction solar cells.* RSC Advances, 2015. **5**(90): p. 73575-73600.
87. Woo, Y.S., *Transparent Conductive Electrodes Based on Graphene-Related Materials.* Micromachines (Basel), 2018. **10**(1).
88. Redoy, R.A.F., S.S. Rashid, O.M.S. Alghamdi, S. Aljohani, S. Sameer, T. Islam, R. Aktar, N.A. Alghamdi, O.A. Alhartomy, and S. Wageh, *Assessing the potential and challenges of Graphene in optoelectronic applications: A comprehensive review.* Materials Science in Semiconductor Processing, 2026. **202**.
89. Bagade, S.S., S. Patel, M.M. Malik, and P.K. Patel, *Recent Advancements in Applications of Graphene to Attain Next-Level Solar Cells.* C, 2023. **9**(3).
90. Kim, H. and J.-H. Ahn, *Graphene for flexible and wearable device applications.* Carbon, 2017. **120**: p. 244-257.
91. Kanti, P.K., D.J. K, J. Swapnalin, and V. Vicki Wanatasanappan, *Advancements and prospects of MXenes in emerging solar cell technologies.* Solar Energy Materials and Solar Cells, 2025. **285**.

92. Safie, N.E., M.A. Azam, M.F.A. Aziz, and M. Ismail, *Recent progress of graphene-based materials for efficient charge transfer and device performance stability in perovskite solar cells.* International Journal of Energy Research, 2020. **45**(2): p. 1347-1374.
93. Shaker, L.M., A.A. Abdulamier, and A.A. Al-Amiery, *Graphene-based materials for next-generation energy storage: Progress, challenges, and future outlook.* Journal of Alloys and Compounds, 2025. **1036**.
94. Saeed, M.A., A. Abdelkader, Y. Alshammari, C. Valles, and A. Alkandary, *Graphene Applications in Composites, Energy, and Water Treatment.* Macromolecular Materials and Engineering, 2025. **310**(4).
95. Singh, S., K. Rathi, and K. Pal, *Synthesis, characterization of graphene oxide wrapped silicon carbide for excellent mechanical and damping performance for aerospace application.* Journal of Alloys and Compounds, 2018. **740**: p. 436-445.
96. Santhiran, A., P. Iyngaran, P. Abiman, and N. Kuganathan, *Graphene Synthesis and Its Recent Advances in Applications—A Review.* C, 2021. **7**(4).
97. Lee, H.C., W.-W. Liu, S.-P. Chai, A.R. Mohamed, A. Aziz, C.-S. Khe, N.M.S. Hidayah, and U. Hashim, *Review of the synthesis, transfer, characterization and growth mechanisms of single and multilayer graphene.* RSC Advances, 2017. **7**(26): p. 15644-15693.
98. Solis-Fernandez, P., M. Bissett, and H. Ago, *Synthesis, structure and applications of graphene-based 2D heterostructures.* Chem Soc Rev, 2017. **46**(15): p. 4572-4613.
99. Liu, Z., L. Lin, H. Ren, and X. Sun, *CVD Synthesis of Graphene*, in *Thermal Transport in Carbon-Based Nanomaterials*. 2017. p. 19-56.
100. Saeed, M., Y. Alshammari, S.A. Majeed, and E. Al-Nasrallah, *Chemical Vapour Deposition of Graphene-Synthesis, Characterisation, and Applications: A Review.* Molecules, 2020. **25**(17).
101. Kashyap, P.K., I. Sharma, and B.K. Gupta, *Continuous Growth of Highly Reproducible Single-Layer Graphene Deposition on Cu Foil by Indigenously Developed LPCVD Setup.* ACS Omega, 2019. **4**(2): p. 2893-2901.
102. Guo, S. and S. Dong, *Graphene nanosheet: synthesis, molecular engineering, thin film, hybrids, and energy and analytical applications.* Chem Soc Rev, 2011. **40**(5): p. 2644-2672.
103. Rasul, S., A. Alazmi, K. Jaouen, M.N. Hedhili, and P.M.F.J. Costa, *Rational design of reduced graphene oxide for superior performance of supercapacitor electrodes.* Carbon, 2017. **111**: p. 774-781.
104. Tao, H., C. Yan, A.W. Robertson, Y. Gao, J. Ding, Y. Zhang, T. Ma, and Z. Sun, *N-Doping of graphene oxide at low temperature for the oxygen reduction reaction.* Chem Commun (Camb), 2017. **53**(5): p. 873-876.
105. Lee, H., K. Paeng, and I.S. Kim, *A review of doping modulation in graphene.* Synthetic Metals, 2018. **244**: p. 36-47.
106. Yeom, D.Y., W. Jeon, N.D. Tu, S.Y. Yeo, S.S. Lee, B.J. Sung, H. Chang, J.A. Lim, and H. Kim, *High-concentration boron doping of graphene nanoplatelets by simple thermal annealing and their supercapacitive properties.* Sci Rep, 2015. **5**: p. 9817.
107. Cheng, W., X. Liu, N. Li, J. Han, S. Li, and S. Yu, *Boron-doped graphene as a metal-free catalyst for gas-phase oxidation of benzyl alcohol to benzaldehyde.* RSC Adv, 2018. **8**(20): p. 11222-11229.
108. Selvakumar, D., G. Murugadoss, A. Alsalme, A.M. Alkathiri, and R. Jayavel, *Heteroatom doped reduced graphene oxide paper for large area perovskite solar cells.* Solar Energy, 2018. **163**: p. 564-569.
109. Tiwari, S.K., S. Sahoo, N. Wang, and A. Huczko, *Graphene research and their outputs: Status and prospect.* Journal of Science: Advanced Materials and Devices, 2020. **5**(1): p. 10-29.
110. Li, X., H. Zhu, K. Wang, A. Cao, J. Wei, C. Li, Y. Jia, Z. Li, X. Li, and D. Wu, *Graphene-on-silicon Schottky junction solar cells.* Adv Mater, 2010. **22**(25): p. 2743-2748.
111. Yavuz, S., E.M. Loran, N. Sarkar, D.P. Fenning, and P.R. Bandaru, *Enhanced Environmental Stability Coupled with a 12.5% Power Conversion Efficiency in an Aluminum Oxide-Encapsulated n-Graphene/p-Silicon Solar Cell.* ACS Appl Mater Interfaces, 2018. **10**(43): p. 37181-37187.

112. Rehman, M.A., S.B. Roy, D. Gwak, I. Akhtar, N. Nasir, S. Kumar, M.F. Khan, K. Heo, S.-H. Chun, and Y. Seo, *Solar cell based on vertical graphene nano hills directly grown on silicon.* Carbon, 2020. **164**: p. 235-243.
113. Kamel, M.S.A., M. Oelgemöller, and M.V. Jacob, *Chemical vapor deposition-grown graphene transparent conducting electrode for organic photovoltaics: Advances towards scalable transfer-free synthesis.* Renewable and Sustainable Energy Reviews, 2024. **203**: p. 114740.
114. Bi, H., S. Sun, F. Huang, X. Xie, and M. Jiang, *Direct growth of few-layer graphene films on SiO2substrates and their photovoltaic applications.* J. Mater. Chem., 2012. **22**(2): p. 411-416.
115. Liu, J., W. Sun, D. Wei, X. Song, T. Jiao, S. He, W. Zhang, and C. Du, *Direct growth of graphene nanowalls on the crystalline silicon for solar cells.* Applied Physics Letters, 2015. **106**(4): p. 043904.
116. Jiao, T., J. Liu, D. Wei, Y. Feng, X. Song, H. Shi, S. Jia, W. Sun, and C. Du, *Composite Transparent Electrode of Graphene Nanowalls and Silver Nanowires on Micropyramidal Si for High-Efficiency Schottky Junction Solar Cells.* ACS Appl Mater Interfaces, 2015. **7**(36): p. 20179-20183.
117. Thirumal, V., A. Pandurangan, R. Jayavel, and R. Ilangovan, *Synthesis and characterization of boron doped graphene nanosheets for supercapacitor applications.* Synthetic Metals, 2016. **220**: p. 524-532.
118. Wang, Q., J. Yan, and Z. Fan, *Carbon materials for high volumetric performance supercapacitors: design, progress, challenges and opportunities.* Energy & Environmental Science, 2016. **9**(3): p. 729-762.
119. Wang, X., G. Sun, P. Routh, D.H. Kim, W. Huang, and P. Chen, *Heteroatom-doped graphene materials: syntheses, properties and applications.* Chem Soc Rev, 2014. **43**(20): p. 7067-98.
120. Kaushal, S., M. Kaur, N. Kaur, V. Kumari, and P.P. Singh, *Heteroatom-doped graphene as sensing materials: a mini review.* RSC Adv, 2020. **10**(48): p. 28608-28629.
121. Ghotia, S., T. Rimza, S. Singh, N. Dwivedi, A.K. Srivastava, and P. Kumar, *Hetero-atom doped graphene for marvellous hydrogen storage: unveiling recent advances and future pathways.* Journal of Materials Chemistry A, 2024. **12**(21): p. 12325-12357.
122. Dong, F., Y. Cai, C. Liu, J. Liu, and J. Qiao, *Heteroatom (B, N and P) doped porous graphene foams for efficient oxygen reduction reaction electrocatalysis.* International Journal of Hydrogen Energy, 2018. **43**(28): p. 12661-12670.
123. Huang, F., L. Zhang, S. Li, J. Fu, K.H.L. Zhang, and Q. Cheng, *Direct Growth of Graphene Nanowalls on Inverted Pyramid Silicon for Schottky Junction Solar Cells.* ACS Applied Energy Materials, 2021. **4**(7): p. 6574-6584.
124. Arvas, M.B., H. Gürsu, M. Gencten, and Y. Sahin, *Preparation of different heteroatom doped graphene oxide based electrodes by electrochemical method and their supercapacitor applications.* Journal of Energy Storage, 2021. **35**: p. 102328.
125. Miao, Y., Y. Ma, and Q. Wang, *Plasma-Assisted Simultaneous Reduction and Nitrogen/Sulfur Codoping of Graphene Oxide for High-Performance Supercapacitors.* ACS Sustainable Chemistry & Engineering, 2019. **7**(8): p. 7597-7608.
126. Li, S., Z. Wang, H. Jiang, L. Zhang, J. Ren, M. Zheng, L. Dong, and L. Sun, *Plasma-induced highly efficient synthesis of boron doped reduced graphene oxide for supercapacitors.* Chem Commun (Camb), 2016. **52**(73): p. 10988-91.
127. Wang, Y., K. Zhang, R. Wang, C. Zhang, F. Kong, and T. Shao, *Plasma jet printing for preparation of N-doped graphene electrode.* Journal of Materials Science: Materials in Electronics, 2019. **30**(9): p. 8944-8954.
128. Sun, H., Q. Wang, T. Wu, Y. Miao, and Y. Fang, *Plasma-assisted synthesis of pyrrolic-nitrogen doped reduced graphene oxide to enhance supercapacitor performance.* Applied Surface Science, 2020. **527**: p. 146574.
129. Song, Y., Z. Zhao, X. Liu, Y. Yang, C. Leng, H. Zhang, J. Yu, L. Sun, X. Wang, and J. Qiu, *DBD plasma-tuned functionalization of edge-enriched graphene nanoribbons for high performance supercapacitors.* Electrochimica Acta, 2020. **337**: p. 135741.
130. Sahoo, M., K.P. Sreena, B.P. Vinayan, and S. Ramaprabhu, *Green synthesis of boron doped graphene and its application as high performance anode material in Li ion battery.* Materials Research Bulletin, 2015. **61**: p. 383-390.

131. Jing, M., T. Wu, Y. Zhou, X. Li, and Y. Liu, *Nitrogen-Doped Graphene via In-situ Alternating Voltage Electrochemical Exfoliation for Supercapacitor Application.* Front Chem, 2020. **8**: p. 428.
132. Das, T.K., S. Banerjee, A. Kumar, A.K. Debnath, and V. Sudarsan, *Electrochemical performance of hydrothermally synthesized N-Doped reduced graphene oxide electrodes for supercapacitor application.* Solid State Sciences, 2019. **96**: p. 105952.
133. Wu, S., C. Zhang, X. Cui, S. Zhang, Q. Yang, and T. Shao, *Facile synthesis of nitrogen-doped and boron-doped reduced graphene oxide using radio-frequency plasma for supercapacitors.* Journal of Physics D: Applied Physics, 2021. **54**(26): p. 265501.
134. Zhu, T., S. Li, B. Ren, L. Zhang, L. Dong, and L. Tan, *Plasma-induced synthesis of boron and nitrogen co-doped reduced graphene oxide for super-capacitors.* Journal of Materials Science, 2019. **54**(13): p. 9632-9642.
135. Seo, D.H., Z.J. Han, S. Kumar, and K. Ostrikov, *Structure-Controlled, Vertical Graphene-Based, Binder-Free Electrodes from Plasma-Reformed Butter Enhance Supercapacitor Performance.* Advanced Energy Materials, 2013. **3**(10): p. 1316-1323.

Chapter 2

Experimental Details and Characterization techniques

This chapter presents brief description of chemical routes followed for the synthesis of Graphene-based materials; CVD systems used for graphene growth on different substrates such as hot wire/filament chemical vapor deposition (HWCVD), plasma-enhanced chemical vapor deposition (PECVD) and description of rf-sputtering used for ITO deposition for fabrication of solar cells. This chapter also contains a brief description of characterization techniques (XRD, FESEM, FETEM, AFM, KPFM, XPS etc.) used for the study of different properties of thin films and solar cells.

2.1 Chemical synthesis routes for Graphene based materials

2.1.1 Preparation of Graphene Oxide by Modified Hummer's method

Graphene oxide (GO) was synthesized using Modified Hummers method where sulfuric acid (H_2SO_4) was used as exfoliating agent and potassium permanganate ($KMnO_4$) was used as oxidizing agent.[1-5] The detailed process is mentioned in chapter 3 (section 3.1.1).

2.1.2 Preparation of Reduced Graphene Oxide (r-GO)

Reduced Graphene Oxide was prepared by two ways, namely thermal reduction, and chemical reduction. In thermal reduction, GO is thermally treated at 450°C to remove oxygen-containing functional groups and obtain r-GO(T).[6-10] For chemical reduction, hydrazine hydrate acted as reducing agent to obtain r-GO(C).[11, 12] The detailed process is mentioned in section 3.1.2, chapter 3

2.1.3. Preparation of Boron doped Reduced Graphene Oxide

To synthesize boron doped r-GO samples, boric acid is used as boron source~~,~~. Boron doped reduced Graphene oxide are prepared by two different routes, by i) treating GO with boric acid and then reducing it and ii) by treating r-GO with boric acid. The detailed process can be found in section 3.1.3 of chapter 3.

2.2 Film preparation and Device Fabrication Techniques

Single and multi-layer Graphene can be prepared by various techniques such as Hot-wire Chemical Vapor Deposition (HWCVD), dual zone CVD, Plasma-enhanced Chemical Vapor Deposition (PECVD)` and by chemical routes. In our work, we have used Hot-wire CVD, and rf-PECVD for depositing Graphene film on Nickel and silicon substrates.

2.2.1 Hot wire chemical vapor deposition (HWCVD)

HWCVD is a widely used thin film fabrication technique. In this method, precursor gases are thermally and catalytically dissociated into reactive radicals as they pass through a high-temperature filament, typically heated to 2000-2200°C. Filament materials, including tungsten, tantalum, and molybdenum, are commonly used in HWCVD. This technique offers several advantages over conventional CVD methods, such as the ability to grow films at lower substrate temperatures, high gas decomposition efficiency, large-area deposition capability, and

the absence of ion bombardment on the growing film surface. Additionally, by adjusting deposition parameters, the microstructure of the film can be controlled, ranging from amorphous to nano- or micro-crystalline phases. For the synthesis of various carbon allotropes, precursor gases such as CH_4, C_2H_2, CF_4, and C_2F_6 can be employed in the HWCVD process. In this study, methane (CH_4) is used as the carbon source for graphene growth. Due to methane's relatively low decomposition efficiency, a high filament temperature is necessary to achieve sufficient dissociation for film formation. Hydrogen (H_2) is used as both a carrier gas and a diluent, aiding the formation of crystalline phases by reducing dangling carbon bonds.

Figure 2.2 shows a schematic of a general HWCVD system, while Figure 2.3 depicts the specific system used in this work. The HWCVD setup consists of two cylindrical stainless-steel chambers (304 grade), separated by a gate valve. One chamber function as the deposition chamber, and the other serves as the load-lock chamber. The system includes a high-temperature, water-cooled substrate heater capable of reaching up to 950°C.

The system is designed with flexibility, allowing the vertical adjustment of the substrate heater to control the distance between the filament and the substrate. In addition, the filament and gas inlets are enclosed by a stainless-steel gas confinement assembly, which enhances the dissociation efficiency of the precursor gases.

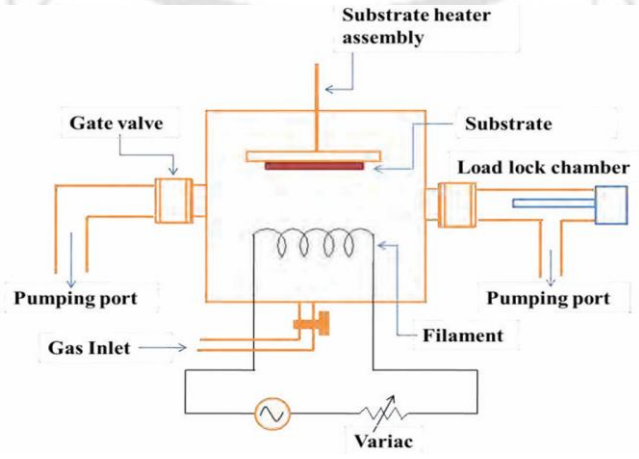

Fig. 2.1: Schematic of HWCVD system

To achieve the growth of single and multi-layer graphene by HWCVD, several deposition parameters, such as process pressure (PP), substrate temperature (T_s), CH_4/H_2 gas flow rates, and substrate choices (c-Si and Ni foil), were systematically varied. [13, 14] Detailed conditions for these parameters are described in Chapters 4 and 5. For the preparation of graphene thin films, high-purity methane (CH_4) and hydrogen (H_2) gases (99.99% purity) were used. To minimize contamination and maintain consistency, a new tantalum filament was used for each deposition. The filament, with a diameter of 0.5 mm, was arranged in a parallel configuration with three 7 cm-long wires, enabling the filament temperature to be maintained in the range of 2000-2200°C. The substrates were heated by a radiative heater positioned 0.5 mm above the substrate holder. Before deposition, the chamber was evacuated to a pressure below 10^{-6} mbar using a turbo molecular pump, which ran for 5-6 hours to ensure a clean environment.

Fig. 2.2: HWCVD system in our lab

2.2.2 rf-Sputtering

In this thesis, indium-tin-oxide (ITO) and silver (Ag) have been selected as materials for the transparent conducting layer and electrical contacts, respectively, in the device fabrication process. These layers were deposited using radio frequency (RF) sputtering, a physical vapor deposition (PVD) technique based on the physical ejection of atoms from a solid target due to bombardment by energetic gas ions.[15-22] Before the sputtering process, the chamber is

evacuated to a base pressure of approximately 10^{-7} mbar. Once this vacuum level is achieved, a controlled flow of inert argon (Ar) gas is introduced into the chamber. A high voltage is applied between the electrodes, the target (cathode) and the substrate (anode) causing the Ar gas to ionize. The resulting Ar ions are accelerated toward the cathode, where they strike the target surface, causing the ejection of target atoms.

The sputtered atoms travel toward the grounded anode and adhere to the substrate, forming a thin film. This process allows for the controlled deposition of uniform and high-quality conductive layers, which are essential for the device's performance

2.2.3. rf-PECVD

The rf-PECVD technique is most commonly used deposition method to produce device quality hydrogenated amorphous silicon (*a-Si:H*) thin films but recently it is being used for the direct growth of graphene on silicon substrates.[23-29] The role of the plasma in this technique is to provide a source of energy to dissociate methane (CH_4) molecules. CH_4 is dissociated into CH_n ($n \leq 3$) as well as H_2 and H [30]. Hydrogen molecules are also decomposed into atomic hydrogen. Excitation of the ground state electron to the vacuum state gives rise to ionization events, generating new electrons and ions to maintain the plasma. The plasma is confined between two parallel plates, one of which holds the substrate.

The radicals formed in secondary gas phase reactions and then get deposited on the substrate, yielding the film. Radio frequency plasma enhanced chemical vapour deposition (RF-PECVD) (13.56 MHz) multi-chamber system (EXCEL instruments, Mumbai, India) has been used for the deposition of thin films and fabrication of solar cells. Figure 2.4 (a) shows the schematic diagram of the RF-PECVD multi-chamber system and Figure 2.4 (b) show the real image of RF-PECVD multi-chamber. The system consists of four cylindrical chambers made of stainless steel (SS304 grade), three (PECVD) chambers and a central load lock cum hot wire chemical

vapour deposition (HWCVD) chamber. All the three PECVD chambers are separated from load lock chamber (i.e. HWCVD) using CF100 gate valve. The substrate can be transferred from one PECVD chamber to other PECVD chamber through load-lock without breaking the vacuum. This prevents contamination of other chambers. All the process chambers are individually connected to a turbo-molecular pump (TMP) (Pfieffer, HIPAC 300) with a gate valve between them. The TMP is backed by a two-stage rotary pump (Pfieffer, PASCAL 2020SD). Exhaust line of each rotary pump is connected to the burn box. During deposition, burn box temperature is kept at 700 ºC and these burnt gases were dissolved in the soap water before going to atmosphere. Cold water is supplied to the TMP and burn box and one fan was attached to each TMP to keep it cool. Pirani and penning gauges are used to monitor the pressure inside the chambers. Separate gas lines are used to feed the reactant gases in these chambers.

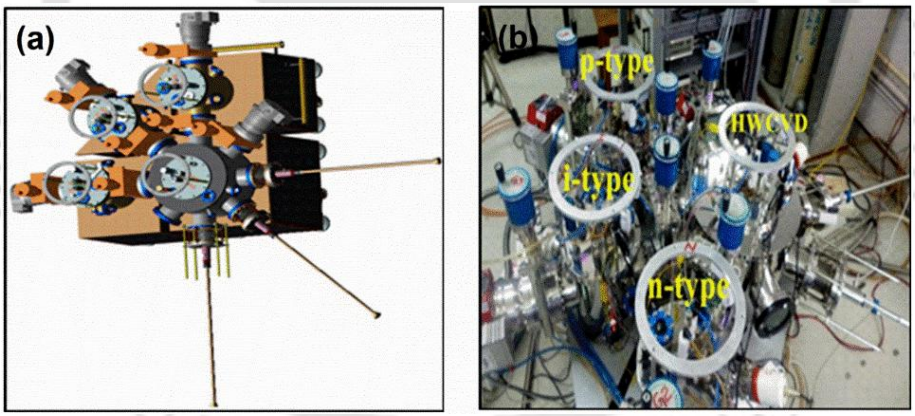

Fig. 2.3: (a) Schematic diagram of RF- PECVD multi-chamber system (b) real image of RF-PECVD multi-chamber

2.2.4. Thermal evaporation Deposition

Thermal evaporation is a widely used Physical Vapor Deposition (PVD) technique for thin film fabrication. It is a simple yet effective method that relies on a resistively heated filament or boat made from refractory materials such as tungsten (W), molybdenum (Mo), or tantalum (Ta). The solid evaporant is heated in a high-vacuum chamber until it transforms into vapor,

which then condenses onto a substrate to form a thin film. The system primarily consists of a vacuum chamber, vacuum pumps, a heating filament or boat, and a substrate holder, which may include a heating element.[31]The deposition process involves the sublimation of the solid evaporant, the transfer of vapor to the substrate, condensation upon arrival, and subsequent structural modifications on the substrate surface. This technique is commonly employed for depositing metallic electrical contacts such as gold, silver, and aluminium in thin-film devices, including solar cells, LEDs, and thin-film transistors (TFTs). It also enables co-evaporation of multiple materials, where precise temperature control ensures the desired film stoichiometry. The evaporation rate and condensation behaviour vary depending on the source material and deposition conditions.[32, 33]

In this thesis, we used thermal evaporation deposition system for the deposition of silver and aluminium as contacts in solar cells. The quality of the deposited films is influenced by factors such as evaporation rate, deposition pressure, film thickness, evaporation angle, substrate temperature, and residual gas composition. These parameters can be precisely controlled in the thermal evaporation process, ensuring uniform and high-quality film deposition. A key advantage of this method is its ability to achieve large-area thin films with consistent thickness, making it a reliable choice for applications in electronics and materials science.

2.3 Characterization Techniques

The powder and thin films prepared using above-mentioned methods were characterized for studying its structural, optical and electrical properties using different experimental techniques described below.

2.3.1 Raman Spectroscopy

Raman spectroscopy is one of the non-destructive and very powerful tools to study vibrational modes of a material for understanding the crystal structure and many other fundamental

properties. Raman scattering is an inelastic scattering phenomenon of photons by the fluctuations such as atomic vibrations, charge density and spin density and so on in the material. Positions of the peaks are related to the inter-atomic forces and distances, to their masses and chemical environments.[34-38] Raman studies reported in this thesis were performed using HORIBA Jobin-Yvon LabRam HR Raman spectroscopy equipped with Ar-ion laser at a wavelength of 488 nm. The spot size of the laser beam was 1 μm in diameter and the incident laser power on the sample was less than 1 mW. These studies were carried out at room temperature (*RT*) in the backscattering geometry.

2.3.2 X-ray Diffraction

X-ray diffractometer, Rigaku TTRAX III, 18 kW with CuK_a radiation of 1.54 Å, was used for microstructure investigations. The measurements were performed in 2θ thin film mode at a grazing angle of incidence of 3°. The samples were scanned in the range of 10-70° with a step of 0.05°. The crystallite size in the film was calculated using Scherrer's formula[39] (Equation 2.1) as follows

$$d_{XRD} = \frac{0.9\lambda}{B_1 Cos\theta_{hkl}} \tag{2.1}$$

where d_{XRD} is the crystallite size, l is the wavelength of X-ray, B_1 is the broadening due to crystallite size and θ_{hkl} is the peak position corresponding to the (hkl) plane.

2.3.3 Field emission transmission electron microscopy

To analyse the structure of graphene, transmission electron microscopy (FETEM) studies were performed. The JEOL-2100 was used to capture FETEM selective area electron refraction SAED patterns and high-resolution pictures and crystalline were determined using t e m in dark field mode with a 200KW accelerating voltage and lab 6 filament for measurements the

graphene were grown directly on nickel mesh great using imageJ software the HRTEM pictures are utilise to quantify that is facing the spacing of distinct atoms.

2.3.4 Field emission scanning electron microscopy

Surface morphology of the films and cross-sectional image of solar cells were recorded by field emission scanning electron microscopy (FESEM, model: SIGMA ZEISS). In this technique, a field emission cathode provides narrow electron beam of high energy which is focused on the sample and result in improvement of resolution of the image. FESEM was operated with an accelerating voltage of 2 to 4 KeV and films were coated with a very thin gold layer with the plasma to avoid charging effect during measurement.

2.3.5 Atomic Force Microscopy

Atomic force microscopy (AFM) is one of the useful tools to observe surface topography of the films. AFM consists of a microscale cantilever with a sharp tip at its end that is used to scan the surface of the film. Cantilever is generally made with Silicon or silicon nitride. When the tip is brought close to the film surface, the force between film and tip leads to a deflection of the cantilever. The deflection is measured using a laser spot reflected from the top surface of the cantilever into an array of photodiodes.[40-42] In this thesis, the measurements were performed with AFM (model Agilent, 5500 series) in tapping mode using silicon nitride cantilever with force constant 33 N/m and a resonance frequency of 304 KHz. The root mean square (RMS) roughness of films is calculated using "WSxM" software for the selected areas.

2.3.6 Fourier transform infrared spectroscopy

Fourier transform infrared (FTIR) spectroscopy is a non-destructive technique which can identify the bond configuration in the material. This instrument works based on the fact that each molecular bond has its own distinct quantized vibrational levels whose frequency lie usually in the mid-infrared region of 200 - 4000 cm^{-1}. Once the frequency of an incident

infrared radiation matches with the frequency of molecular vibration modes, radiation is absorbed by the molecules.[43-45] A single beam 'Perkin Elmer BX' FTIR spectrometer is used to record the IR transmission spectra for all prepared samples. The films are deposited on IR transparent substrate such as both sides polished undoped monocrystalline Si (100) wafer. The spectrometer is operated using normal incidence with step size of 1 cm^{-1} and resolution of 4 cm^{-1} with average of sixty-four scans for each sample.

2.3.7 Energy dispersive X-ray spectroscopy

Energy Dispersive X-ray Spectroscopy (EDS) is a widely used analytical technique in materials science to determine the elemental composition of a sample. The technique is based on the detection of characteristic X-rays emitted by elements when their atoms interact with a high-energy electron beam. When an electron beam strikes a sample, it displaces electrons from the inner shells of atoms, creating vacancies. These vacancies are filled by electrons from higher energy levels, and in the process, characteristic X-rays are emitted. The energy of these emitted X-rays is unique to each element, allowing for precise elemental identification. The transitions of electrons between different energy levels are classified into K-series, L-series, and M-series, depending on the shell involved. For effective EDS analysis, the energy supplied must exceed the ionization energy of the element being analysed. The accelerating voltage of the electron beam plays a crucial role in this process.[46-51] In our study, an accelerating voltage of 20 kV in SE2 mode was used for EDS analysis to determine the atomic and weight percentages of silicon, carbon, and oxygen in graphene films. Additionally, it was employed to analyse carbon, boron, and oxygen in graphene oxide, reduced graphene oxide, and boron-doped reduced graphene oxide samples. This technique provides valuable insights into the composition of materials, aiding in the characterization and optimization of various thin-film and nanomaterial applications.

2.3.8 X-ray photoelectron Spectroscopy

X-ray Photoelectron Spectroscopy (XPS) is a powerful analytical technique used to determine the elemental composition, chemical states, and electronic structure of elements present on the surface of a material. It is highly surface-sensitive, typically analysing depths up to 10 nm. However, depth profiling can be performed by sputtering the surface layer, allowing for an understanding of compositional variations from the surface to the bulk of the material. In XPS, an X-ray beam excites atoms on the material's surface, causing the emission of photoelectrons. By analysing the energy of these emitted electrons, valuable insights into the elemental composition and chemical bonding states can be obtained. XPS operates with photon energies ranging from 200 to 2000 eV, making it suitable for studying both conducting and non-conducting materials. Additionally, the technique maintains a stable charge state on the sample surface, enabling precise surface characterization.[52, 53]

This method is widely used in materials science for investigating thin films, coatings, and nanomaterials, providing crucial information about surface chemistry and electronic properties. We have used this for our graphene films deposited on silicon substrates to get the information about Carbon-silicon and carbon-carbon bonds.

2.3.9 Kelvin Probe Force Microscopy

Kelvin Probe Force Microscopy (KPFM) is a powerful technique used to measure the local work function of thin films, including graphene-based materials. The term "local work function" is used because measurements are performed in ambient conditions, where surface adsorbates can influence the results.[54] KPFM operates by measuring the contact potential difference (CPD) between a conducting tip and the sample surface. This CPD value is then used to determine the sample's work function. The technique is based on the principle that when a conductive tip is brought close to a sample, electron tunnelling occurs, causing a shift

in the Fermi levels of both the tip and the sample until they reach equilibrium. This alignment of energy levels generates a contact potential difference, which induces an electrical force. To nullify this force, an external DC voltage is applied, equal and opposite to the CPD, restoring the Fermi levels to their original state. The applied voltage corresponds to the difference in work functions between the sample and the tip. The work function of the sample is calculated using a reference material, often Highly Oriented Pyrolytic Graphite (HOPG), due to its stability against contamination and minimal dipole formation.[55-58]

In this study, KPFM measurements were carried out using an Oxford Instruments Cypher S microscope to analyse the work function of as-deposited graphene films on silicon substrates. The ability of KPFM to provide high-resolution surface potential mapping makes it an essential tool for studying electronic properties of thin films and nanomaterials.

2.3.10 Conductivity measurements

Conductivity of thin films were measured using two probe method in coplanar geometry. Silver paint was used as electrodes for conductivity measurements. In coplanar geometry, if l is the length of electrodes, d is the separation between them, t is the thickness of the film, V is the applied voltage and I is the measured current then the conductivity is given by the following Equation 2.2

$$\sigma = \frac{I \times d}{V \times l \times t} \tag{2.2}$$

A Solar Simulator (model: Sciencetech) was used for to illuminate the films during photoconductivity measurements.

2.3.11 Surface Profilometer

A Surface profilometer is used to measure the thickness of deposited films. It is capable to scan area of tens of millimeters with a vertical range starting from hundreds of microns to a few

nanometers. In the present thesis, measurements were carried out using Veeco-Dektak 150 stylus profilometer. Thickness measurement was performed for each film at three different mask locations and those values were averaged to determine the thickness.

2.4 Solar cell characterization

2.4.1 Current density (*J*) – Voltage (*V*) measurement

Electrical performance of a solar cell was determined from the current density-voltage (*J-V*) curve obtained by illuminating the solar cell with solar simulator (model: ScienceTech) under AM1.5. Intensity of light beam falling on the sample was about 100 mW/cm^2. A Keithley 2450 Source meter controlled by a computer is used to provide voltage sweeps and record the corresponding current. An example of current density-voltage characteristic of solar cell is illustrated in Fig. 2.4.

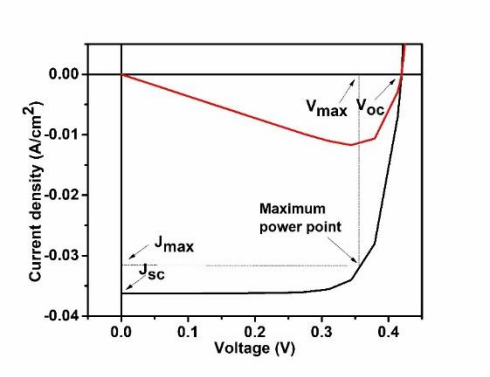

Fig. 2.4: Current density (J) - voltage (V) characteristics of solar cell

From the *J-V* curve, short-circuit current density (J_{sc}), open-circuit voltage (V_{oc}) and fill factor (*FF*) are obtained. The solar cell efficiency (η) is defined as the ratio of maximum electrical energy output to the incident solar energy on the cell. The η (%) is determined by the following Equation 2.3 [59].

$$\eta(\%) = \frac{J_{sc} \times V_{oc} \times FF}{P_{in}} \times 100 \qquad (2.3)$$

$$\text{where} \quad FF = \frac{J_{\max} \times V_{\max}}{J_{sc} \times V_{oc}}$$

where J_{sc}, V_{oc}, FF and P_{in} are short-circuit current density, open-circuit voltage, fill factor and input power. The V_{oc} is the voltage at which no current flows through the external circuit; that is at $J = 0$. On the other hand, J_{sc} is current density at which voltage drop is zero across the solar cell. The FF is the ratio of the maximum power that can be obtained from the cell to the product of J_{sc} and V_{oc}. It is a measure of 'squareness' of the J-V curve and describes the operating point at which the solar cell gives maximum power to the attached load.

2.5 Simulation studies of Graphene-Silicon heterojunction Solar cells

The simulation studies of Graphene/ silicon heterojunction solar cells is performed using a user-friendly software AFORS-HET (Automat FOR Simulation of HETero structures) v-2.5 under AM1.5 illumination and power density of 100mW/cm^2.

2.6 References

1. Kigozi, M., R.K. Koech, O. Kingsley, I. Ojeaga, E. Tebandeke, G.N. Kasozi, and A.P. Onwualu, *Synthesis and characterization of graphene oxide from locally mined graphite flakes and its supercapacitor applications.* Results in Materials, 2020. **7**: p. 100113.
2. Chen, X., Z. Qu, Z. Liu, and G. Ren, *Mechanism of Oxidization of Graphite to Graphene Oxide by the Hummers Method.* ACS Omega, 2022. **7**(27): p. 23503-23510.
3. Santamaría-Juárez, G., E. Gómez-Barojas, E. Quiroga-González, E. Sánchez-Mora, M. Quintana-Ruiz, and J.D. Santamaría-Juárez, *Safer modified Hummers' method for the synthesis of graphene oxide with high quality and high yield.* Materials Research Express, 2020. **6**(12): p. 125631.
4. Panicker, N.J., J. Das, and P.P. Sahu, *Synthesis of highly oxidized graphene (HOG) by using HNO3 and KMnO4 as oxidizing agents.* Materials Today: Proceedings, 2021. **46**: p. 6270-6274.
5. Jannah, W.N., S. Sunaryono, and N. Mufti, *Synthesis graphene oxide based on modified Hummer's method*, in *The Ii International Scientific Conference "Industrial and Civil Construction 2022"*. 2023. p. 020009.
6. Öztekin, D., H. Arbağ, and S. Yaşyerli, *Preparation of RGO with Enhanced Electrical Conductivity: Effects of Sequential Reductions of L-Ascorbic Acid and Thermal.* Arabian Journal for Science and Engineering, 2025. **50**: p. 9905-9918.
7. Mokoloko, L.L., B.J. Matsoso, R.P. Forbes, D.H. Barrett, B.D. Moreno, and N.J. Coville, *Evolution of large-area reduced graphene oxide nanosheets from carbon dots via thermal treatment.* Carbon Trends, 2021. **4**: p. 100074.
8. Gomez-Mancebo, M.B., R. Fernandez-Martinez, A. Ruiz-Perona, V. Rubio, P. Bastante, F. Garcia-Perez, F. Borlaf, M. Sanchez, A. Hamada, A. Velasco, Y.K. Ryu, F. Calle, L.J. Bonales, A.J. Quejido, J. Martinez, and I. Rucandio, *Comparison of Thermal and Laser-Reduced*

Graphene Oxide Production for Energy Storage Applications. Nanomaterials (Basel), 2023. **13**(8): p. 1391.
9. Valentini, C., V. Montes-Garcia, P.A. Livio, T. Chudziak, J. Raya, A. Ciesielski, and P. Samori, *Tuning the electrical properties of graphene oxide through low-temperature thermal annealing.* Nanoscale, 2023. **15**(12): p. 5743-5755.
10. Li, X., H. Zhu, K. Wang, A. Cao, J. Wei, C. Li, Y. Jia, Z. Li, X. Li, and D. Wu, *Graphene-on-silicon Schottky junction solar cells.* Adv Mater, 2010. **22**(25): p. 2743-2748.
11. Chudziak, T., V. Montes-Garcia, W. Czepa, D. Pakulski, A. Musial, C. Valentini, M. Bielejewski, M. Carlin, A. Tubaro, M. Pelin, P. Samori, and A. Ciesielski, *A comparative investigation of the chemical reduction of graphene oxide for electrical engineering applications.* Nanoscale, 2023. **15**(44): p. 17765-17775.
12. Chen, H., L. Ding, K. Zhang, Z. Chen, Y. Lei, Z. Zhou, and R. Hou, *Preparation of chemically reduced graphene using hydrazine hydrate as the reduction agent and its NO2 sensitivity at room temperature.* International Journal of Electrochemical Science, 2020. **15**(10): p. 10231-10242.
13. Anuar, N.A., N.H.M. Nor, M.Y. Chia, B.T. Goh, W.S. Chiu, Z. Aspanut, R. Awang, H. Nakajima, S. Tunmee, M. Sookhakian, and Y. Alias, *Improved photoelectrochemical performance of tungsten-catalyzed graphene nanoplatelet electrodes prepared by hot-wire chemical vapor deposition at low substrate temperatures.* Thin Solid Films, 2024. **797**: p. 140330.
14. Anuar, N.A.b., N.H.M. Nor, R.b. Awang, H. Nakajima, S. Tunmee, M. Tripathi, A. Dalton, and B.T. Goh, *Low-temperature growth of graphene nanoplatelets by hot-wire chemical vapour deposition.* Surface and Coatings Technology, 2021. **411**: p. 126995.
15. Miao, Y., Y. Ma, and Q. Wang, *Plasma-Assisted Simultaneous Reduction and Nitrogen/Sulfur Codoping of Graphene Oxide for High-Performance Supercapacitors.* ACS Sustainable Chemistry & Engineering, 2019. **7**(8): p. 7597-7608.
16. Barman, B., S.K. Swami, and V. Dutta, *Fabrication of highly conducting ZnO/Ag/ZnO and AZO/Ag/AZO transparent conducting oxide layers using RF magnetron sputtering at room temperature.* Materials Science in Semiconductor Processing, 2021. **129**: p. 105801.
17. Tchenka, A., A. Agdad, M.C. Samba Vall, S.K. Hnawi, A. Narjis, L. Nkhaili, E. Ibnouelghazi, E. Ech-Chamikh, and M. Zheludkevich, *Effect of RF Sputtering Power and Deposition Time on Optical and Electrical Properties of Indium Tin Oxide Thin Film.* Advances in Materials Science and Engineering, 2021. **2021**(1): p. 1-14.
18. Bertran, E., *RF sputtering deposition of Ag/ITO coatings at room temperature.* Solid State Ionics, 2003. **165**(1-4): p. 139-148.
19. Sousa, M.G. and A.F. da Cunha, *Optimization of low temperature RF-magnetron sputtering of indium tin oxide films for solar cell applications.* Applied Surface Science, 2019. **484**: p. 257-264.
20. Gudmundsson, J.T., A. Anders, and A. von Keudell, *Foundations of physical vapor deposition with plasma assistance.* Plasma Sources Science and Technology, 2022. **31**(8): p. 083001.
21. Gudmundsson, J.T., *Physics and technology of magnetron sputtering discharges.* Plasma Sources Science and Technology, 2020. **29**(11): p. 113001.
22. Ghulam, A.N., O.A.L. Dos Santos, L. Hazeem, B. Pizzorno Backx, M. Bououdina, and S. Bellucci, *Graphene Oxide (GO) Materials-Applications and Toxicity on Living Organisms and Environment.* J Funct Biomater, 2022. **13**(2): p. 77.
23. Chen, W., R. Cariou, G. Hamon, R. Léal, J.-L. Maurice, and P.R.i. Cabarrocas, *Influence of deposition rate on the structural properties of plasma-enhanced CVD epitaxial silicon.* Scientific Reports, 2017. **7**: p. 43968.
24. He, J., C. Wang, W. Li, K.C. Qi, and Y.D. Jiang, *Effect of gas temperature on the structural and optoelectronic properties of a-Si:H thin films deposited by PECVD.* Surface & Coatings Technology, 2013. **214**: p. 131-137.
25. Anutgan, T. and S. Uysal, *Low temperature plasma production of hydrogenated nanocrystalline silicon thin films.* Current Applied Physics, 2013. **13**(1): p. 181-188.

26. Han, Y., B.J. Park, J.H. Eom, V. Jella, S. Ippili, S.V.N. Pammi, J.S. Choi, H. Ha, H. Choi, C. Jeon, K. Park, H.T. Jung, S. Yoo, H.Y. Kim, Y.H. Kim, and S.G. Yoon, *Direct Growth of Highly Conductive Large-Area Stretchable Graphene.* Adv Sci (Weinh), 2021. **8**(7): p. 2003697.
27. Guo, L., Z. Zhang, H. Sun, D. Dai, J. Cui, M. Li, Y. Xu, M. Xu, Y. Du, N. Jiang, F. Huang, and C.-T. Lin, *Direct formation of wafer-scale single-layer graphene films on the rough surface substrate by PECVD.* Carbon, 2018. **129**: p. 456-461.
28. Bekdüz, B., Y. Beckmann, J. Mischke, J. Twellmann, W. Mertin, and G. Bacher, *Graphene growth through a recrystallization process in plasma enhanced chemical vapor deposition.* Nanotechnology, 2018. **29**(45): p. 455603.
29. Miao, R.-X., C.-H. Zhao, S.-Q. Wang, W. Ren, Y.-F. Li, T.-K. Shu, and B. Yang, *Direct growth of graphene films without catalyst on flexible glass substrates by PECVD*.* Chinese Physics B, 2021. **30**(9): p. 098101.
30. Ramanujam, J. and A. Verma, *Photovoltaic Properties of a-Si:H Films Grown by Plasma Enhanced Chemical Vapor Deposition: A Review.* Materials Express, 2012. **2**(3): p. 177-196.
31. Stadler, B.J.H., *Vapor Processes*, in *Materials Processing*. 2016. p. 513-588.
32. Toma, F.T.Z., M.S. Rahman, K.M.A. Hussain, and S. Ahmed, *Thin Film Deposition Techniques: A Comprehensive Review.* Journal of Modern Nanotechnology, 2024. **4**: p. 6.
33. Oluwatosin Abegunde, O., E. Titilayo Akinlabi, O. Philip Oladijo, S. Akinlabi, and A. Uchenna Ude, *Overview of thin film deposition techniques.* AIMS Materials Science, 2019. **6**(2): p. 174-199.
34. Olubiyi, O.I., F.-K. Lu, D. Calligaris, F.A. Jolesz, and N.Y. Agar, *Advances in Molecular Imaging for Surgery*, in *Image-Guided Neurosurgery*. 2015. p. 407-439.
35. Deluca, M., H. Hu, M.N. Popov, J. Spitaler, and T. Dieing, *Advantages and developments of Raman spectroscopy for electroceramics.* Communications Materials, 2023. **4**(1): p. 1-15.
36. Saletnik, A., B. Saletnik, and C. Puchalski, *Overview of Popular Techniques of Raman Spectroscopy and Their Potential in the Study of Plant Tissues.* Molecules, 2021. **26**(6): p. 1537.
37. Cong, X., X.-L. Liu, M.-L. Lin, and P.-H. Tan, *Application of Raman spectroscopy to probe fundamental properties of two-dimensional materials.* npj 2D Materials and Applications, 2020. **4**(1): p. 1-12.
38. Wu, J.B., M.L. Lin, X. Cong, H.N. Liu, and P.H. Tan, *Raman spectroscopy of graphene-based materials and its applications in related devices.* Chem Soc Rev, 2018. **47**(5): p. 1822-1873.
39. B.D. Cullity, S.R.S., *Elements of X-Ray Diffraction*: p. 174
40. Sheppard, C.J.R., *MICROSCOPY | Overview*, in *Encyclopedia of Modern Optics*. 2005. p. 61-69.
41. Alunda, B.O. and Y.J. Lee, *Review: Cantilever-Based Sensors for High Speed Atomic Force Microscopy.* Sensors (Basel), 2020. **20**(17): p. 4784.
42. Hansma, P.K., V.B. Elings, O. Marti, and C.E. Bracker, *Scanning tunneling microscopy and atomic force microscopy: application to biology and technology.* Science, 1988. **242**(4876): p. 209-216.
43. Yusuf, M.O., *Bond Characterization in Cementitious Material Binders Using Fourier-Transform Infrared Spectroscopy.* Applied Sciences, 2023. **13**(5): p. 3353.
44. Modupalli, N., M. Naik, C.K. Sunil, and V. Natarajan, *Emerging non-destructive methods for quality and safety monitoring of spices.* Trends in Food Science & Technology, 2021. **108**: p. 133-147.
45. Pasieczna-Patkowska, S., M. Cichy, and J. Flieger, *Application of Fourier Transform Infrared (FTIR) Spectroscopy in Characterization of Green Synthesized Nanoparticles.* Molecules, 2025. **30**(3): p. 684.
46. Hajizadeh, Z., R. Taheri-Ledari, and F.R. Asl, *Identification and analytical methods*, in *Heterogeneous Micro and Nanoscale Composites for the Catalysis of Organic Reactions*. 2022. p. 33-51.
47. Tshabalala, Z.P., D.N. Oosthuizen, H.C. Swart, and D.E. Motaung, *Tools and techniques for characterization and evaluation of nanosensors*, in *Nanosensors for Smart Cities*. 2020. p. 85-110.

48. Cornu, R., G. Laurent, and A. Beduneau, *Preparation and characterization of PLGA nanoparticles*, in *Poly(lactic-co-glycolic acid) (PLGA) Nanoparticles for Drug Delivery*. 2023. p. 27-54.
49. Shirazi, M., G.M. Rad, and Y. Tamsilian, *Polymer Nanocomposite Characterization and Applications*, in *Encyclopedia of Materials: Composites*. 2021. p. 725-745.
50. Mudalige, T., H. Qu, D. Van Haute, S.M. Ansar, A. Paredes, and T. Ingle, *Characterization of Nanomaterials*, in *Nanomaterials for Food Applications*. 2019. p. 313-353.
51. Scimeca, M., S. Bischetti, H.K. Lamsira, R. Bonfiglio, and E. Bonanno, *Energy Dispersive X-ray (EDX) microanalysis: A powerful tool in biomedical research and diagnosis.* Eur J Histochem, 2018. **62**(1): p. 2841.
52. Giri, T.K., *Solid lipid nanoparticles for the delivery of drug molecules*, in *Materials for Biomedical Engineering*. 2019. p. 551-576.
53. Ferreira, L.A.B., S.B. Dos Reis, E. do Nascimento da Silva, S. Cadore, J.D.S. Bernardes, N. Duran, and M.B. de Jesus, *Thiol-antioxidants interfere with assessing silver nanoparticle cytotoxicity.* Nanomedicine, 2020. **24**: p. 102130.
54. Farias, E.D., M.E. Zoloff Michoff, V. Sueldo Occello, V. Brunetti, M.C.G. Passeggi, and T. Glatzel, *KPFM and DFT as tools to correlate the charge distribution and molecular orientation of dendritic adsorbates on different surfaces.* Applied Surface Science, 2021. **565**: p. 150552.
55. Checa, M., A.S. Fuhr, C. Sun, R. Vasudevan, M. Ziatdinov, I. Ivanov, S.J. Yun, K. Xiao, A. Sehirlioglu, Y. Kim, P. Sharma, K.P. Kelley, N. Domingo, S. Jesse, and L. Collins, *High-speed mapping of surface charge dynamics using sparse scanning Kelvin probe force microscopy.* Nat Commun, 2023. **14**(1): p. 7196.
56. Collins, L., R.K. Vasudevan, and A. Sehirlioglu, *Visualizing Charge Transport and Nanoscale Electrochemistry by Hyperspectral Kelvin Probe Force Microscopy.* ACS Appl Mater Interfaces, 2020. **12**(29): p. 33361-33369.
57. Glatzel, T., S. Sadewasser, R. Shikler, Y. Rosenwaks, and M.C. Lux-Steiner, *Kelvin probe force microscopy on III–V semiconductors: the effect of surface defects on the local work function.* Materials Science and Engineering: B, 2003. **102**(1-3): p. 138-142.
58. Lee, H., W. Lee, J.H. Lee, and D.S. Yoon, *Surface Potential Analysis of Nanoscale Biomaterials and Devices Using Kelvin Probe Force Microscopy.* Journal of Nanomaterials, 2016. **2016**: p. 1-21.
59. Belfar, A., *Simulation study of the a-Si:H/nc-Si:H solar cells performance sensitivity to the TCO work function, the band gap and the thickness of i-a-Si:H absorber layer.* Solar Energy, 2015. **114**: p. 408-417.

Chapter 3

Synthesis and Characterization of doped and undoped Graphene-based materials by chemical route

The synthesis of Graphene Oxide by Modified Hummer's method[1-5] and its further conversion to reduced Graphene Oxide is discussed here. We have followed two routes for the reduction process, one is chemical reduction and another one is thermal reduction. The comparative analysis of the chemically and thermally reduced r-GO samples based on their specific surface area, electrical conductivity and other structural properties are also discussed. Further, bulk synthesis of boron-doped reduced graphene oxide (B-rGO) as an electrode material for supercapacitors [6-11] by using Boric acid (H_3BO_3) as boron source is also discussed. The structural properties of B-rGO, in comparison with Graphene Oxide (GO), Graphite and reduced Graphene Oxide(r-GO) has been studied by XRD, Raman and FETEM analysis. The boron doping of ~9% has been confirmed by EDAX analysis. An increase in

inter-layer spacing from 0.23nm to 0.28nm has been observed in B-rGO due to intercalation of boron atom in the lattice. FTIR studies also confirmed the doping due to presence of B-C and B-O bond. We have reported an increased specific capacitance of 326.56 F/g for B-rGO compared to GO (137.88 F/g) and r-GO (108.85 F/g). The corresponding structural properties have also been studied by XRD and Raman and electrical conductivity is also calculated. For all the chemically prepared samples i.e. GO, r-GO, B-rGO and r-BGO, thermal kinetics study is done to estimate the activation energies and entropy changes at various stages of degradation with temperature.

3.1 Experimental details

3.1.1 Preparation of Graphene Oxide by Modified Hummer's method

Graphene oxide (GO) was synthesized using Modified Hummers method. In this method, 250 mg graphite and 9ml sulfuric acid (H_2SO_4) were mixed and stirred for 3 hours at room temperature at 550rpm. Now, 750mg potassium permanganate ($KMnO_4$) was grind and gradually added into the solution with constant stirring. An ice bath is provided while adding $KMnO_4$ as this reaction is exothermic in nature. The mixture was kept on stirrer at 45°C until the color of the solution became reddish. Now the solution was diluted by adding 25 ml DI water and the mixture was heated at 90°C for half an hour. The solution was further diluted by adding another 75ml DI water and 30% H_2O_2 solution (5ml) into it. The solution became greenish yellow in color. The mixture is washed with 5% HCl (1.42ml HCl of 30% +8.58ml water) followed by DI water until the pH became neutral. Then, the solution is centrifuged twice at 4000 rpm for 30 minutes. The resulting solution obtained is brownish in color. The solution is filtered and dried into the Vacuum Oven. Finally, GO powder was obtained.

For making thin films of Graphene Oxide, GO powder is dissolved in NMP (N-Methyl-2-Pyrrolidone) (15mg/ml) and the resulting solution is sonicated for 5hrs. GO films are

deposited on 1cm X 1cm quartz, undoped silicon and FTO substrate by drop casting using 30µl of the obtained solution. The thickness of the film could be controlled by the optimized concentration of the solution. Film Thickness was measured by using stylus Profilometer.

3.1.2 Preparation of Reduced Graphene Oxide (r-GO)

1. Thermal reduction: GO powder (50mg) is placed in a crucible and kept in a muffle furnace at 450°C for 1h for thermal reduction. After 1hour of thermal reduction, the sample was cooled to room temperature and black coloured Reduced Graphene Oxide (r-GO(T)) powder is obtained. The oxygen-containing functional groups from graphene oxide were removed by this process.

2. Chemical reduction: In this process, 50mg of Graphene Oxide is mixed with 50mL of DI water and sonicated in ultrabath sonicator for 3hrs. After this, 3mL of hydrazine hydrate is added to the solution which acts as a reducing agent and the solution is kept on the magnetic stirrer at 500rpm for 12hrs. Finally, the solution is washed with DI water and black powder (r-GO(C)) is obtained.

For preparing a thin film of r-GO, 15mL r-GO is dissolved in 1mL of NMP (N-methyl-2-pyrrolidone). The resulting solution is sonicated for 5hrs. Thin films of r-GO are obtained by drop-casting 30µl of the solution onto 1cm X 1cm quartz, undoped silicon, and FTO substrates.

3.1.3 Preparation of Boron doped Reduced Graphene Oxide

To synthesize boron doped r-GO samples, boric acid is used as boron source, two types of Boron doped Reduced Graphene Oxides were obtained:

1. The prepared Graphene Oxide (750mg) was doped with boron by mixing 1.5g of Boric Acid (H_3BO_3) and 20ml of DI water. The solution was then sonicated for

30minutes. Further, the solution is placed in autoclave and kept in a muffle furnace at 500°C for 12 hours. The sample was cooled to room temperature. r-BGO powder was collected and it was dried in an oven at 60°C for overnight.

2. The prepared Reduced Graphene Oxide (2.1mg) and 6.3mg Boric Acid (H_3BO_3) were mixed with 30mL propanol for boron doping. This solution was sonicated for half an hour and then placed into autoclave and kept in a muffle furnace at 150°C for 10 hours. The sample was cool down to the room temperature and B-rGO black powder was obtained.

3.2 Results and Discussion

3.2.1 Comparative study of chemically and thermally reduced graphene oxide based on their specific surface area, structural and electrical properties

To confirm the synthesis of Graphene Oxide and it's further reduction to reduced Graphene Oxide, XRD studies were done. It has been observed that due to presence of oxygen functionalities, the peak appeared at 2θ=10.61° for GO where the *d* spacing is 0.832nm due to intercalation of oxide functional group such as epoxy, hydroxyl, carbonyl, and carboxyl groups at the carbon basal plane. Further, when Graphene Oxide is reduced (r-GO), functional groups are removed and the interlayer spacing is decreased in r-GO for both thermally and chemically reduced samples. This indicates that the π-conjugated structure of graphene has been restored considerably at the produced r-GO. A peak shift is observed for r-GO at 2θ =24.5° in case of r-GO(C) and at 25.42^0 in case of r-GO(T). In case of r-GO(T), the peak is more intense which may imply that crystal plane (002) are more periodically arranged in r-GO(T) compared to r-GO(C). In addition, the d-spacing of r-GO was reduced from 0.832nm for GO to 0.36nm for r-GO(C) and 0.38 for r-GO(T) which proved that oxygen-containing functional groups were removed efficiently in both the cases. Another less intense

peak could be seen at 2θ=42.60° for r-GO samples with (001) orientation which is attributed to the turbostratic band of disordered carbon materials.

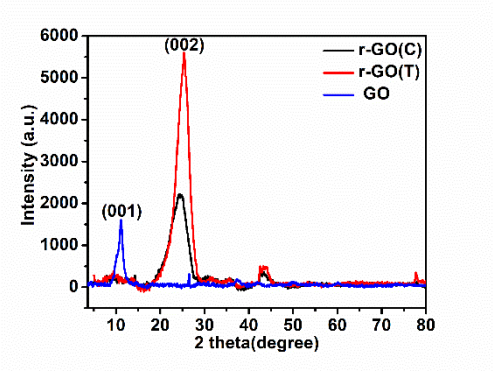

Fig.3.1: XRD Spectra of GO, r-GO (C) and r-GO (T)

Table 3.1: XRD data analysis for d-spacing(d) for GO, r-GO (C) and r-GO (T)

Sample Name	2-theta (°)	d-spacing (nm)
Graphene Oxide	10.61	0.832
r-GO(C)	24.50	0.363
r-GO(T)	25.42	0.380

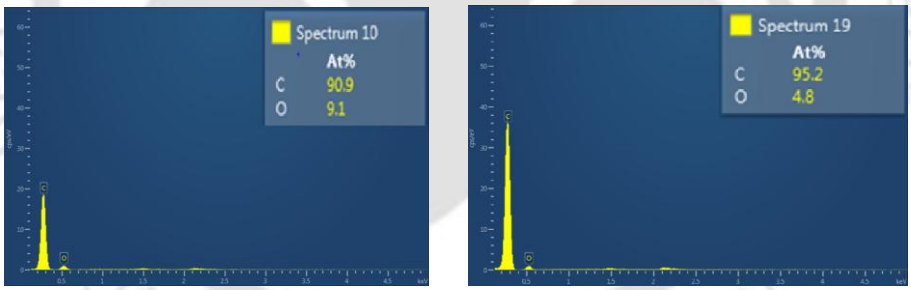

a) b)

Fig.3.2: EDX analysis of a) r-GO(C) and b) r-GO(T)

EDX analysis was carried out to find the ratio of atomic concentration of Carbon and Oxygen atoms for r-GO films. The ratio is 90:10 in case of r-GO(C) and 95:5 in case of r-GO(T). Less oxygen content in case of r-GO(T), indicates that thermal reduction is more efficient than chemical reduction to obtain r-GO samples.

The surface areas and pore size distribution of all materials were determined by the BET method from N_2 isotherm using a Quantachrome Autosorb Automated instrument.The estimated values of specific Surface area, average pore size and total pore volume are listed in the table 3.2.

Table 3.2: Specific Surface area, Average pore diameter and Pore Volume of r-GO(C), and b) r-GO(T)

Sample Name	Specific Surface Area (m^2/g)	Average pore diameter (nm)	Pore Volume (cc/g)
r-GO(C)	17.35	1.716	0.074
r-GO(T)	74.78	1.806	0.338

According to the average pore size, both the samples are microporus because their pore sizes are between 1 to 2nm. Also, we observe that in case of r-GO(C), the BET surface area is17.35m^2/g and 74.78m^2/g in case of r-GO(T). Greater BET surface area indicates that the adsorption capacity is expected to increase with the surface area.

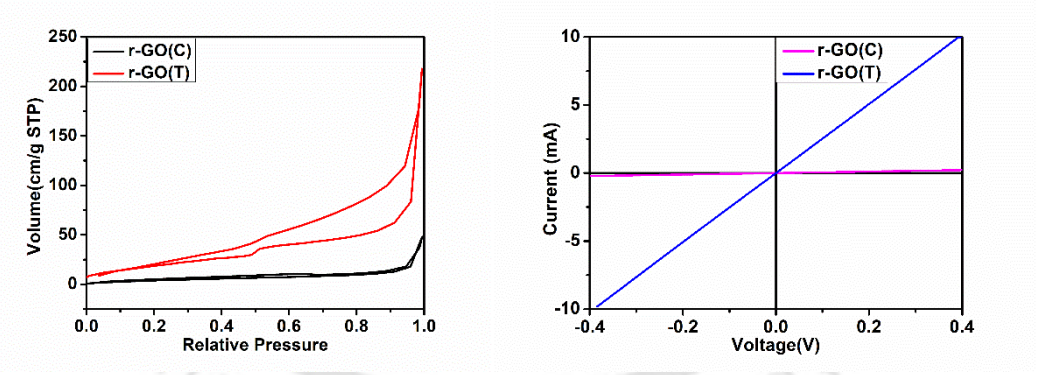

Fig. 3.3: (a) Absorption isotherm of r-GO(C), and r-GO(T) (b) I-V characteristics of r-GO(C), and r-GO(T)

For I-V measurement, thin film of GO and r-GO samples were prepared by drop-casting method. The thickness of the drop-casted GO film used for both chemical and thermal reduction was approximately 300nm, measured using stylus profilometry. Electrodes were made from silver paint. From fig. 3.3, we can observe that the conductivity of r-GO(C)) is 0.049S/cm and r-GO(T) is 2.28S/cm. The I-V characteristics of the thermally and chemically

reduced GO films indicate the presence of impurities and incomplete reduction in the chemically reduced samples. The chemically reduced r-GO exhibits a more resistive and non-linear I-V response, suggesting that residual oxygen-containing functional groups and structural defects continue to hinder charge transport. These unreduced groups act as trapping sites and disrupt the sp^2 network, preventing full restoration of electrical conductivity.[12-14] In contrast, the thermally reduced GO shows a comparatively more linear and conductive I-V behavior, confirming a higher degree of deoxygenation and better graphitic reconstruction.[13-15] The difference in electrical characteristics corroborates that the chemical reduction route did not achieve complete removal of oxygen functionalities, leading to heterogeneous film quality and limited electronic performance. For all the synthesis and analysis process further, thermally reduced graphene oxide is used.

3.2.2 Thermal Kinetics study of Graphite, Graphene Oxide and Reduced Graphene Oxide

Thermal kinetics or thermal stabilities studies are carried out for Graphite, Graphene Oxide, and Reduced Graphene Oxide by Thermogravimetric Analysis (TGA). To measure the mass change of samples as a function of temperature and time, the samples were subjected to thermal decomposition from room temperature to 900°C under inert atmosphere with the heating rate of 10°C/min. With this technique, we can measure the decomposition, sublimation, reduction, desorption, adsorption and vaporization in terms of mass change.

We can see the TGA graphs and their corresponding first derivative thermogravimetry DTG graphs with their respective T_{max} values are presented in fig. 3.4 (a) and (b). DTG graphs generated from TGA curves demonstrated three distinguished DTG peaks corresponding to three mass loss events in GO whereas for r-GO and Graphite only one single DTG peak that can be related to only a single mass loss step occurred during the thermal degradation for both Graphite and r-GO.

The key mass loss events of GO can be explained based on various decomposition temperatures: mass loss at <100°C is due to water elimination, 100-360°C due to the removal of oxygen functional groups and 360-900°C can be linked to the oxidative pyrolysis of carbon framework. The only DTG peak found graphite and reduced graphene oxide samples can be ascribed to the combustion of carbon. As depicted in the DTG, their carbon combustion temperature was distinctly marked in terms of the temperature of maximum mass change rate (T_{max}) with GO at (T_{max} = 515-660°C), r-GO at (T_{max} = 456-606°C) and graphite at (T_{max} = 675-801).

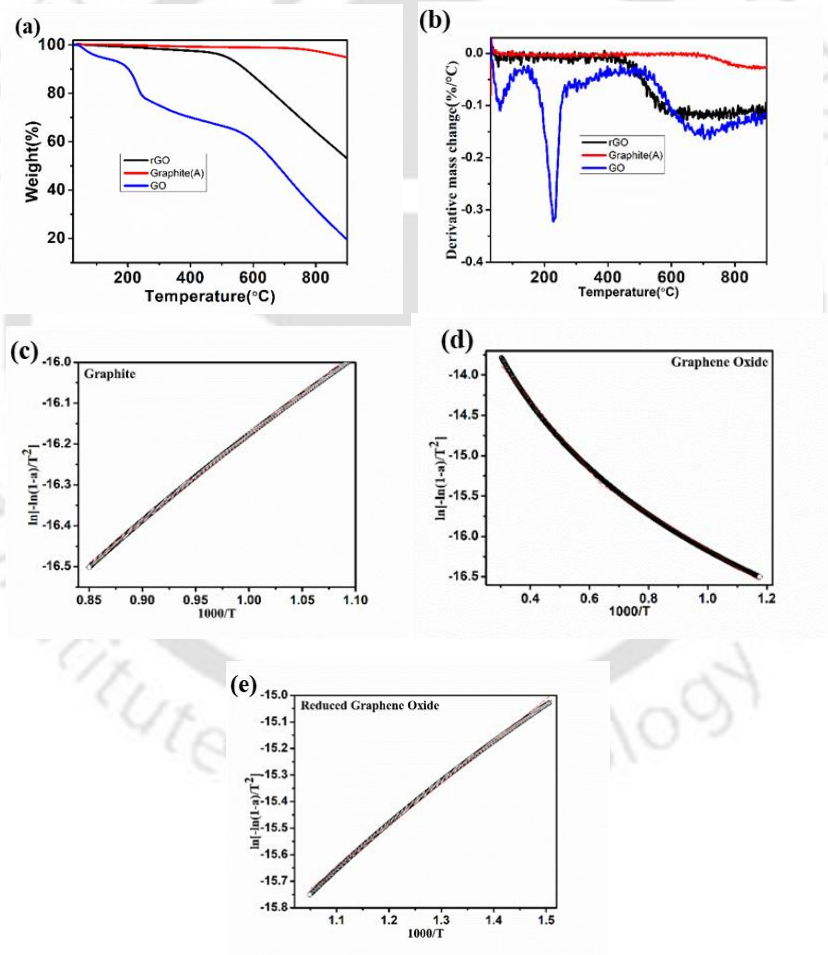

Fig. 3.4: (a)TGA curve of Graphite, GO, r-GO (b)DTA curve of Graphite, GO, rGO. Coats Redfern plot of thermal decomposition of (c)Graphite (d) Graphene Oxide (e) reduced Graphene Oxide

The distinguished T_{max} can be attributed to the maximum of the external heat energy required to overcome the strong bonding within their carbon lattice structure. Graphite has higher T_{max} because it needs larger amount of heat energy to break down the sp^2 hybridized carbon

atoms ordered by covalent bonds in a hexagonal carbon framework. Graphite, the most thermodynamically stable carbon materials studied in this work, demands even more heat energy due to its strongest 3D carbon network, consisting of a large number of graphene stacked layers held by additional van der Waals forces. From these studies, it is obvious that T_{max} can be regarded as a key parameter that can be used for their identification and specifically for detection of presence of GO and graphite impurities in graphene materials.

There are different models used to study the kinetic parameters, such as Ozawa method, Kissinger method, Coats-Redfern model, Freeman-Carrol method etc. Among these, Coats-Redfern model is simple and require only one heating rate whereas others require measurements for at least 3 different heating rates. For our study, Coats-Redfern model is used to calculate thermodynamic parameters like activation energy, Arrhenius parameter, entropy change, enthalpy change and Gibbs free energy.

In thermal decomposition, the rate of disappearance of the original substance is described by the reaction kinetics equation,

$$d\alpha/dt = Ae^{-(E/RT)}(1-\alpha)^{n} \quad (3.1)$$

where α is the fraction of the original substance decomposed at time t, n is the order reaction, A is the preexponential factor and E is the activation energy of the reaction. In non-isothermal mode, for a linear heating rate β= dT/dt, the following Coats-Redfern equation can be obtained by integrating and rearranging the above reaction kinetics equation.

$$ln[g(\alpha)/T^2] = ln[(AR/\beta E)(1-2RT/E)] - E/RT \quad (3.2)$$

where g(α) is the kinetic model function.

The slope of the plot of $ln[g(\alpha)/T^2]$ against 1/T is a straight line, from which the activation energy (E) is calculated. The pre-exponential factor, Arrhenius parameter (A) is also

calculated from the intercept of curve on y-axis which is equal to ln (AR/βE). The kinetic parameter, entropy of activation (ΔS) is calculated using the following equation.

$$\Delta S(J/Kmol) = 2.303R(\log (Ah/k_B T_P)) \quad (3.3)$$

where h is the Planck's constants and T_P is the peak temperature of DTG.

Table 3.3: Thermodynamic parameters in thermal decomposition of Graphite, GO, r-GO

Sample	Decomposition	Activation Energy, Ea (KJ/mol)	Arrhenius Parameter (s^{-1})	DTG Peak temperature T_P (°C)	Entropy change (KJ/mol)
Graphite	Step 1	17.11	2.95×10^7	804	-112.59
Graphene Oxide	Step 1	36.19	2.09×10^5	226.96	-147.38
	Step 2	18.52	4.16×10^5	696.07	-147.16
Reduced Graphene Oxide	Step 1	13.21	9.4×10^6	595.76	-120.28

From the table 3.3, it can be seen that the activation energy is more is case of Graphene Oxide compared to Graphite and reduced Graphene Oxide. This is because large amount of energy is required for removal of oxygen containing functional in GO compared to r-GO and Graphite. For similar reasons, we can see the increased value of entropy change for Graphene Oxide.

3.2.3 Facile synthesis of Boron doped reduced Graphene Oxide as electrode material for Supercapacitor Applications

To understand the impact of boron doping in GO and thermally reduced rGO on structural and electrochemical properties and its further application in supercapacitors as electrodes, boron doped reduced graphene oxides are prepared by two different ways i.e. doping graphene oxide with boron and then reducing it (r-BGO) and doping thermally reduced graphene oxide with boron (B-rGO). X-Ray Diffraction (XRD) pattern for the Graphite, Graphene Oxide (GO), Reduced Graphene Oxide (r-GO) and boron doped reduced graphene oxide using Cu Kα radiation (λ=1.54Å) are shown in the Figure 3.5 (a). r-BGO gives a sharp

peak at 2θ=27.76° corresponding to the (002) plane and graphitic interlayer spacing of 0.32 nm.

B-rGO gives a broad peak at 2θ=25.37° corresponding to the (002) plane and graphitic interlayer spacing of 0.351nm. The small difference in 2θ values for boron doped samples from r-GO suggests that boron doping is successful into the hexagonal crystalline structure. In r-BGO, reduction and doping occur simultaneously so interlayer spacing is reduced and become lesser than Graphite. Also, the sample is highly crystalline in nature. In B-rGO (Boron-doped in Reduced Graphene Oxide), it seems doping did not influence the interlayer spacing since reduction was done before doping. It is concluded that most of the boron doping occurred on the sp^2 carbon plane.

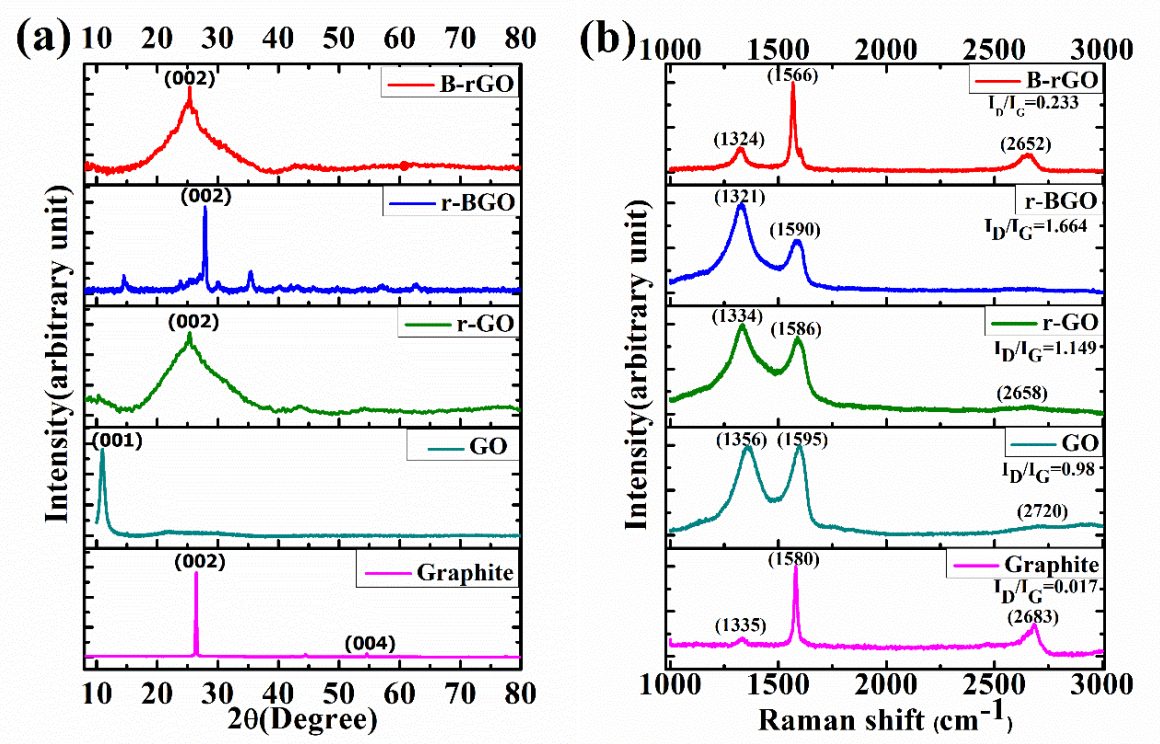

Fig. 3.5: (a) XRD Pattern of Graphite, GO, r-GO, r-BGO, B-rGO (b) Raman Spectra of Graphite, GO, r-GO, r-BGO, B-rGO

Table 3.4: XRD data analysis for d-spacing(d) for Graphite, GO, r-GO, r-BGO and B-rGO

Sample	Graphite	GO	r-GO	r-BGO	B-rGO
d(nm)	0.336	0.810	0.350	0.320	0.351

From Raman spectra (fig. 3.5 (b)), graphitic nature of the precursor powder was observed by a sharp band occurring near 1580cm^{-1} from sp^2 carbon atoms. In case of GO, sharp bands appeared at 1356, 1595 and 2720 cm^{-1}. In GO, the prominent Raman signal at 1356 cm^{-1} is attributed to the sp^3 defects in the sp^2 lattice, which is designated by the D-band and is related to the defects in graphene structure. Another peak at ~2720 cm^{-1} denoted by 2D-band is attributed to the development of graphene structure. Subsequent reduction by thermal exfoliation resulted in Raman bands appearing at 1334 cm^{-1} (D-band), 1586 cm^{-1} (G-band) and 2658cm^{-1} (2D-band), respectively. The specific Raman bands and their intensity ratios may provide useful information about the structure of graphene such as D/G band intensity ratio, which represents defects (edges, vacancies, ripples, etc.) while 2D/G represents the number of layers in graphene.[16-19]

Table 3.5: I_D /I_G ratio and Cluster size for Graphite, GO, r-GO, r-BGO and B-r-GO

Sample	I_D /I_G	Cluster size
Graphite	0.017	2266 nm
GO	0.983	39.19 nm
r-GO	1.149	33.53 nm
r-BGO	1.664	23.15 nm
B-rGO	0.233	165.37nm

In r-BGO, the intensity of defect peak is increased (table 3.5). When Boric acid is added with GO then boron atoms react with the functional groups which are present in GO and carbon plane both.[20-22] So, the defects are increased. Therefore, the I_D/I_G is increased in r-BGO compares to GO. The intensity of defect peak is decreased in B-rGO which implies that the doping mainly, occurred in the plane existing in r-GO structure. The defects in r-GO plane is occupied by boron atoms, which results in minimal structural defects as observed in Raman. Therefore, the I_D/I_G is decreased in B-rGO.

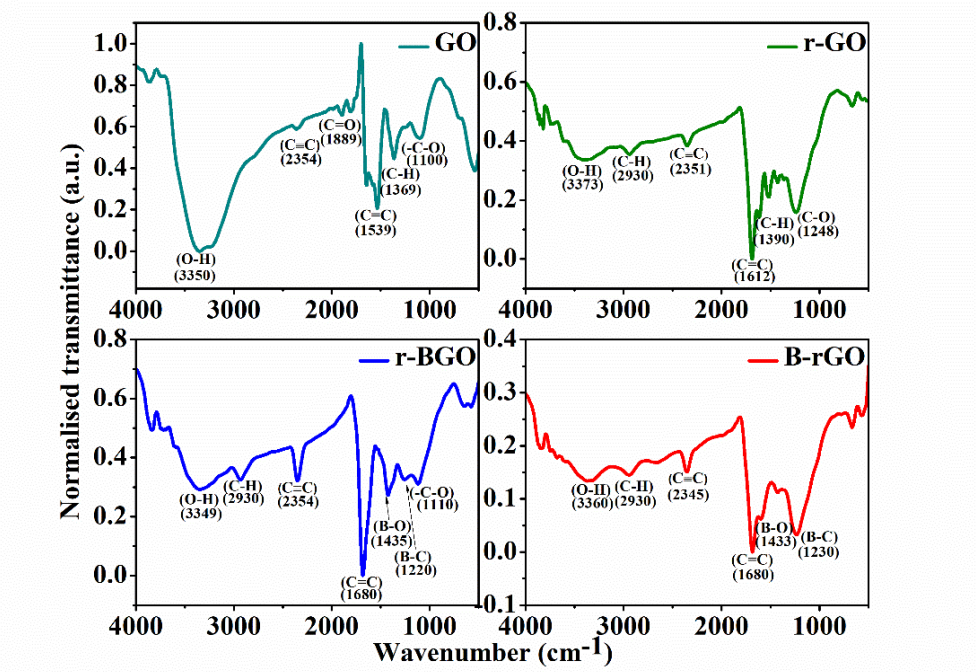

Fig 3.6: FTIR Spectra of GO, r-GO, r-BGO and B-rGO

The FTIR spectra in fig. 3.6 is also in well agreement with XRD and Raman spectra. As shown in fig. 3.6, the major peaks are observed for GO at 3350, 2354, 1889, 1539, 1369 and 1100cm^{-1} corresponding to hydroxyl (-OH), alkaline (C≡C), carbonyl (C=O), aromatic (C=C), alkyl (C-H), and (-C-O) functional groups respectively. This shows successful oxidation of graphene oxide from graphite.

Table 3.6: The comparative ratio of intensities corresponds to (C=C) and (O-H) bonds

Bonds	$I_{r\text{-}GO}/I_{GO}$	$I_{r\text{-}BGO}/I_{GO}$	$I_{B\text{-}rGO}/I_{GO}$	$I_{r\text{-}BGO}/I_{r\text{-}GO}$	$I_{B\text{-}rGO}/I_{r\text{-}GO}$
C=C	0.9623	0.8454	0.8948	0.8785	0.9298
O-H	0.2739	0.3517	0.3516	1.2839	1.2837

The reduction from graphene oxide to reduced graphene oxide is shown by loss in the prominence of oxygen containing functional groups in r-GO. Further the presence of boron containing functional groups i.e., (B-O), and (B-C) peaks in r-BGO as well as B-rGO confirm the successful boron doping in both the samples.

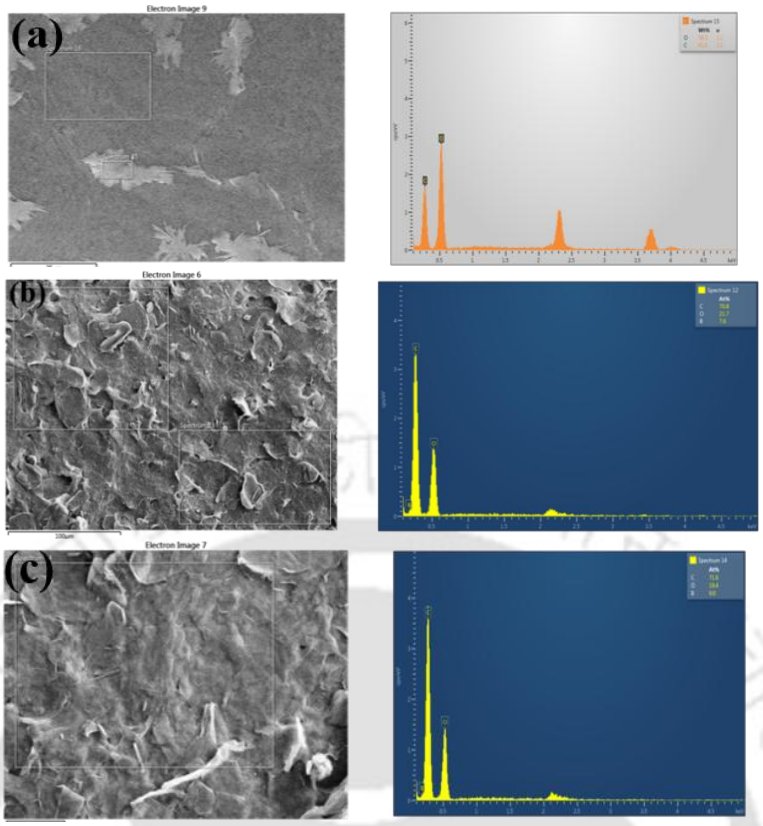

Fig 3.7: FESEM image and EDX of (a) Graphene Oxide (GO), (b) r-BGO and (c) B-rGO

From table 3.6, it is shown that for C=C and O-H bonds, $I_{r\text{-}BGO}/I_{GO}$ is less than $I_{B\text{-}rGO}/I_{GO}$. So, it is easier to functionalize GO than r-GO as bonds in r-GO are more stable. These ratios (r-BGO and B-rGO) are also in agreement with EDX results discussed further. The elemental composition of carbon, oxygen and boron in GO, r-GO, r-BGO and B-rGO are shown in fig. 3.7. The at% of Carbon and Oxygen in Graphene Oxide are 41.5% and 58.5%. This confirms the presence of oxygen containing groups and hence the formation of Graphene Oxide. We have performed EDX analysis at different places in the sample and observed that at an average, we have successfully been able to dope r-BGO by ~7.6% and B-rGO by ~1%. The doping of Boron in r-BGO is more effective than B-rGO. GO has functional groups so, when boric acid reacted with GO, boron was successfully doped. But in r-GO functional groups were already removed so when boric acid is added with r-GO, boron doping was less compared to r-BGO.

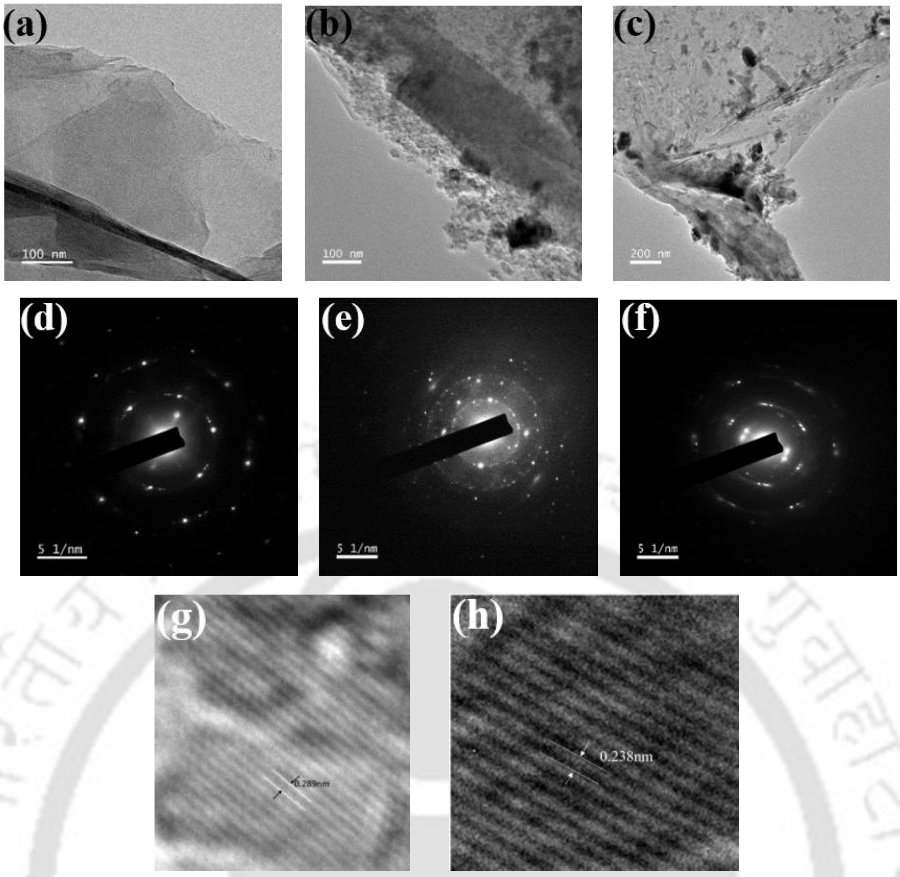

Fig 3.8: FETEM image of (a) GO, (b) r-BGO (c) B-rGO, SAED pattern of (d) GO (e) r-BGO, (f) B-rGO and HRTEM image of (g) GO and (h) B-rGO

From FETEM in fig. 3.8, we can see some attachments at the surface of B-rGO as compared to GO. This could be due to presence of boron atoms at the surface. The SAED image also shows that GO is crystalline in nature whereas B-rGO is polycrystalline. This also confirms the distortion in the structure of GO due to intercalation of boron atoms in the middle. From the HRTEM analysis, we have observed an increase in the interlayer spacing from 0.23nm in GO to 0.286nm in B-rGO. This could result in the increase of surface area of B-rGO implying increase in the charge storage capacity.

The electrochemical behavior of the samples was evaluated using 3 electrode system with Ag/AgCl as reference electrode, Pt as counter electrode and 3M H_2SO_4 as electrolyte solution. Table 3.7 compares our findings with those published in the literature. Our findings are consistent with previous reports for all the samples.

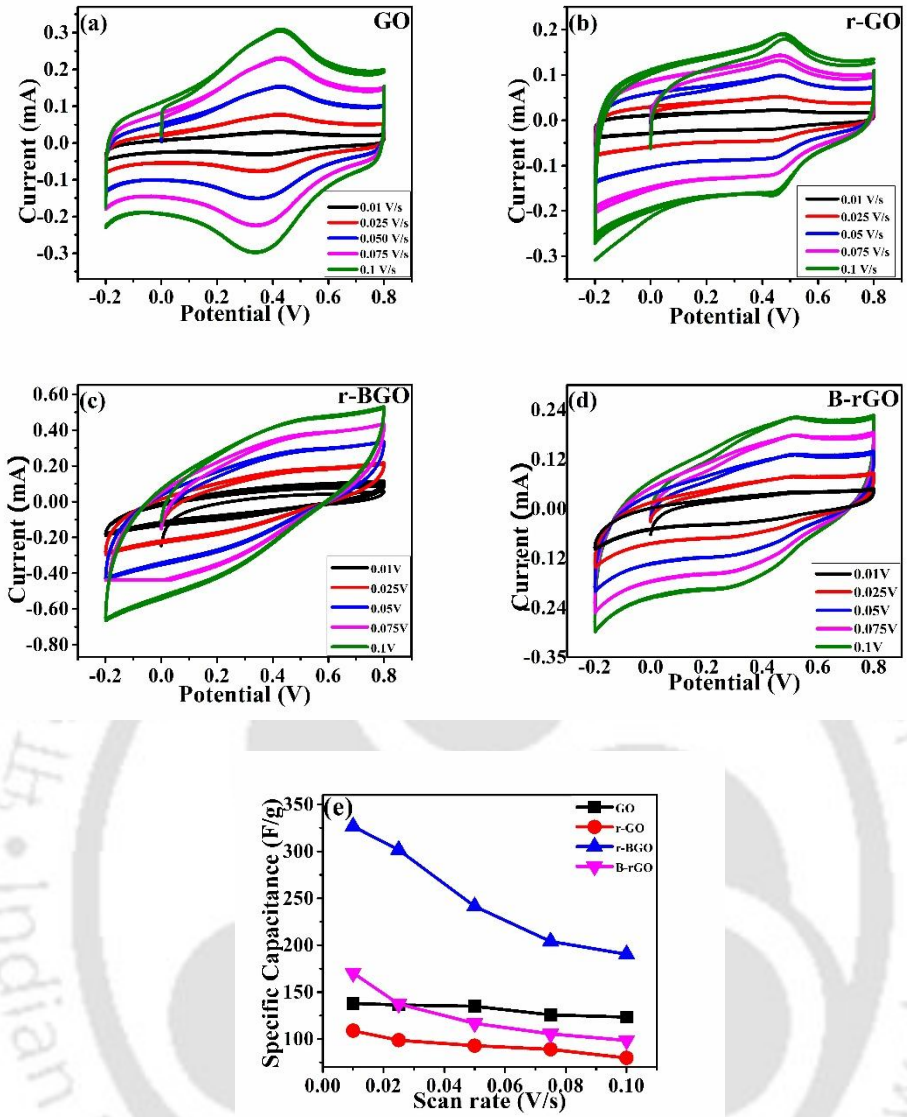

Fig 3.9: CV Curve of (a) GO, (b) r-GO, (c) r-BGO, and (d) B-rGO at different scan rates and (e) Specific Capacitance Vs Scan rates for GO, r-GO, r-BGO, B-rGO

As shown in fig 3.9, the Specific capacitances of GO, r-GO, r-BGO and B-rGO were investigated with scan rates from 0.01V/s to 0.1V/s. We observed that the specific capacitance has decreased for all the samples when scan rate is increased from 0.01V/s to 0.1V/s. The dependency of specific capacitance on scan rate is possibly due to ion diffusion in the carbon material. The ions can penetrate higher at lower scan rates as they have sufficient time to enter and exit from the pores whereas at high scan rates, only surface interaction takes place.

Table 3.7: Specific capacitance comparison of doped Graphene oxides reported in the Literatures

Sample		Specific Capacitance (F/g)	Reference
Graphene Oxide	GO	**137.88**	**Our work**
	GO	16.9 (without plasma treatment) 85.6 (after plasma treatment)	[23]
Reduced graphene oxide	r-GO	**108.85**	**Our work**
	r-GO	148	[22]
	r-GO	135	[24]
	T-GNS	53	[11]
Boron doping in reduced graphene oxide	B-rGO	**170.46**	**Our work**
	HB-GNS	113	[11]
Boron doping in graphene oxide	r-BGO	**326.56**	**Our work**
	BT-rGO	448	[24]
	B-rGO (boron doping of GO)	173.7 (without plasma treatment) 345 (after plasma treatment)	[23]
	B-rGO (boron doping of GO)	240	[22]
	B-rGO (boron doping of GO)	237 (without plasma treatment) 446.24 (after plasma treatment)	[25]

Fig. 3.9 (e) shows the variation in specific capacitance value at higher scan rates is observed for r-BGO samples. The specific capacitance for boron doped samples is higher than GO and r-GO at each corresponding scan rates from 0.1V/s to 0.01V/s. The CV curves show rectangular shapes, indicating the typical feature of an electrochemical double-layer capacitor (EDLC). The specific capacitance values for r-BGO and B-rGO are 326.56 ± 3.1F/g and 170.46F/g respectively, which are 2.36 and 1.24 times higher than that of GO (fig 3.9 (e)).

3.3 Conclusion:

Here, we prepared Graphene Oxide by Modified Hummers method and then reduced it to r-GO by two different ways. One by thermal annealing at high temperature secondly by using hydrazine hydrate as chemical reducing agent. We have compared the properties of both the samples. We found that the specific surface area in r-GO(C) is 17.35m^2/g, pore diameter is

1.716nm and total pore volume is 0.074cm^3/g. In r-GO(T), the specific surface area is 74.78m^2/g, pore diameter is 1.806nm and total pore volume is 0.338cm^3/g. Electrical properties of both the samples shows that the electrical conductivity of r-GO(C) is 0.049S/cm and r-GO(T) is 2.28S/cm. This shows that although reduction takes place in both the process, the quality is better in case of thermal reduction. However, the drawback of thermal reduction is the requirement of high temperature. Further bulk synthesis of boron-doped reduced graphene oxide (B-rGO & r-BGO) as an electrode material for supercapacitors is reported here by using Boric acid (H_3BO_3) as boron source. The structural properties of B-rGO and r-BGO have been studied by XRD, Raman, EDAX and FETEM analysis. The r-BGO samples are highly crystalline in nature whereas B-rGO is amorphous. The intercalation of boron atom in the lattice is also confirmed by increase in inter-layer spacing from 0.23nm to 0.28nm from HRTEM analysis. Presence of dip corresponding to B-C and B-O bond in FTIR transmission spectra further confirms efficient boron doping for both B-rGO and r-BGO samples. We have reported an increased capacitance of 326.56 ± 3.1 F/g for r-BGO and 170.46± 2 F/g for B-rGO compared to GO (137.88 ± 1.8 F/g) and r-GO (108.85 ± 1.6 F/g). This signifies that boron doping in Graphene Oxide before reduction (r-BGO) is efficient compared to reduced graphene oxide (B-rGO). These values are comparable to those reported so far. The doping is also confirmed by XRD, Raman, FTIR and EDX Analysis. This nitrogen doping has also increased the conductivity as compared to Graphene Oxide.

3.4 References:

1. Miro, P., M. Audiffred, and T. Heine, *An atlas of two-dimensional materials.* Chem Soc Rev, 2014. **43**(18): p. 6537-6554.
2. Yokwana, K., B. Ntsendwana, E.N. Nxumalo, and S.D. Mhlanga, *Recent advances in nitrogen-doped graphene oxide nanomaterials: Synthesis and applications in energy storage, sensor electrochemical applications and water treatment.* Journal of Materials Research, 2023. **38**(13): p. 3239-3263.
3. Im, M.J., J.I. Kim, S.K. Hyeong, B.J. Moon, and S. Bae, *From Pristine to Heteroatom-Doped Graphene Quantum Dots: An Essential Review and Prospects for Future Research.* Small, 2023. **19**(47): p. 2304497.
4. Hossain, M.Z., J.E. Johns, K.H. Bevan, H.J. Karmel, Y.T. Liang, S. Yoshimoto, K. Mukai, T. Koitaya, J. Yoshinobu, M. Kawai, A.M. Lear, L.L. Kesmodel, S.L. Tait, and M.C. Hersam,

Chemically homogeneous and thermally reversible oxidation of epitaxial graphene. Nat Chem, 2012. **4**(4): p. 305-9.
5. Yang, G., L. Li, W.B. Lee, and M.C. Ng, *Structure of graphene and its disorders: a review.* Sci Technol Adv Mater, 2018. **19**(1): p. 613-648.
6. Dong, F., Y. Cai, C. Liu, J. Liu, and J. Qiao, *Heteroatom (B, N and P) doped porous graphene foams for efficient oxygen reduction reaction electrocatalysis.* International Journal of Hydrogen Energy, 2018. **43**(28): p. 12661-12670.
7. Rosli, N.H.A., K.S. Lau, T. Winie, S.X. Chin, and C.H. Chia, *Synergistic effect of sulfur-doped reduced graphene oxide created via microwave-assisted synthesis for supercapacitor applications.* Diamond and Related Materials, 2021. **120**: p. 108696.
8. Ghotia, S., T. Rimza, S. Singh, N. Dwivedi, A.K. Srivastava, and P. Kumar, *Hetero-atom doped graphene for marvellous hydrogen storage: unveiling recent advances and future pathways.* Journal of Materials Chemistry A, 2024. **12**: p. 12325-12357.
9. Kaushal, S., M. Kaur, N. Kaur, V. Kumari, and P.P. Singh, *Heteroatom-doped graphene as sensing materials: a mini review.* RSC Adv, 2020. **10**(48): p. 28608-28629.
10. Wang, X., G. Sun, P. Routh, D.H. Kim, W. Huang, and P. Chen, *Heteroatom-doped graphene materials: syntheses, properties and applications.* Chem Soc Rev, 2014. **43**(20): p. 7067-98.
11. Thirumal, V., A. Pandurangan, R. Jayavel, and R. Ilangovan, *Synthesis and characterization of boron doped graphene nanosheets for supercapacitor applications.* Synthetic Metals, 2016. **220**: p. 524-532.
12. Ahmad, F., M. Zahid, H. Jamil, M.A. Khan, S. Atiq, M. Bibi, K. Shahbaz, M. Adnan, M. Danish, F. Rasheed, H. Tahseen, M.J. Shabbir, M. Bilal, and A. Samreen, *Advances in graphene-based electrode materials for high-performance supercapacitors: A review.* Journal of Energy Storage, 2023. **72**.
13. Minitha, C.R., V.S. Anithaa, V. Subramaniam, and R.T. Rajendra Kumar, *Impact of Oxygen Functional Groups on Reduced Graphene Oxide-Based Sensors for Ammonia and Toluene Detection at Room Temperature.* ACS Omega, 2018. **3**(4): p. 4105-4112.
14. Woo, Y.S., *Transparent Conductive Electrodes Based on Graphene-Related Materials.* Micromachines (Basel), 2018. **10**(1).
15. Bagade, S.S., S. Patel, M.M. Malik, and P.K. Patel, *Recent Advancements in Applications of Graphene to Attain Next-Level Solar Cells.* C, 2023. **9**(3).
16. Wang, Y., K. Zhang, R. Wang, C. Zhang, F. Kong, and T. Shao, *Plasma jet printing for preparation of N-doped graphene electrode.* Journal of Materials Science: Materials in Electronics, 2019. **30**(9): p. 8944-8954.
17. Miao, Y., Y. Ma, and Q. Wang, *Plasma-Assisted Simultaneous Reduction and Nitrogen/Sulfur Codoping of Graphene Oxide for High-Performance Supercapacitors.* ACS Sustainable Chemistry & Engineering, 2019. **7**(8): p. 7597-7608.
18. Seo, D.H., Z.J. Han, S. Kumar, and K. Ostrikov, *Structure-Controlled, Vertical Graphene-Based, Binder-Free Electrodes from Plasma-Reformed Butter Enhance Supercapacitor Performance.* Advanced Energy Materials, 2013. **3**(10): p. 1316-1323.
19. Li, Z., S. Gadipelli, Y. Yang, G. He, J. Guo, J. Li, Y. Lu, C.A. Howard, D.J.L. Brett, I.P. Parkin, F. Li, and Z. Guo, *Exceptional supercapacitor performance from optimized oxidation of graphene-oxide.* Energy Storage Materials, 2019. **17**: p. 12-21.
20. Ngidi, N.P.D., M.A. Ollengo, and V.O. Nyamori, *Tuning the properties of boron-doped reduced graphene oxide by altering the boron content.* New Journal of Chemistry, 2020. **44**(39): p. 16864-16876.
21. Riyanto, I. Sahroni, K. Bindumadhavan, P.Y. Chang, and R.A. Doong, *Boron Doped Graphene Quantum Structure and MoS(2) Nanohybrid as Anode Materials for Highly Reversible Lithium Storage.* Front Chem, 2019. **7**: p. 116.
22. Zhu, T., S. Li, B. Ren, L. Zhang, L. Dong, and L. Tan, *Plasma-induced synthesis of boron and nitrogen co-doped reduced graphene oxide for super-capacitors.* Journal of Materials Science, 2019. **54**(13): p. 9632-9642.
23. Wu, S., C. Zhang, X. Cui, S. Zhang, Q. Yang, and T. Shao, *Facile synthesis of nitrogen-doped and boron-doped reduced graphene oxide using radio-frequency plasma for supercapacitors.* Journal of Physics D: Applied Physics, 2021. **54**(26): p. 265501.

24. Yeom, D.Y., W. Jeon, N.D. Tu, S.Y. Yeo, S.S. Lee, B.J. Sung, H. Chang, J.A. Lim, and H. Kim, *High-concentration boron doping of graphene nanoplatelets by simple thermal annealing and their supercapacitive properties.* Sci Rep, 2015. **5**: p. 9817.
25. Li, S., Z. Wang, H. Jiang, L. Zhang, J. Ren, M. Zheng, L. Dong, and L. Sun, *Plasma-induced highly efficient synthesis of boron doped reduced graphene oxide for supercapacitors.* Chem Commun (Camb), 2016. **52**(73): p. 10988-10991.

Chapter 4

Growth of multi-layer Graphene by HWCVD on Nickel substrate

In this chapter, we present a comprehensive investigation into the controlled synthesis and transfer of high-quality graphene films via hot-wire chemical vapor deposition (HWCVD) on nickel substrates. Here, methane (CH_4) and hydrogen (H_2) precursors are activated at a heated filament to generate reactive carbon species that dissolve into nickel at elevated substrate temperatures. By systematically varying the CH_4/H_2 gas flow rates, total deposition time, and post-growth annealing temperature, we achieve precise control over both the uniformity and thickness of graphene, producing films that range from bilayer to 10 layers. We then detail a robust wet-chemical etching protocol employing a PMMA support coating and $FeCl_3$-based nickel dissolution for the clean transfer of as-grown graphene onto silicon wafers. Finally, we employ Raman spectroscopy and tapping-mode atomic force microscopy (AFM) to quantify

surface morphology and number of layers of graphene. Correlating our measurements with the deposition conditions reveals how process parameters define graphene's structure and performance, supporting the scalable production of custom films for silicon devices.

4.1. Experimental Details

4.1.1. Deposition Parameters

Graphene films are deposited on Ni foil (125 μm thick, 99.9% purity) by HWCVD method using CH_4, and H_2 precursor gases. Films are deposited by varying the deposition time, CH_4/H_2 gas flow rates, and annealing temperature after the deposition. Deposition parameters for the growth of graphene films are divided into three series a) influence of deposition time at deposition and annealing temperature of 700°C, b) influence of CH_4/H_2 ratio deposition and annealing temperature of 700°C, and c) Influence of annealing temperature variation from 700 °C to 780°C for films deposited on a fixed deposition temperature of 700°C. Deposition parameters such as filament temperature and filament to substrate distance were kept at 2050±50 °C and 1.5 cm respectively for all the films. Filament temperature was measured using pyrometer by focusing at the center of tungsten filament.

4.1.2. Transfer process of Graphene Films from Nickel foil to Silicon Substrates

Graphene films, initially deposited on nickel (Ni) foil, are transferred onto silicon (Si) substrates through a chemical etching process, following the method outlined in previous literature[1-5]. This transfer process consisted of several critical steps to ensure the successful transfer of graphene films onto the desired substrates. The process began with the preparation of a poly(methyl methacrylate) (PMMA) solution, where PMMA was dissolved in tetrahydrofuran (THF) solvent at a concentration of 5 mg/ml. A small drop of this solution was spin coated to the surface of the graphene films, forming a protective layer that would aid in the subsequent handling and transfer of the delicate graphene structure. This PMMA coating

served as a mechanical support to maintain the integrity of the graphene film during the etching and transfer process.

Following the application of PMMA, the nickel substrate was selectively etched away using a 1M ferric chloride ($FeCl_3$) solution. The etching process was gradual, allowing complete dissolution of the Ni foil over approximately 12 hours. As the etching progressed, the graphene film, supported by the PMMA layer, began to separate from the Ni substrate and floated freely within the $FeCl_3$ solution. The floating graphene films were then carefully extracted and transferred onto Silicon substrates

Once the graphene films were successfully placed onto the target substrates, the next step involved the removal of the PMMA support layer. This was achieved by immersing the samples in acetone, which effectively dissolved the PMMA, leaving behind graphene film. To eliminate any residual contaminants and ensure a pristine surface, the graphene-coated substrates were subsequently rinsed thoroughly with deionized water. This final washing step helped remove impurities from the transfer process. The overall transfer process of graphene films onto silicon substrates is illustrated in Figure 4.1.

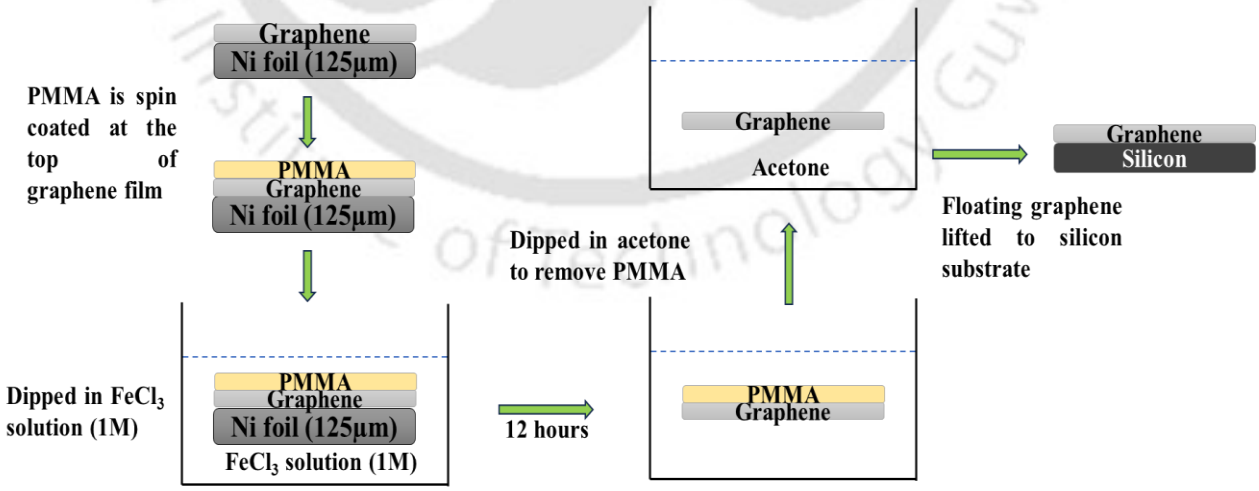

Fig. 4.1: Schematic of transfer process of Graphene onto silicon substrates

In metal-catalyzed CVD systems such as Cu and Ni, graphene growth is primarily governed by the balance between precursor activation, surface reactions, nucleation density, and the

evolution of defects during and after deposition. For device-oriented applications, it is therefore essential to minimise both intrinsic structural defects and extrinsic defects arising from gas-phase reactions or handling steps during processing. [6] For Ni-based growth, the nucleation density plays a decisive role in determining grain size and the likelihood of multilayer formation, while parameters such as methane partial pressure, growth temperature, and hydrogen chemistry provide practical control over surface coverage and suppression of unwanted carbon species. [7] Consequently, the final layer number, film continuity, and transfer compatibility are governed by the selected process window, establishing a direct link between growth optimisation and achievable device performance. [8]

4.2. Effect of deposition parameters on graphene film quality

4.2.1. Influence of deposition time on Graphene film (series 1)

The deposition parameters of series 1 where deposition time is varied while keeping other parameters constant and shown in table 4.1.

Table 4.1: Deposition parameters by deposition time variation (series 1)

Sample Name	Deposition time(t_d) (min)	Other parameters
HW323	**20**	Substrate temperature (T_s): 700^0C Annealing Temperature T_a): 700^0C Filament temperature (T_f): 2050 ± 50^0C Process Pressure (P.P.): 1mbar Annealing time: 45min CH_4 flow rate: 5 sccm H_2 flow rate 20 sccm
HW336	**15**	
HW338	**10**	
HW339	**5**	

All the graphene film transferred on silicon substrates show the characteristic peaks in Raman spectra (Fig. 4.2), ensuring the successful transfer of the films deposited on Ni substrate to Silicon substrate.

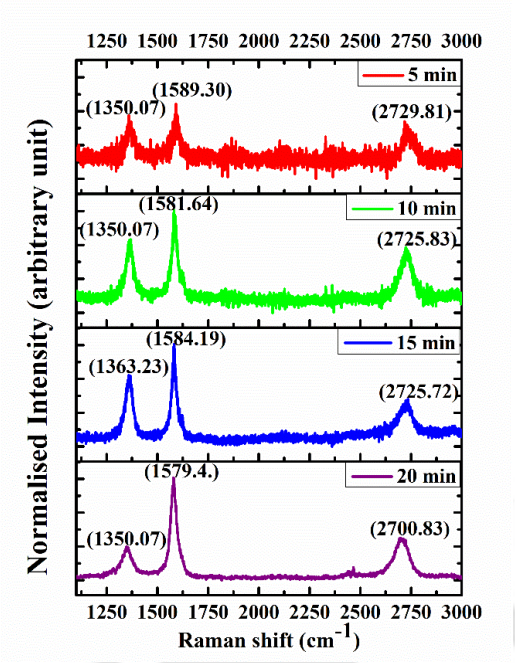

Fig. 4.2: Raman spectra of Graphene films with deposition time variation (series 1)

The Raman spectra corresponding to D peak, G peak and 2D peak and corresponding variation in I_D/I_G and I_{2D}/I_G ratios with different deposition times are reported offering key insights into the defect density and layer thickness of the deposited graphene. As the deposition time decreases from 20 minutes to 5 minutes, the I_D/I_G ratio rises from 0.32 to 0.88, and the I_{2D}/I_G ratio increases from 0.41 to 0.78, as shown in Fig. 4.2 and Table 4.2. The increase in I_D/I_G with reduced deposition time suggests a higher defect density in the graphene structure. In HWCVD, a longer deposition time allows a more uniform carbon diffusion onto the nickel substrate, leading to improved graphene quality during the cooling and segregation process. However, with a shorter deposition time, the carbon atoms have less time to nucleate and form a continuous, defect-free graphene network.

Table 4.2: I_D/I_G and I_{2D}/I_G values obtained from Raman spectra for Graphene films with deposition time variation (series 1)

Sample	I_D/I_G	I_{2D}/I_G
HW323 (20min)	0.32	0.41
HW336 (15min)	0.68	0.46
HW338 (10min)	0.71	0.64
HW339 (5min)	0.88	0.78

This results in a higher concentration of grain boundaries, edge defects, and vacancies, all of which contribute to the increased D-band intensity in Raman spectra.[9, 10] These observations align with prior studies indicating that smaller graphene domain sizes and incomplete growth result in increase in I_D/I_G ratio.[11] Moreover, the observed increase in the I_{2D}/I_G ratio indicates a reduction in graphene layer thickness as the deposition time decreases. A higher I_{2D}/I_G ratio generally signifies fewer graphene layers, with monolayer graphene (thickness ~0.335 nm) exhibiting the highest values. Shorter deposition times result in less carbon available for diffusion and segregation from the Ni substrate, thereby forming thinner graphene layers during the transfer process. For instance, at a deposition time of 20 minutes, prolonged carbon supply and diffusion lead to thicker graphene films, reflected by a lower I_{2D}/I_G ratio. Conversely, reducing the deposition time to 5 minutes yields thinner graphene layers, which enhances the relative intensity of the 2D peak compared to the G peak. These observations align with previous studies that have established a direct correlation between the I_{2D}/I_G ratio and graphene layer thickness.[12, 13]

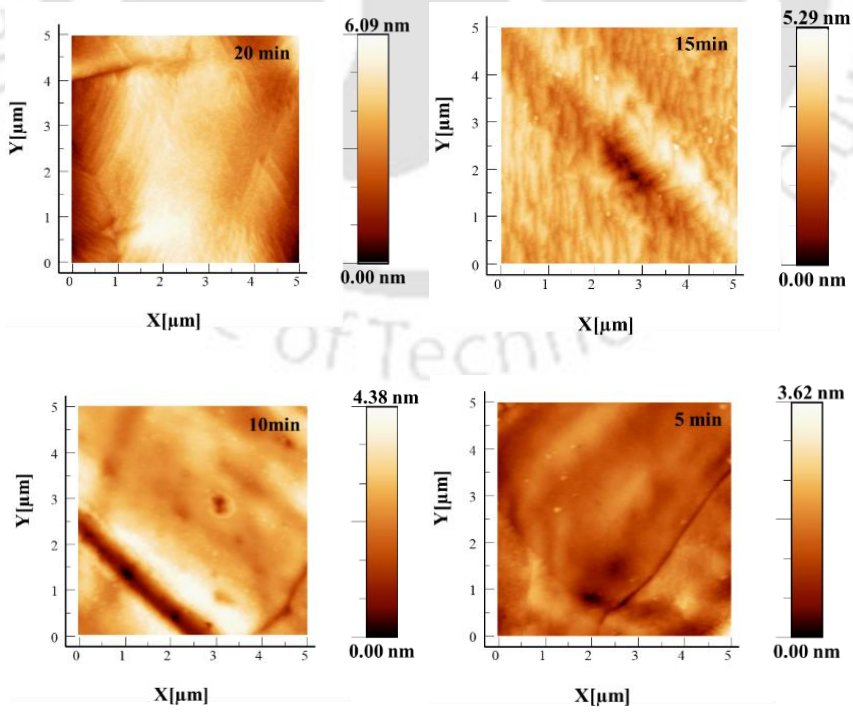

Fig. 4.3: AFM images of Graphene films with deposition time (a) 20min (b) 15min (c) 10min (d) 5min

The increase in I_D/I_G and I_{2D}/I_G with decreasing deposition time indicates a higher defect density and reduced graphene layer thickness. By optimizing the deposition time, it is possible to control defect concentration and layer uniformity, which are critical for graphene-based electronic and optoelectronic applications. AFM analysis (figure 4.3 and table 4.4) further confirms this trend, showing a decrease in root mean square (rms) roughness from 0.84 nm for the 20-minute sample to 0.38 nm for the 5-minute sample. Similarly, the average height reduced from 5.68 nm (10-15 layers) to 2.34 nm (8-10 layers), indicating thinner and smoother graphene films at shorter deposition times. The reduction in roughness suggests that longer deposition times lead to multilayer graphene growth with increased surface fluctuations, while shorter deposition times produce more uniform and continuous films. Similar trends have been reported in studies where reduced deposition time led to lower graphene surface roughness due to more controlled nucleation and limited layer stacking.[14, 15] The decrease in average height further supports the conclusion that the shorter deposition time results in thinner graphene films, which is in agreement with Raman spectroscopy results showing an increase in the I_{2D}/I_G ratio.

Table 4.3: RMS roughness and average height of Graphene films obtained from AFM analysis with deposition time variation

Sample Name	RMS Roughness	Average height
HW 323 (20 min)	0.84nm	5.68nm
HW 336 (15 min)	0.67nm	4.89nm
HW 338 (10min)	0.51nm	3.47nm
HW 339 (5 min)	0.38nm	2.34nm

These findings are consistent with AFM-based graphene studies, where surface topography analysis has been used to confirm the influence of growth time on thickness and uniformity.[16]

4.2.2. Influence of hydrogen dilution of methane on Graphene film (series 2)

Hydrogen plays a crucial role in graphene growth by facilitating the dissociation of methane into active carbon species while simultaneously etching amorphous and defective carbon, thereby influencing both defect density and film quality.[17-24], In order to understand the role of hydrogen flow rate on film quality, uniformity and number of graphene layers, the hydrogen flow rate is systematically varied from 10 sccm to 20 sccm, while maintaining a constant methane flow rate of 5 sccm and a deposition time of 5 minutes. This deposition time was specifically chosen to keep the number of graphene layers on the lower side while ensuring that hydrogen dilution enhances uniformity.

Table 4.4: Deposition parameters for hydrogen dilution of methane on Graphene film (series 2)

Sample Name	H_2 flow rate (sccm)	Other parameters
HW348	**10**	Substrate temperature (T_s): 700^0C Annealing Temperature T_a): 700^0C Filament temperature (T_f): 2050 ± 50^0C Process Pressure (P.P.): 1mbar Deposition time(t_d): 5 min Annealing time: 45min CH_4 flow rate: 5 sccm
HW349	**15**	
HW358	**20**	

Figure 4.2 presents the Raman spectra, while table 4.2 summarizes the corresponding variation in I_D/I_G and I_{2D}/I_G ratios with different deposition times, offering key insights into the defect density and layer thickness of the deposited graphene. As the deposition time decreases from 20 minutes to 5 minutes, the I_D/I_G ratio rises from 0.32 to 0.88, and the I_{2D}/I_G ratio increases from 0.41 to 0.78, as shown in Figure 4.2 and Table 4.2. As the hydrogen flow rate increased from 10 sccm to 20 sccm, significant changes were observed in the Raman spectral characteristics of the deposited graphene films (fig. 4.4).

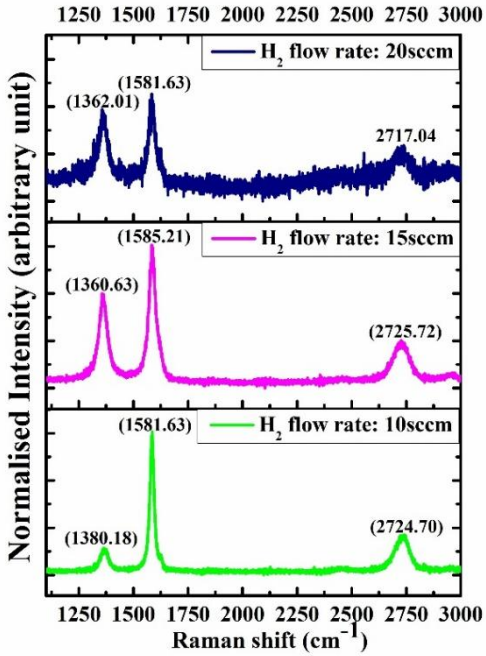

Fig. 4.4: Raman spectra of Graphene films with variation in hydrogen dilution of methane (series 2)

The I_D/I_G ratio, an indicator of defect density and structural disorder, increased from 0.19 to 0.85. This suggests that higher hydrogen concentrations lead to increased etching effects, introducing more defects such as vacancies and edge terminations.[21, 23, 25-27]

Table 4.5: I_D/I_G and I_{2D}/I_G values obtained from Raman spectra for Graphene films with hydrogen dilution of methane (series 2)

Sample	I_D/I_G	I_{2D}/I_G
HW348 (H_2: 10sccm)	0.19	0.28
HW349 (H_2: 15sccm)	0.66	0.32
HW358 (H_2:20sccm)	0.85	0.53

Simultaneously, the I_{2D}/I_G ratio, which provides insights into the number of graphene layers and their stacking order, increased from 0.28 to 0.53. This trend indicates that hydrogen dilution influences the balance between precursor dissociation and etching, potentially improving film uniformity while modifying layer structure.[28, 29]

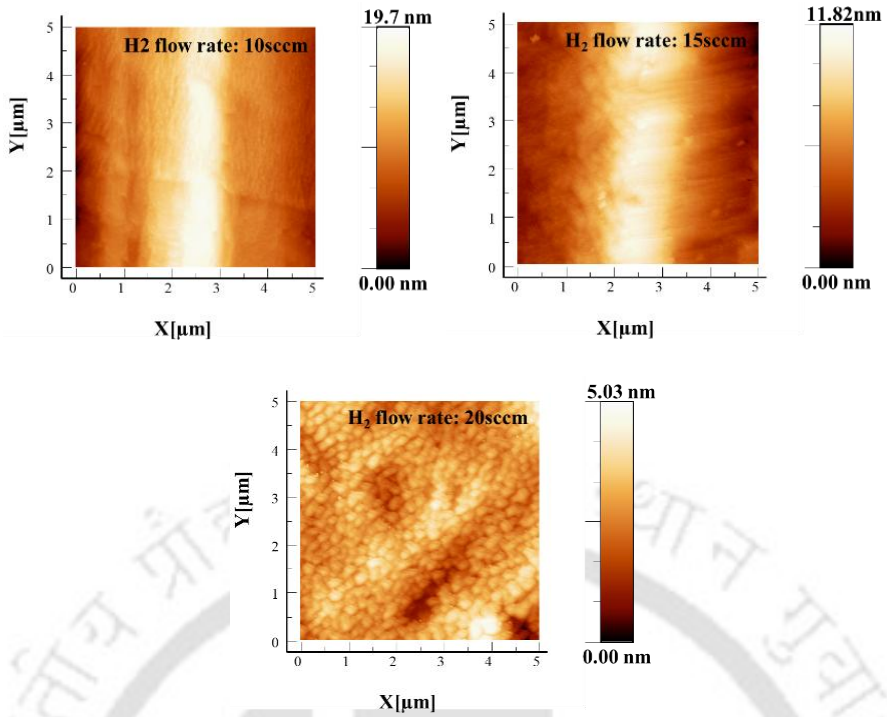

Fig. 4.5: AFM images of Graphene films with variation in hydrogen dilution of methane (a) 10sccm (b) 15sccm (c) 20sccm

From AFM analysis (figure 4.5, table 4.6) we observe that the rms roughness decreased from 2.32nm to 0.59nm and average height decreased from 9.82nm to 3.73nm when the hydrogen flow rates increased from 10sccm to 20 sccm.

Table 4.6: RMS roughness and average height of Graphene films obtained from AFM analysis with variation in hydrogen dilution of methane

Sample Name	RMS Roughness	Average height
HW348 (H_2:10sccm)	2.32nm	9.82nm
HW349 (H_2: 15sccm)	1.57nm	7.97nm
HW358 (H_2: 20sccm)	0.59nm	3.72nm

This is in line with raman studies and these findings highlight the importance of hydrogen dilution in tailoring the structural properties of graphene films grown via HWCVD. While lower hydrogen flow rates favour more ordered graphene with fewer defects, higher hydrogen concentrations enhance etching effects, affecting both uniformity and layer thickness.

Optimizing hydrogen-to-methane ratios is therefore critical for achieving graphene films with desirable properties for applications in nanoelectronics, flexible devices, and energy storage.

4.2.3. Influence of annealing temperature on Graphene film (series 3)

Graphene properties are significantly influenced by growth conditions and post-deposition treatments, such as annealing, which can modify its defect density, crystallinity, and layer stacking. For series 3, hydrogen flow rate of 20 sccm was chosen from series 2 to ensure efficient methane dissociation leading to improved uniformity and crystallinity. While it increases defect density, controlled defect engineering can be beneficial for tuneable electronic properties. Keeping this flow rate allows us to study how annealing temperature (700-780°C) influences defect healing, crystallinity, and layer rearrangement, optimizing graphene quality. The deposition parameters for series 3 are mentioned in table 4.7.

Table 4.7: Deposition parameters for annealing temperature of Graphene film (series 3)

Sample Name	Annealing Temperature (^{0}C)	Other parameters
HW360	**780**	Substrate temperature (T_s): 700^{0}C Filament temperature (T_f): 2050±50^{0}C Process Pressure (P.P.): 1mbar Deposition time(t_d): 5 min Annealing time: 45min CH_4 flow rate: 5 sccm H_2 flow rate: 20 sccm
HW361	**750**	
HW362	**700**	

To further investigate the graphene films were subjected to varying annealing temperatures.

At higher annealing temperatures, the mobility of carbon atoms increases, which may lead to defect migration and grain boundary modifications, affecting the overall film quality.[11, 30-35] Simultaneously, the I_{2D}/I_G ratio increased from 0.42 to 1.10, suggesting an improvement in graphitic ordering and possible decoupling of graphene layers. This trend can be attributed to the rearrangement of carbon atoms and relaxation of strain within the graphene lattice, leading to enhanced 2D band intensity.[12, 36]

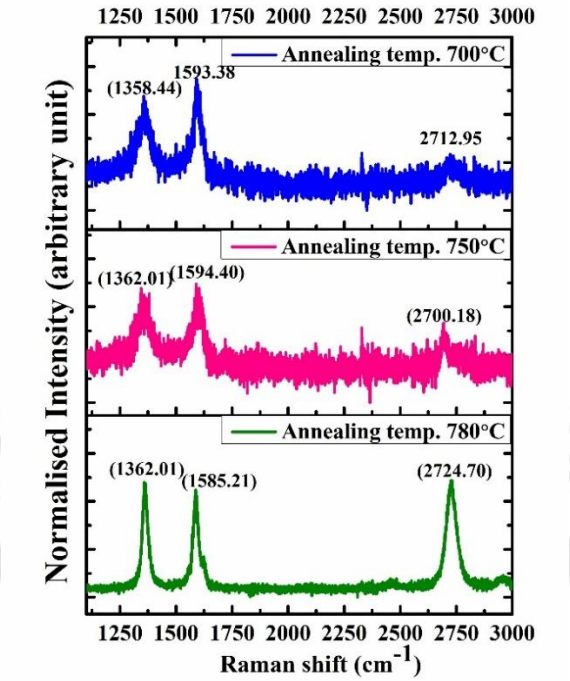

Fig. 4.6: Raman spectra of Graphene films with variation in annealing temperature (series 2)

However, the concurrent rise in the I_D/I_G ratio suggests that while structural ordering improves, additional defect sites are introduced, possibly due to thermal stress or incomplete healing of vacancies (missing carbon atoms in the hexagonal lattice structure). Additionally, the Raman peaks appear sharper and the overall spectra exhibit less noise. This improvement in peak sharpness and signal clarity can be attributed to enhanced crystalline quality in localized regions. Sharper peaks also suggest more uniform stress distribution within the graphene lattice, despite the increase in disorder indicated by the I_D/I_G ratio.

Table 4.8: I_D/I_G and I_{2D}/I_G values obtained from Raman spectra for Graphene films with annealing temperature variation (series 3)

Sample	I_D/I_G	I_{2D}/I_G
HW 360 (780^0C)	1.07	1.10
HW361 (750^0C)	0.94	0.67
HW362 (700^0C)	0.86	0.42

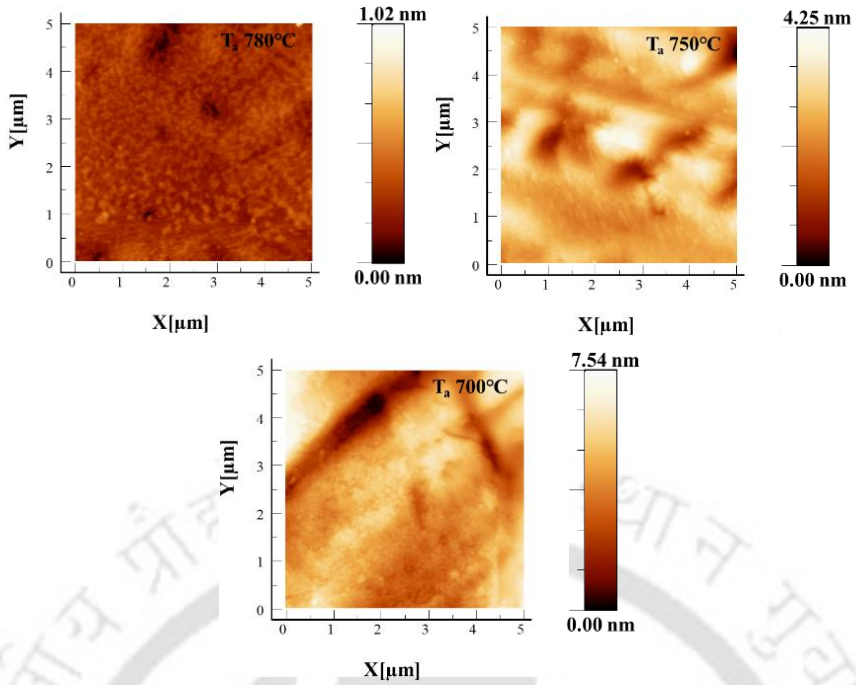

Fig. 4.7: AFM images of Graphene films with variation in annealing temperature (a) 780°C (b) 750°C (c) 700°C

AFM images (Fig. 4.7) and their analysis (Table 4.9) show a progressive decrease in RMS roughness and average height with increasing annealing temperature, indicating a reduction in the thickness and number of graphene layers. This thinning effect is attributed to enhanced carbon desorption and improved surface uniformity at higher temperatures. At the same time, Raman spectral analysis reveals changes in the ID/IG ratio, reflecting variations in defect density.

Table 4.9: RMS roughness and average height of Graphene films obtained from AFM analysis with variation in annealing temperature

Sample Name	RMS Roughness	Average height
HW 360 (780^0C)	0.22nm	0.97nm
HW361 (750^0C)	0.43nm	3.54nm
HW362 (700^0C)	0.78nm	5.32nm

Interestingly, while AFM results suggest smoother and thinner graphene films, the increase in ID/IG ratio indicates the formation of defects such as vacancies or edge disorders. This apparent contradiction highlights the interlinked nature of morphological and structural

changes: as annealing promotes better atomic ordering and layer uniformity (observed in AFM), it can also induce localized defects due to thermal stress, strain relaxation, or incomplete healing (detected in Raman spectra). Therefore, the combined AFM and Raman analyses emphasize the complex interplay between defect generation and crystallinity enhancement during post-deposition annealing, where improvements in surface morphology coincide with the introduction of atomic-scale defects.

4.3. Conclusion

We have successfully deposited bi-layer to multi-layer graphene films on nickel substrates using Hot Wire Chemical Vapor Deposition (HWCVD). The high deposition rate of HWCVD resulted in a minimum number of graphene layers (bi-layer graphene) after just 5 minutes of deposition. As the deposition time increased, the number of layers grew, which was further confirmed by Raman and AFM analysis. The study also revealed that the number of graphene layers and the uniformity of the films decreased with an increase in hydrogen dilution of methane, as hydrogen enhanced methane dissociation and etching, leading to thinner graphene layers with more defects. Additionally, post-deposition annealing treatments showed a decrease in the number of graphene layers with increasing annealing temperature. This trend suggests that higher temperatures may promote the decoupling or reduction of graphene layers, possibly due to thermal stress or rearrangement of carbon atoms.

4.4. References

1. Chen, Y., X.L. Gong, and J.G. Gai, *Progress and Challenges in Transfer of Large-Area Graphene Films.* Adv Sci (Weinh), 2016. **3**(8): p. 1500343.
2. Van Ngoc, H., Y. Qian, S.K. Han, and D.J. Kang, *PMMA-Etching-Free Transfer of Wafer-scale Chemical Vapor Deposition Two-dimensional Atomic Crystal by a Water Soluble Polyvinyl Alcohol Polymer Method.* Sci Rep, 2016. **6**: p. 33096.
3. Langston, X. and K.E. Whitener, Jr., *Graphene Transfer: A Physical Perspective.* Nanomaterials (Basel), 2021. **11**(11).
4. Borin Barin, G., Y. Song, I. de Fátima Gimenez, A.G. Souza Filho, L.S. Barreto, and J. Kong, *Optimized graphene transfer: Influence of polymethylmethacrylate (PMMA) layer concentration and baking time on graphene final performance.* Carbon, 2015. **84**: p. 82-90.

5. Macías, C., A. Cavanna, A. Madouri, S. Béchu, S. Collin, J.-C. Harmand, A. Cattoni, and A. Delamarre, *Optimized Ni-assisted graphene transfer to GaAs surfaces: Morphological, structural, and chemical evolution of the 2D-3D interface.* Applied Surface Science, 2024. **676**.
6. Choi, M., J. Baek, H. Zeng, S. Jin, and S. Jeon, *Toward high-quality graphene film growth by chemical vapor deposition system.* Current Opinion in Solid State and Materials Science, 2024. **31**.
7. Mattevi, C., H. Kim, and M. Chhowalla, *A review of chemical vapour deposition of graphene on copper.* J. Mater. Chem., 2011. **21**(10): p. 3324-3334.
8. Li, X., L. Colombo, and R.S. Ruoff, *Synthesis of Graphene Films on Copper Foils by Chemical Vapor Deposition.* Adv Mater, 2016. **28**(29): p. 6247-52.
9. Ma, H., L. Yu, and R. Lv, *Defect-induced enhanced Raman scattering of two-dimensional materials.* Materials Today, 2025.
10. Luo, Z., C. Cong, J. Zhang, Q. Xiong, and T. Yu, *The origin of sub-bands in the Raman D-band of graphene.* Carbon, 2012. **50**(11): p. 4252-4258.
11. Masudy-Panah, S., R.S. Moakhar, C.S. Chua, A. Kushwaha, T.I. Wong, and G.K. Dalapati, *Rapid thermal annealing assisted stability and efficiency enhancement in a sputter deposited CuO photocathode.* RSC Advances, 2016. **6**(35): p. 29383-29390.
12. Malard, L.M., M.A. Pimenta, G. Dresselhaus, and M.S. Dresselhaus, *Raman spectroscopy in graphene.* Physics Reports, 2009. **473**(5-6): p. 51-87.
13. Cancado, L.G., A. Jorio, E.H. Ferreira, F. Stavale, C.A. Achete, R.B. Capaz, M.V. Moutinho, A. Lombardo, T.S. Kulmala, and A.C. Ferrari, *Quantifying defects in graphene via Raman spectroscopy at different excitation energies.* Nano Lett, 2011. **11**(8): p. 3190-6.
14. Bao, W., G. Liu, Z. Zhao, H. Zhang, D. Yan, A. Deshpande, B. LeRoy, and C.N. Lau, *Lithography-free fabrication of high quality substrate-supported and freestanding graphene devices.* Nano Research, 2010. **3**(2): p. 98-102.
15. Lee, S., K. Lee, and Z. Zhong, *Wafer scale homogeneous bilayer graphene films by chemical vapor deposition.* Nano Lett, 2010. **10**(11): p. 4702-7.
16. Obraztsov, A.N., E.A. Obraztsova, A.V. Tyurnina, and A.A. Zolotukhin, *Chemical vapor deposition of thin graphite films of nanometer thickness.* Carbon, 2007. **45**(10): p. 2017-2021.
17. Bhardwaj, J.S., A. Singh, and P. Agarwal, *Work function tuning of directly grown multi-layer graphene on silicon by PECVD and fabrication of Ag/ITO/Gr/n-Si/Ag solar cell.* Diamond and Related Materials, 2025. **155**.
18. Dhaouadi, E., W. Alimi, I. Hinkov, M. Abderrabba, and S. Farhat, *Graphene synthesis by electromagnetic induction heating: Domain size and morphology control.* Diamond and Related Materials, 2024. **144**.
19. Vlassiouk, I., M. Regmi, P. Fulvio, S. Dai, P. Datskos, G. Eres, and S. Smirnov, *Role of hydrogen in chemical vapor deposition growth of large single-crystal graphene.* ACS Nano, 2011. **5**(7): p. 6069-76.
20. Salehi, M., P. Bastani, L. Jamilpanah, A. Madani, S.M. Mohseni, and B. Shokri, *Low defect and high electrical conductivity of graphene through plasma graphene healing treatment monitored with in situ optical emission spectroscopy.* Sci Rep, 2021. **11**(1): p. 20334.
21. Qin, X., O. Ola, J. Zhao, Z. Yang, S.K. Tiwari, N. Wang, and Y. Zhu, *Recent Progress in Graphene-Based Electrocatalysts for Hydrogen Evolution Reaction.* Nanomaterials (Basel), 2022. **12**(11).
22. Ani, M.H., M.A. Kamarudin, A.H. Ramlan, E. Ismail, M.S. Sirat, M.A. Mohamed, and M.A. Azam, *A critical review on the contributions of chemical and physical factors toward the nucleation and growth of large-area graphene.* Journal of Materials Science, 2018. **53**(10): p. 7095-7111.
23. Li, P., Z. Li, and J. Yang, *Dominant Kinetic Pathways of Graphene Growth in Chemical Vapor Deposition: The Role of Hydrogen.* The Journal of Physical Chemistry C, 2017. **121**(46): p. 25949-25955.
24. Li, K., C. He, M. Jiao, Y. Wang, and Z. Wu, *A first-principles study on the role of hydrogen in early stage of graphene growth during the CH4 dissociation on Cu(111) and Ni(111) surfaces.* Carbon, 2014. **74**: p. 255-265.

25. Zhang, X., L. Wang, J. Xin, B.I. Yakobson, and F. Ding, *Role of hydrogen in graphene chemical vapor deposition growth on a copper surface.* J Am Chem Soc, 2014. **136**(8): p. 3040-7.
26. Ma, T., W. Ren, X. Zhang, Z. Liu, Y. Gao, L.C. Yin, X.L. Ma, F. Ding, and H.M. Cheng, *Edge-controlled growth and kinetics of single-crystal graphene domains by chemical vapor deposition.* Proc Natl Acad Sci U S A, 2013. **110**(51): p. 20386-91.
27. Lin, H., T. Buerki-Thurnherr, J. Kaur, P. Wick, M. Pelin, A. Tubaro, F.C. Carniel, M. Tretiach, E. Flahaut, D. Iglesias, E. Vazquez, G. Cellot, L. Ballerini, V. Castagnola, F. Benfenati, A. Armirotti, A. Sallustrau, F. Taran, M. Keck, C. Bussy, S. Vranic, K. Kostarelos, M. Connolly, J.M. Navas, F. Mouchet, L. Gauthier, J. Baker, B. Suarez-Merino, T. Kanerva, M. Prato, B. Fadeel, and A. Bianco, *Environmental and Health Impacts of Graphene and Other Two-Dimensional Materials: A Graphene Flagship Perspective.* ACS Nano, 2024. **18**(8): p. 6038-6094.
28. Wu, S., D. Huang, H. Yu, S. Tian, A. Malik, T. Luo, and G. Xiong, *Molecular understanding of the effect of hydrogen on graphene growth by plasma-enhanced chemical vapor deposition.* Phys Chem Chem Phys, 2022. **24**(17): p. 10297-10304.
29. Naghdi, S., K.Y. Rhee, and S.J. Park, *A catalytic, catalyst-free, and roll-to-roll production of graphene via chemical vapor deposition: Low temperature growth.* Carbon, 2018. **127**: p. 1-12.
30. Piazolo, S., M. Bestmann, D.J. Prior, and C.J. Spiers, *Temperature dependent grain boundary migration in deformed-then-annealed material: Observations from experimentally deformed synthetic rocksalt.* Tectonophysics, 2006. **427**(1-4): p. 55-71.
31. Xu, L., J. Yang, K. Li, L. Yang, and J. Zhu, *Effect of Post-Deposition Annealing on the Structural Evolution and Optoelectronic Properties of In(2)O(3):H Thin Films.* Nanomaterials (Basel), 2022. **12**(19).
32. Zöllner, D., *Impact of a strong temperature gradient on grain growth in films.* Modelling and Simulation in Materials Science and Engineering, 2022. **30**(2).
33. Lin, S.-H., Y.-H. Chang, Y.-J. Huang, Y.-T. Chen, and S.-H. Dong, *Annealing Temperature Effect on the Properties of CoCe Thin Films Prepared by Magnetron Sputtering at Si(100) and Glass Substrates.* Processes, 2024. **12**(12).
34. Aihaiti, L., K. Tuokedaerhan, B. Sadeh, M. Zhang, X. Shen, and A. Mijiti, *Effect of Annealing Temperature on Microstructure and Resistivity of TiC Thin Films.* Coatings, 2021. **11**(4).
35. Zang, J., Y. Ma, Y. Zhao, R. Guo, Y. Liu, D. Liu, and C. Xue, *Effect of post-annealing treatment on the thermoelectric properties of Ag2Se flexible thin film prepared by magnetron sputtering method.* Results in Physics, 2023. **45**.
36. Mohandoss, M., S.S. Gupta, A. Nelleri, T. Pradeep, and S.M. Maliyekkal, *Solar mediated reduction of graphene oxide.* RSC Advances, 2017. **7**(2): p. 957-963.

Chapter 5

Work function tunning of directly grown multi-layer Graphene on Silicon substrate by PECVD and HWCVD and Solar cell fabrication

This chapter reports production of large-area, high-quality graphene directly on silicon substrate without metallic catalyst for its application in various semiconductor devices. Graphene films are deposited by PECVD (Plasma Enhanced Chemical Vapor Deposition) and HWCVD (Hot wire Chemical Vapor Deposition) with tunable variable work function based on number of layers of Graphene. This has been performed by varying deposition parameters such as process pressure, deposition temperature, deposition time, etc. To confirm the quality of Graphene, Raman, and XPS studies have been performed. The uniformity of the films has been confirmed by FESEM and surface roughness analysis is done by AFM. EDAX has been performed to study the C/Si ratio in the films. The work function has been measured through surface potential mapping by KPFM. The work function of samples deposited by HWCVD

exhibited a variation from 4.38 to 4.92 eV, while samples deposited by PECVD showed a work function range from 4.25 to 4.54 eV, achieved by adjusting the methane and hydrogen gas flow rates. The Solar cell has been fabricated using optimal graphene deposition condition with device structure Ag/ITO/Gr/n-Si/Ag having efficiency of 1%, current density of 25.52mA/cm^2, V_{oc} of 0.13V and FF of 0.29.

5.1 Experimental Details

5.1.1 Deposition of Graphene on Silicon substrate by HWCVD

Graphene is deposited directly on n-type silicon wafer (~250 µm thick, (100), with 1-10 ohm-cm resistivity). Firstly, silicon substrate is cleaned with HF (hydrofluoric Acid) followed by ultra-sonication in DI water, Propanol and then nitrogen drying to remove the naturally grown SiO_2 layer and other impurities. After this, the substrate is loaded to the vacuum chamber of HWCVD (Hot Wire Chemical Vapor Deposition) System. The silicon surface was then heated and stabilized at 450°C under high vacuum (~10^{-6} mbar) and afterwards, film is deposited. Further, the deposited film is annealed for 1 hour to reduce defects and contamination and to improve crystallinity and graphene-silicon interface. Two series of samples are deposited at 450°C and 1 mbar of process pressure for this study. In the first series, the deposition time is varied from 2-10min and in the second series, H_2 flow rate is varied from 30-80 sccm keeping other parameters same. The deposition parameters are mentioned in Table 5.1.

5.1.2 Deposition of Graphene on Silicon substrate by PECVD

Graphene is deposited directly on n-type silicon wafer (~250 µm thick, (100), with 1-10 ohm-cm resistivity). Firstly, silicon substrate is cleaned with HF (hydrofluoric Acid) followed by ultra-sonication in DI (Deionized) water, Propanol and then nitrogen drying to remove the naturally grown SiO_2 layer and other impurities. After this, the substrate is loaded to the vacuum chamber of PECVD (Plasma Enhanced Chemical Vapor Deposition) System. The

silicon surface is then heated and stabilized at (450°C) under high vacuum (~10^{-6} mbar) and afterwards, film is deposited. We have deposited two series of samples at 450°C and 1 mbar of process pressure for this study by varying the H_2 and CH_4 flow rate. After the deposition, the film is annealed for 40 min to enhance graphene's crystallinity, reduce defects, remove residual contaminants, relax thermal stresses, improve the graphene-silicon interface, and boost electrical properties, [1-3] The deposition parameters are mentioned in Table 5.2.

Table 5.1: Deposition parameters for Graphene film by HWCVD

Sample	H_2 flow rate (sccm)	CH_4 flow rate (sccm)	Deposition time (min)	Other Parameters
Series 1				Substrate temperature: 450°C Filament temperature: 2050±50°C Annealing Temperature: 450°C Process Pressure: 1mbar Annealing time: 60min
HW363	10	20	2	
HW362	10	20	5	
HW361	10	20	10	
Series 2				
HW373	30	20	10	
HW372	50	20	10	
HW370	80	20	10	

Table 5.2: Deposition parameters for Graphene film by PECVD

Sample	H_2 flow rate (sccm)	CH_4 flow rate (sccm)	Other Parameters
Series 1			Deposition temperature: 450°C Rf Power: 60W Process Pressure: 1mbar Deposition time: 40min
MP260	80	10	
MP261	60	10	
MP262	40	10	
Series 2			
MP263	80	7	
MP264	60	7	
MP265	40	7	

The different methane and hydrogen flow rates in graphene deposition via HWCVD and PECVD are due to their distinct dissociation mechanisms. In HWCVD, high filament temperatures thermally decompose methane into reactive carbon species, necessitating a higher methane flow to supply sufficient carbon for graphene growth, while a lower hydrogen flow prevents over-etching of carbon species. Conversely, PECVD employs plasma to dissociate

methane at lower temperatures, generating hydrogen radicals that etch amorphous carbon and enhance graphene quality, thus requiring a higher hydrogen flow to produce adequate radicals for surface cleaning and defect passivation, with a lower methane flow providing the necessary carbon source. [2-6]

5.1.3 Solar cell fabrication and measurements

The Graphene/silicon heterojunction solar cell is fabricated with device structure Ag/ITO/Gr/n-Si/Ag. Further for better charge collection, ITO (Indium Tin Oxide (In_2O_3:SnO_2=90:10)) is introduced as TCO (Transparent Conducting Oxide) layer to improve the efficiency of the device and device with structure Ag/ITO/Gr/n-Si/Ag is fabricated. For this, Graphene film (MP265) is deposited by PECVD based on the optimized deposition conditions. Here, silver is used as contacts. The fabricated device is of circular shape with 4mm diameter with device area of 11.31mm^2(10% area reduced due to electrode formation). The deposition parameters for ITO deposited by rf sputtering are mentioned in table 5.3.

Table 5.3: Deposition Parameters for ITO deposited by rf sputtering

Rf-power (W)	Deposition time (min)	Deposition temperature (°C)	Process Pressure (mbar)	Argon Flow rate (sccm)
80	8	150	0.06	7

The schematic structure for the fabricated solar cell is as shown in Fig. 5.1. For the fabricated device, current vs. voltage (J-V) measurements were performed under dark and standard AM 1.5 illumination conditions using ScienceTech solar simulator with a Keithley 2400 source meter. Device photovoltaic characteristic parameters, open circuit voltage (V_{oc}) and short circuit current (J_{sc}), fill factor (FF), and PCE were calculated from the measured J- V curves under illumination.

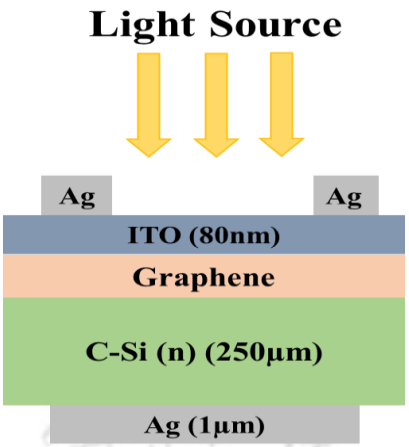

Fig. 5.1: Schematic device structure of fabricated solar cell

5.1.4 KPFM for surface potential mapping of Graphene films

Kelvin Probe Scanning Force Microscopy (KPFM) measurements were performed on the deposited Graphene thin films for surface potential mapping to determine the work function. In this, the contact potential difference (CPD) in between the conducting tip of the instrument and sample is measured, which is further used to determine the work function of samples. (equation 1)[7, 8].

$$eCPD_{sample} = \Phi_{tip} - \Phi_{sample} \quad (5.1)$$

Here e is the charge of electron, Φ_{tip} is the work function of the tip and Φ_{sample} is the work function value of sample.

To determine the value of Φ_{tip}, we used film of Highly oriented pyro-electric graphite (HOPG) (Φ = 4.6eV) as reference due to its non-sensitivity towards contamination and no dipole formation. From HOPG, work function of tip (Φ_{tip}) is calculated. (Equation 2)

$$\Phi_{tip} = \Phi_{HOPG} + eCPD_{HOPG} \quad (5.2)$$

Finally, from equation 5.1 and 5.2, the work function of sample is calculated as shown in equation 3. [9, 10]

$$\Phi_{sample} = 4.6\ eV + e[CPD_{HOPG} - CPD_{sample}] \quad (5.3)$$

Graphene's work function is primarily influenced by the number of graphene layers and the uniformity of the film during deposition. In monolayer graphene, the Fermi level is located at the Dirac point. However, as additional layers are introduced, interlayer interactions modify the electronic band structure, leading to shifts in the Fermi level. These modifications directly affect the work function of graphene, emphasizing the significance of controlling layer thickness and deposition uniformity to tailor its electronic properties for specific applications.[11-13]

Upon biasing the graphene film, Kelvin Probe Force Microscopy (KPFM) allows us to accurately measure graphene/metal contact resistances by mapping the surface potential of a device. Fig. 5.2 shows the schematic of fermi level shift when the work function changes.

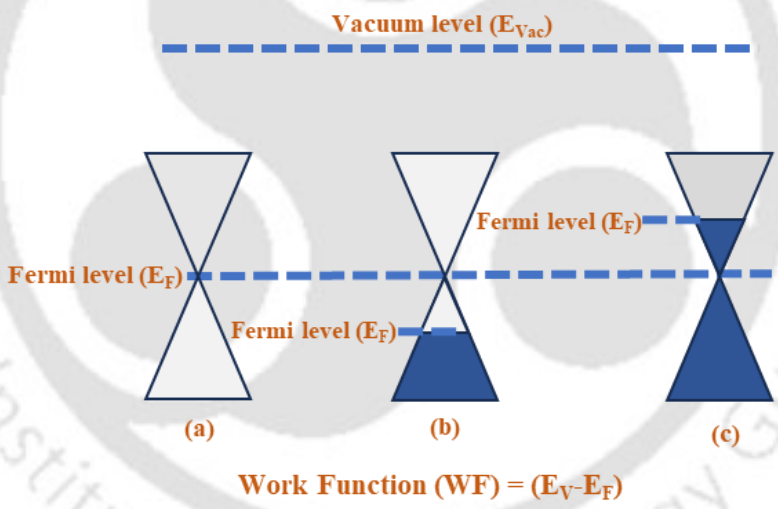

Fig. 5.2: Schematic diagram of energy band of (a) pristine graphene (c) increasing the WF of graphene, (b) decreasing the WF of graphene.

5.2 Results and Discussion

5.2.1 Growth of multi-layer Graphene on silicon substrate by HWCVD

In the first series (HW361 to HW363), the deposition time is varied by keeping other parameters constant.

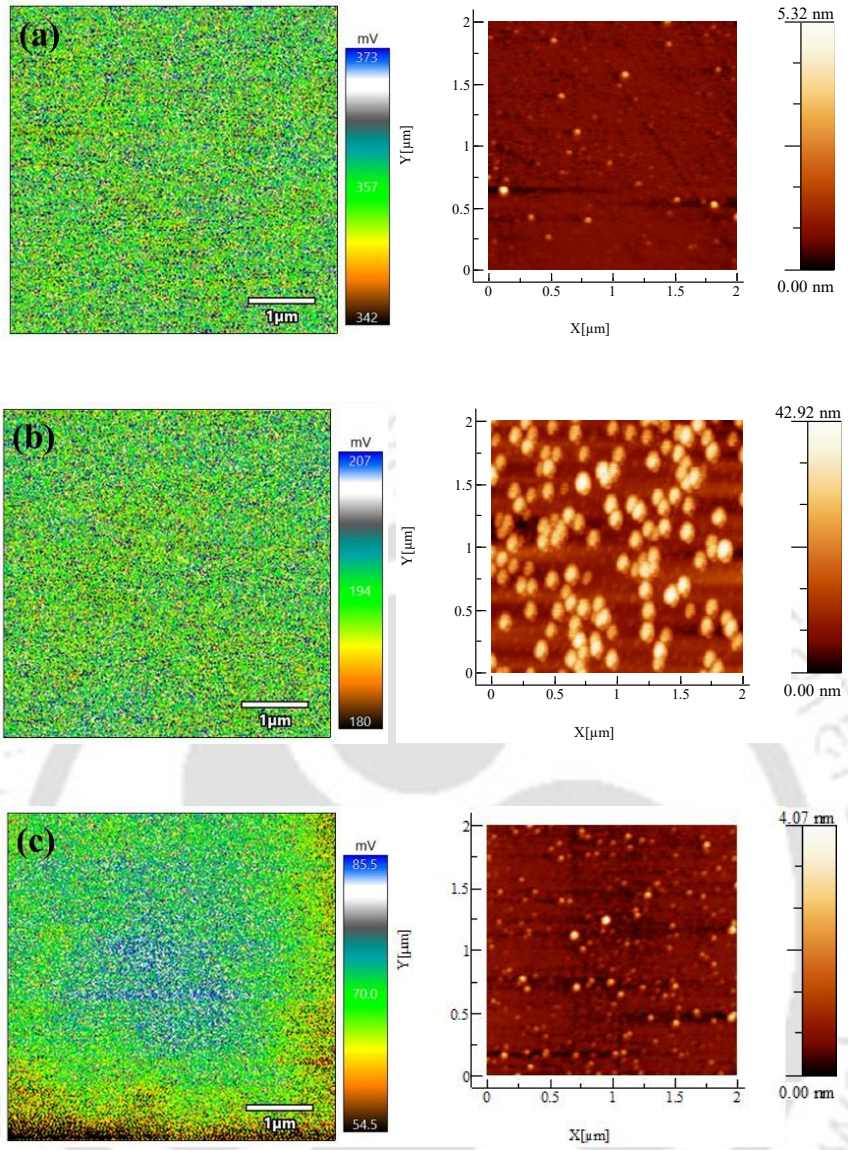

Fig. 5.3: CPD mapping, and AFM images of as-grown graphene film by HWCVD (a) HW361 (10min), (b) HW362 (5min), (c) HW363 (2min)

Atomic Force Microscopy (AFM) measurements were performed in tapping mode to analyze the surface morphology and layer thickness of graphene films deposited for different time durations. Figure 5.3 presents the AFM images, while the corresponding roughness parameters are summarized in Table 5.4. The surface roughness values provide insights into the uniformity and thickness variations of the deposited graphene layers. For a deposition time of 10 minutes (HW361), AFM analysis reveals the formation of multilayer graphene with relatively high surface roughness. The increased roughness can be attributed to the variation in the number of graphene layers across the substrate, leading to non-uniform stacking. The presence of multiple

graphene layers suggests that the growth rate is substantial over this duration, likely due to sustained carbon accumulation on the substrate. By reducing the deposition time to 5 minutes (sample HW362), an increase in the film deposition area is observed (Fig. 5.3(b)); however, the surface coverage remains incomplete. Due to the non-uniform nature of the film, the average height serves as an indicator of the number of graphene layers. The measured average height of 0.9 nm (Fig. 5.3(b) and Table 5.4) suggests that the deposited graphene film consists of 2 to 4 layers. This result demonstrates that reducing the exposure time to the carbon precursor effectively limits excessive layer growth. However, thickness variations across the substrate persist, indicating that further optimization is necessary to achieve improved uniformity and consistent layer distribution.[14, 15]

Kelvin Probe Force Microscopy (KPFM) was employed to map the contact potential difference (CPD) and determine the work function of the graphene films. As shown in Figure 5.3, the work function decreases from 4.67eV(2min) to 4.38eV(10min) with increasing deposition time. This trend is attributed to the progressive reduction in film thickness and the corresponding decrease in the number of layers. In multilayer graphene, interlayer interactions promote charge redistribution, lowering the effective work function due to enhanced screening effects. As the thickness decreases, reduced interlayer coupling modifies the electronic structure, leading to an increase in the measured work function.

Furthermore, the work function of graphene is influenced by substrate interactions, doping effects, and intrinsic defects. Thinner graphene films exhibit stronger substrate interactions, which can alter their electronic properties. Variations in surface roughness, defects, or local doping concentrations may also contribute to observed work function differences.

The deposition parameters along with average CPD, calculated work function, rms roughness and average height are summarized in table 5.4.

To achieve more uniform coverage while maintaining the minimum number of graphene layers, optimization of deposition parameters is necessary. One potential approach is to adjust the hydrogen dilution ratio of methane during the deposition process. Hydrogen plays a crucial role in regulating graphene growth by etching excess carbon and promoting layer-by-layer formation.[16, 17] Increasing hydrogen dilution could help in enhancing surface diffusion, thereby improving uniformity while controlling the thickness of the deposited graphene. Moreover, a dynamic adjustment of hydrogen concentration over time might ensure a gradual and controlled growth process, reduce abrupt layer variations and enhance the lateral continuity of the graphene film.

Table 5.4: AFM and KPFM parameters of series 1 graphene film by HWCVD

Sample	H_2 flow rate (sccm)	CH_4 flow rate (sccm)	Deposition time	Avg. CPD (mV)	Work function (eV)	Rms roughness (nm)	Average height (nm)	$\frac{CH_4}{CH_4+H_2}$
HW363	10	20	2	70.02	4.67	0.27nm	0.58nm	0.67
HW362	10	20	5	193.83	4.55	0.28nm	0.9nm	0.67
HW361	10	20	10	357.49	4.38	8.20nm	14.56nm	0.67

In series 2, the methane-to-hydrogen gas ratio was systematically varied, as detailed in Tables 5.2 and 5.5. The primary objective was to enhance hydrogen dilution to facilitate the dissociation of CH_4, thereby promoting the formation of uniform graphene films with controlled thickness. Hydrogen plays a critical role in regulating graphene growth by influencing precursor decomposition, etching excess carbon, and modifying surface diffusion dynamics. Despite obtaining multi-layered graphene at 10 minutes in series 1, we maintained this deposition time to balance thickness control and uniformity. Shorter durations reduce layers but risk non-uniform growth. Increasing hydrogen dilution enhanced CH_4 dissociation and etching, promoting sp^2 carbon formation while preventing excessive deposition.[18, 19] As shown in Figure 5.4 and Table 5.5, films deposited with 30 sccm hydrogen dilution exhibit

uniform coverage, but their average thickness of approximately 26 nm indicates graphitic nature of the film. This suggests that while hydrogen helps regulate carbon deposition, the chosen methane-to-hydrogen ratio still promotes excessive layer growth.

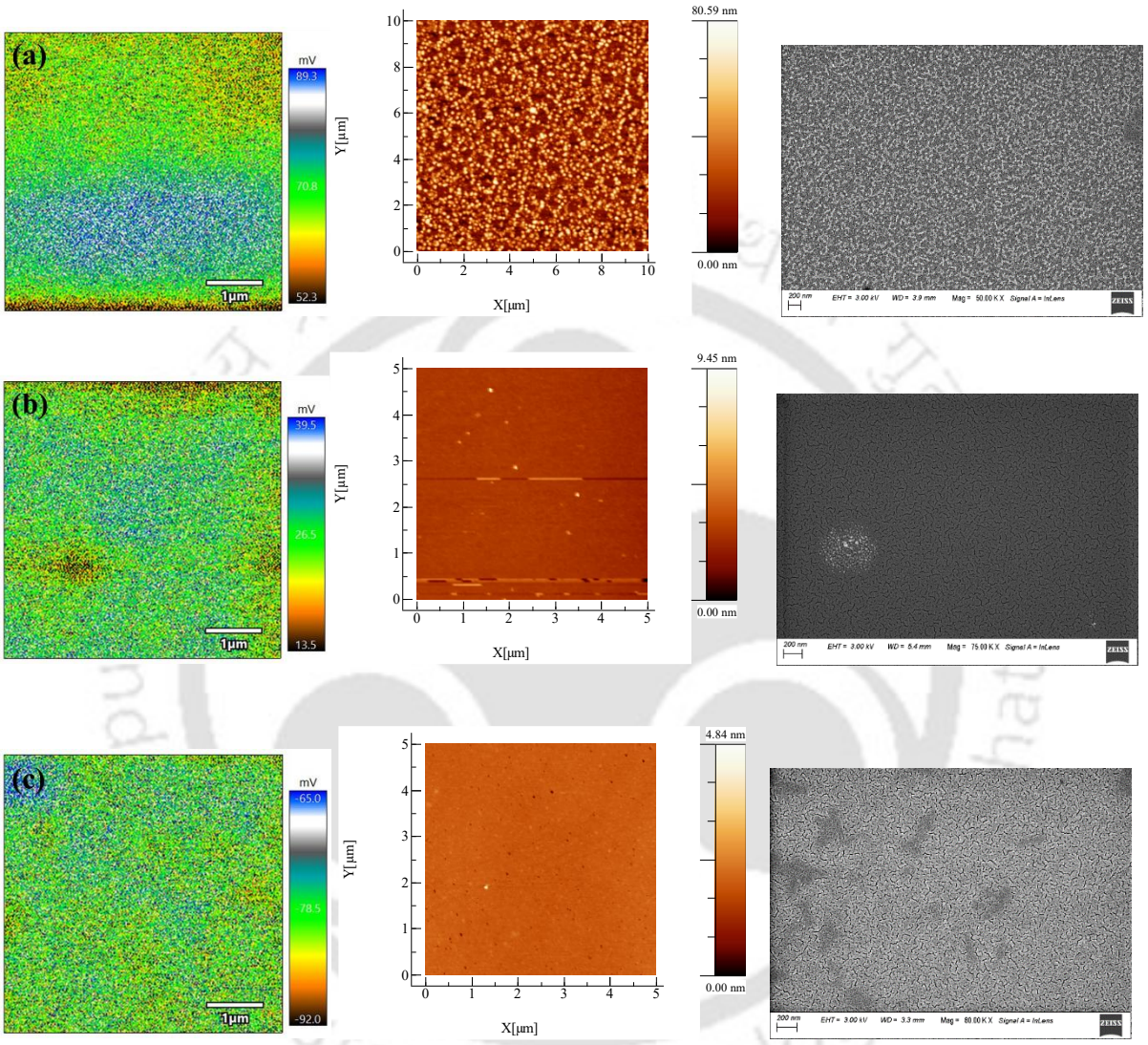

Fig. 5.4: CPD mapping, AFM images, and FESEM images of as-grown graphene film of series 2 by HWCVD (a) H_2=30sccm, CH_4=20sccm, (b) MP261 H_2=50sccm, CH_4=20sccm, (c) H_2=80sccm, CH_4=20sccm

AFM and FESEM images (Figure 5.4) reveal that increasing hydrogen dilution from 30 sccm to 80 sccm significantly reduces film uniformity and surface coverage. This can be attributed to hydrogen's enhanced etching effect, which prevents excessive layer accumulation but also limits nucleation density, disrupting film continuity. At higher hydrogen dilution, a significant reduction in deposition area coverage is observed due to intensified etching and reduced

availability of active carbon species essential for graphene nucleation. Additionally, increased hydrogen flow may induce a sweeping effect, where methane is displaced more rapidly, limiting its dissociation and subsequent graphene growth. These findings highlight the importance of optimizing the methane-to-hydrogen ratio to achieve uniform graphene deposition while minimizing excessive etching and ensuring sufficient carbon availability. The AFM and KPFM results of series 2 are summarized in table 5.5.

Table 5.5: AFM and KPFM parameters of series 2 graphene film by HWCVD

Sample	H_2 flow rate (sccm)	CH_4 flow rate (sccm)	Deposition time	Avg. CPD (mV)	Work function (eV)	Rms roughness (nm)	Average height (nm)	$\frac{CH_4}{CH_4 + H_2}$
HW373	30	20	10	70.83	4.67	15.55nm	26.65nm	0.40
HW372	50	20	10	26.43	4.71	0.34nm	2.66nm	0.28
HW370	80	20	10	-78.52	4.92	0.17nm	1.9nm	0.20

For the film with H_2 flow rate of 30 sccm and CH_4 flow rate of 20 sccm, Further EDX, Raman and Spectroscopic ellipsometry measurements are performed. This film is used as it has maximum uniformity. Energy Dispersive X-ray Spectroscopy (EDX) analysis was performed to confirm the growth of carbon films on the silicon substrate, as illustrated in Figure 5.5. The elemental mapping results indicate the presence of approximately 23 atomic% carbon and 77 atomic% silicon in the sample, suggesting that carbonaceous material has been successfully deposited onto the substrate. Detection of carbon in the EDX spectra confirms the presence of a graphene-based film. However, the high silicon content observed in the spectra is attributed to the ultrathin nature of the deposited carbon layers. Unlike bulk carbon films, few-layer graphene exhibits extremely low thickness (typically a few nanometers), which allows the incident electron beam to penetrate through the graphene and interact with the underlying

silicon substrate. As a result, the detected X-ray emissions contain a substantial contribution from the substrate, leading to a strong silicon signal in the EDX spectra.[20, 21]

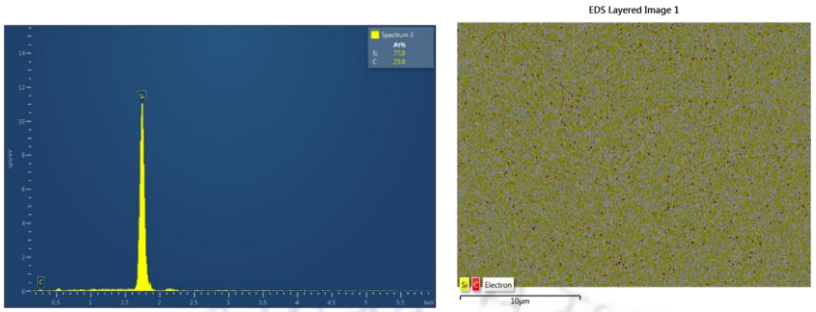

Fig. 5.5: EDX Analysis of Graphene film (H_2: 30sccm; CH_4: 20sccm) on Silicon

Raman measurements (Figure 5.6) were performed using a 633 nm excitation wavelength to analyze the structural characteristics of the deposited graphene films. The spectra exhibit distinct peaks corresponding to the D band at 1342 cm^{-1}, the G band at 1604 cm^{-1}, and the 2D band at 2687 cm^{-1} for sample HW361, confirming the successful deposition of graphene. The presence of the D band suggests some degree of disorder, likely due to structural defects or edges, while the G band corresponds to the in-plane vibration of sp^2 carbon atoms. The 2D band, which is a signature of graphene, provides insights into the layer number and stacking order. The observed spectral irregularities, such as broadening or noise in the Raman signal, may be attributed to the low film thickness, which results in weaker Raman scattering due to reduced interaction volume.

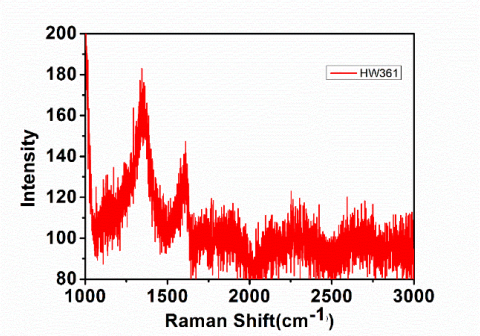

Fig. 5.6: Raman spectra of Graphene film (H_2: 30sccm; CH_4: 20sccm) at 633nm excitation wavelength

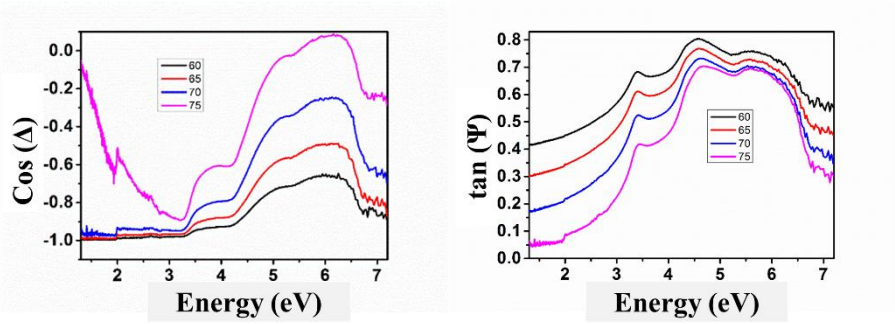

Fig. 5.7: Ellipsometic spectra of Tan (Psi) and Cos (Delta) values for Graphene film (H_2: 30sccm; CH_4: 20sccm) by varying angle of incidence from 60˚ to 75˚

Spectroscopic ellipsometry (Figure 5.7) was performed by varying the angle of incidence from 60º to 75º to analyze the optical properties of the deposited graphene films. The obtained Tan(Ψ) plot reveals distinct peaks at 3.4 eV and 4.6 eV. The peak at 3.4 eV corresponds to electronic transitions in the silicon substrate, while the peak at 4.6 eV is attributed to the characteristic optical response of graphene.

The 4.6 eV peak is associated with the $\pi \rightarrow \pi^*$ electronic transitions in graphene, which arise due to interband absorption. This feature is a well-known signature in ellipsometry studies of graphene and provides insight into its electronic structure and thickness. The presence of a strong silicon-related peak suggests that the graphene layer is relatively thin, allowing significant optical contributions from the underlying substrate. Further analysis, including fitting ellipsometric data with an appropriate optical model, can help determine the precise thickness and optical constants (n, k) of the graphene films.

We have successfully achieved the direct growth of single, bi-, and multilayer graphene on a silicon substrate. However, the uniformity of the deposited films was limited, with significant variations in coverage and thickness. To address this issue, Plasma-Enhanced Chemical Vapor Deposition (PECVD) was employed as an alternative growth technique. Compared to Hot-Wire Chemical Vapor Deposition (HWCVD), PECVD offers a lower growth rate, which allows for better control over film thickness and layer uniformity. The plasma-assisted

decomposition of precursors in PECVD enables more controlled nucleation and growth, reducing random variations in graphene coverage. This approach is expected to enhance film consistency while maintaining the desired layer characteristics.

5.2.2 Growth of multi-layer Graphene on Silicon substrate by PECVD

For our samples in series 1, Fig. 5.8 shows the CPD mapping, AFM and FESEM images of the films. Nearly uniform CPD is obtained for all the films, indicating that the films are compositionally uniform. When the H_2 flow rate is reduced from 80 sccm to 40 sccm, the average contact potential difference (CPD) decreases, leading to an increase in the work function from 4.25 eV to 4.42 eV. In plasma-enhanced chemical vapor deposition (PECVD), hydrogen (H_2) plays a pivotal role in facilitating graphene growth by managing defect density, eliminating surplus carbon, and influencing doping characteristics. When the H_2 flow rate is high (80 sccm), excess hydrogen increases n-type doping and defect formation, leading to a lower work function of 4.25 eV and a higher contact potential difference (CPD). In contrast, reducing the H_2 flow rate to 40 sccm minimizes defects and weakens n-type doping, bringing the Fermi level closer to the Dirac point. This adjustment enhances the work function to 4.42 eV while reducing the CPD, aligning with research findings that limited hydrogen exposure enhances graphene's crystallinity and optimizes its intrinsic electronic properties.[13, 22-24]

The average rms roughness and average height for these films were also calculated using AFM image. It is observed that the average height of the films changes with deposition condition, no significant difference in rms roughness is observed. The observed average CPD, work function, RMS roughness and average height for these films are listed in Table 5.6. The FESEM images (Fig. 3) reveal that the surface of the deposited films on the silicon substrate is highly uniform, with no evidence of pinholes or cracks. Such a smooth and uniform surface morphology is crucial for achieving optimal performance in solar cell applications.

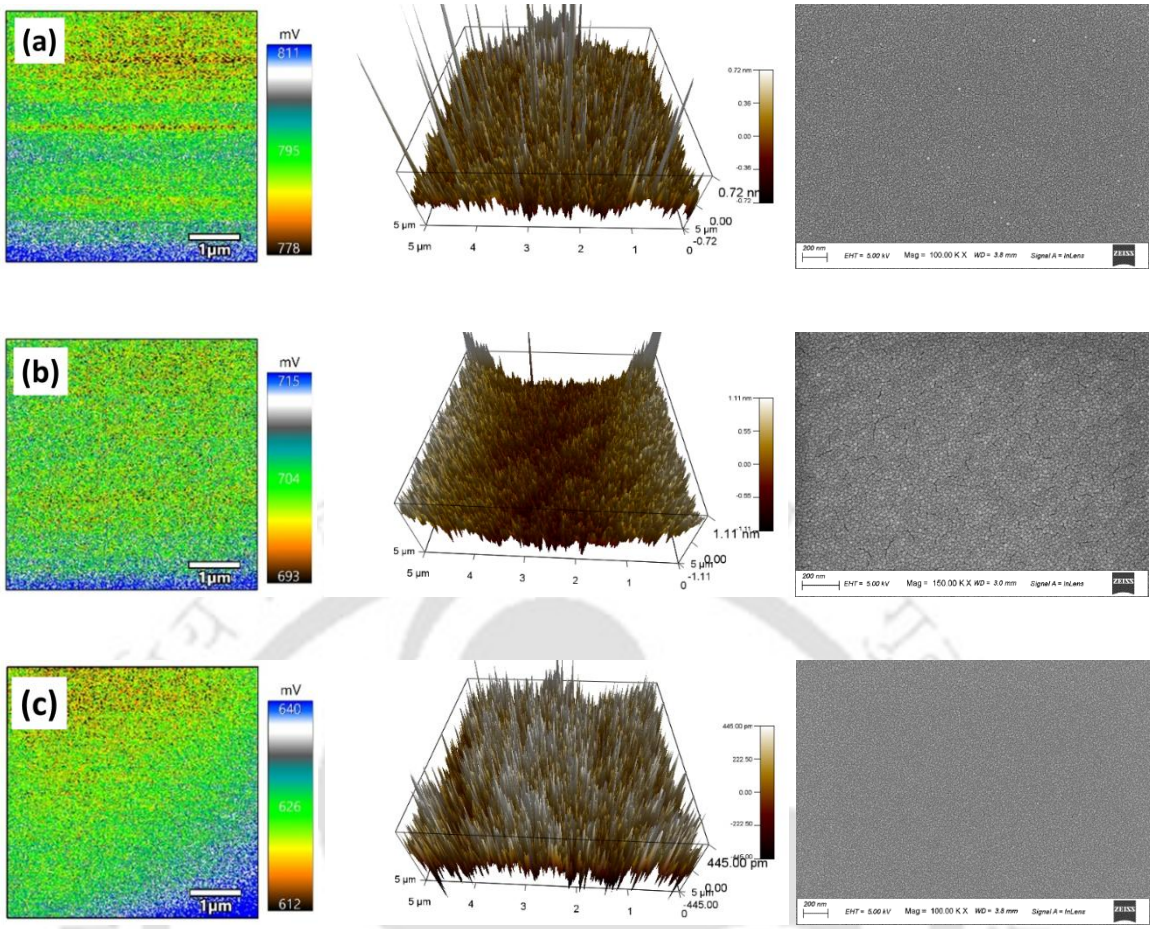

Fig. 5.8: CPD mapping, AFM images, and FESEM images of as-grown graphene film by PECVD (a) MP260 (H_2=80sccm, CH_4=10sccm), (b) MP261 (H_2=60sccm, CH_4=10sccm), (c) MP262 (H_2=40sccm, CH_4=10sccm)

Table 5.6: AFM and KPFM parameters of series 1 graphene film by PECVD

Sample	H_2 flow rate (sccm)	CH_4 flow rate (sccm)	Avg. CPD (mV)	Work function (eV)	Rms roughness (nm)	Average height (nm)	$\frac{CH_4}{CH_4 + H_2}$
MP260	80	10	794.93	4.25	0.23	0.366	0.11
MP261	60	10	704.34	4.37	0.25	0.71	0.143
MP262	40	10	625.68	4.42	0.22	0.67	0.2

Fig. 5.8 shows the FESEM images and rms roughness profile obtained from AFM images. These images shows uniformity in all the films. It is also evident from table 5.5 that all the films are uniform in nature with rms roughness values ranging from 0.22-0.25 nm.

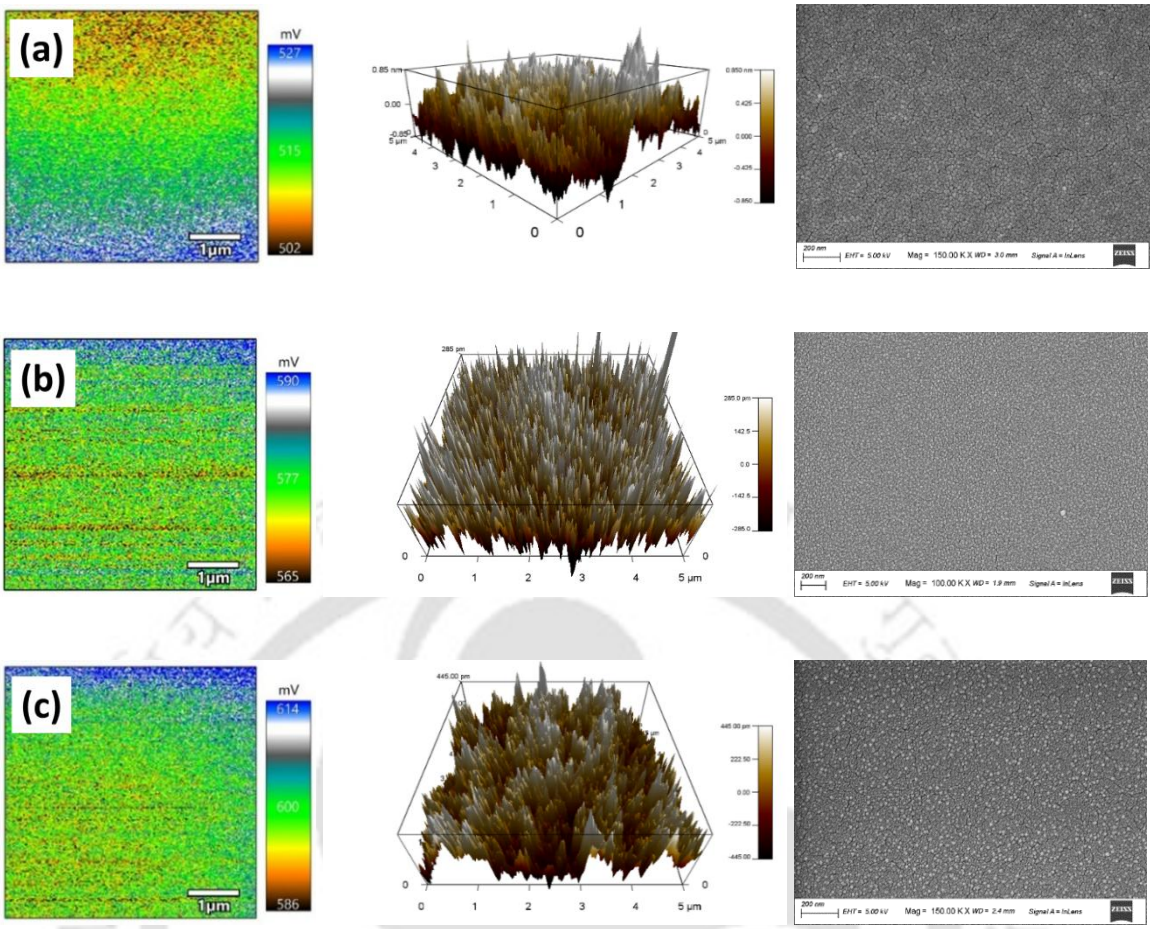

Fig. 5.9: CPD mapping, AFM images, and FESEM images of as-grown graphene film by PECVD (a) MP263 (H_2=80sccm, CH_4=7sccm), (b) MP264 (H_2=60sccm, CH_4=7sccm), (c) MP265 (H_2=40sccm, CH_4=7sccm)

Table 5.7: AFM and KPFM parameters of series 2 graphene film by PECVD

Sample	H_2 flow rate (sccm)	CH_4 flow rate (sccm)	Avg. CPD (mV)	Work function (eV)	Rms roughness (nm)	Average height (nm)	$\frac{CH_4}{CH_4+H_2}$
MP263	80	7	600.10	4.44	0.43	1.05	0.09
MP264	60	7	577.22	4.46	0.14	0.35	0.10
MP265	40	7	514.68	4.52	0.19	0.337	0.15

Further in series 2, the methane flow rate was reduced from 10 sccm to 7 sccm. To analyze the effect of the CH_4/H_2 ratio, the H_2 flow rate was systematically varied from 80 sccm to 60 sccm and then to 40 sccm, allowing a detailed investigation of its influence on work function modulation (Table 5.7 and Fig. 5.9). Since the dissociation mechanism of methane in PECVD

is highly sensitive to the hydrogen flow rate or the flux of hydrogen radicals/ions, variations in these parameters play a crucial role in influencing the growth process.

When the hydrogen flow rate is decreased from 80sccm to 60sccm, the work function simultaneously increases from 4.44eV to 4.52eV. It is also observed that when we compare the results of both the series from table 5.6 and 5.7, at each value of hydrogen flow rate, the work function of the films has increased when the methane flow rates are decreased from 10sccm to 7sccm. FESEM images (Fig. 5.9) shows uniform and crack free deposition in all the films.

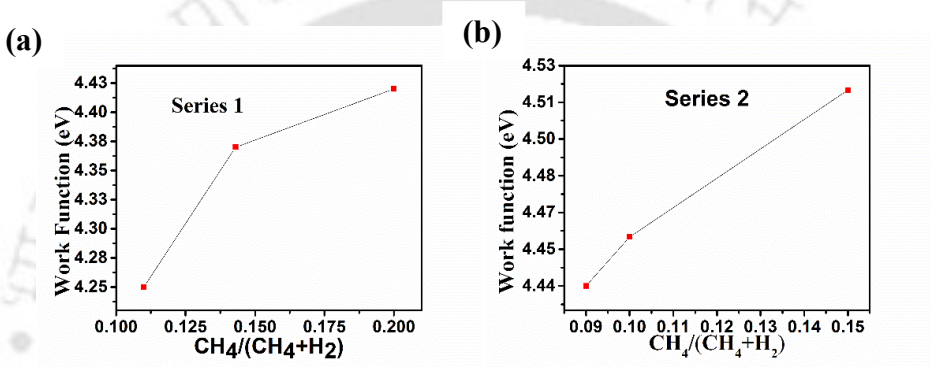

Fig 5.10: Variation in work function with respect to $CH_4/(CH_4+H_2)$ for (a) series 1 (b) series 2

Fig. 5.10 (a,b) demonstrates the impact of the $CH_4/(CH_4+H_2)$ ratio on graphene's work function, showing that a higher CH_4 fraction correlates with an increased work function. At lower CH_4 concentrations (i.e., higher H_2 flow), hydrogen plays a pivotal role in etching amorphous carbon, reducing defects, and passivating dangling bonds, which collectively result in lower work function values. Conversely, as the CH_4 fraction increases, the carbon supply becomes dominant, promoting higher sp^2 carbon content and diminishing hydrogen-induced doping, thereby enhancing the intrinsic work function. Furthermore, reduced hydrogen concentration mitigates p-type doping effects (from hydrogen or oxygen species), enabling the work function of graphene to approach its pristine value

As high work function is desired for our requirement, structural characterizations for MP265 film with work function of 4.52eV was performed. Fig 5.11 (a) shows signature of distorted

single layered Graphene in the raman spectra. Here the ratio of 2D/G peak is more than 2 symbolizing single layered graphene but with lots of distortions as the G peak is almost equal to D peak.

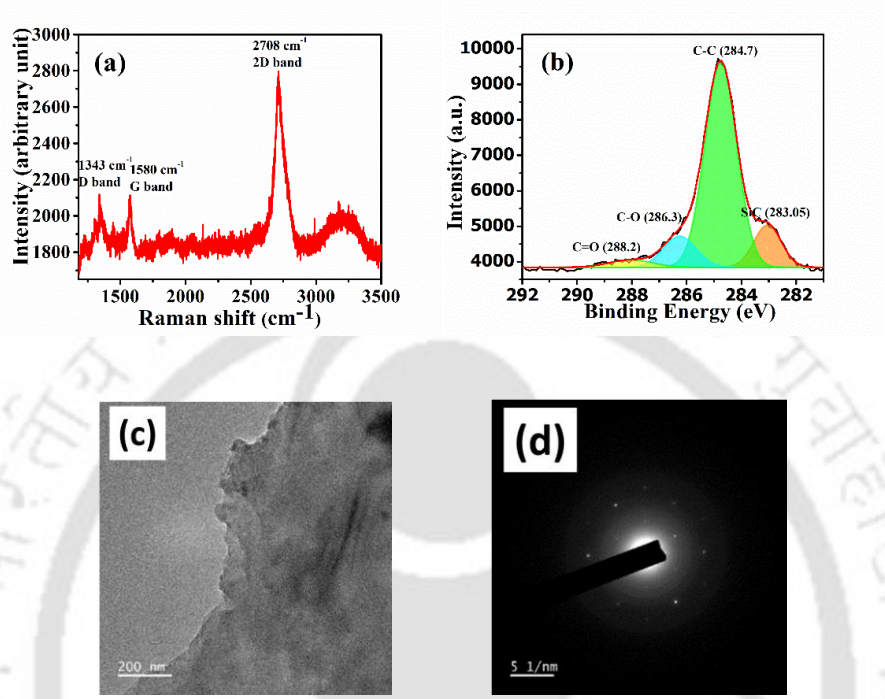

Fig. 5.11: (a) Raman spectra, (b) XPS Spectra, (c) FETEM image, and (d) SAED pattern of MP 265

XPS measurements were performed for graphene films (Fig. 5.11(b)). The first peak is assigned to the sp^2 hybridized C atoms in the graphene positioned at ~284.7 eV, the peaks located at ~286.2 eV and 288.2eV are associated with oxygen content in the sample. The C 1s XPS spectrum represents graphene or graphene-like layers on the sample surface, with the presence of oxygen primarily attributed to contamination of the graphene layer. The C 1s spectrum of graphene grown on a silicon substrate features multiple peaks corresponding to distinct chemical states. The primary assigned to sp^2 C–C peak (284.7 eV) signifies graphitic carbon and serves as a reference for charge correction. The C–Si peak (~284.6–285.0 eV) indicates interfacial bonding between graphene and silicon. A minor SiC formation is also observed at approximately 283.05 eV. Oxygen-related peaks, including C–O (~286.0–286.5 eV), C=O

(~288.2 eV).[25, 26] From Fig. 5.11 (c,d), we can see that the graphene film is multi-layered and the SAED pattern shows the hexagonal pattern of different planes conforming the formation of crystalline pristine quality graphene.

The observed work function variations from 4.38 to 4.92 eV for HWCVD samples and 4.25 to 4.54 eV for PECVD samples, achieved by varying methane and hydrogen flow rates, can be attributed to the distinct deposition mechanisms inherent to each technique. In HWCVD, high-temperature thermal dissociation leads to a broader distribution of carbon species, resulting in varied graphene quality and doping levels, which contribute to the wider work function range. The relatively lower hydrogen flow in HWCVD influences surface states and defect densities, further impacting the work function. Conversely, PECVD offers enhanced process control through plasma-assisted dissociation, where higher hydrogen flow facilitates the generation of active radicals for controlled etching and defect minimization, leading to a more consistent and narrower work function range. These findings underscore the greater sensitivity of HWCVD to gas flow variations and the superior stability of PECVD in achieving reproducible work function values. [6, 27]

As per our requirements for the solar cells, higher work function with uniform film and less defects is required. For this, MP265 with 4.52 eV work function is favorable MP265 thin film is used for the device fabrication.

5.3. Device results

The fabricated device structure is Ag/Gr/n-Si/Ag and Ag/ITO/Gr/n-Si/Ag. The Schematic diagram for the device is mentioned in fig. 5.1. The corresponding band diagram is shown in fig. 5.12.

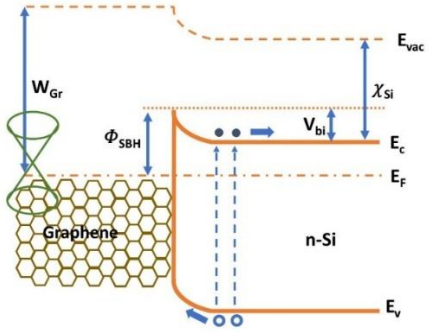

Fig. 5.12: Energy band schematics of graphene/n-silicon Schottky junction solar cell under light conditions. The arrow indicates direction of holes and electrons. [28]

An energy band diagram of electron-hole pair generation and the Schottky barrier connection under light is displayed in Fig. 5.12. The formation of Schottky barrier and depletion zone at the interface is a result of the difference between the Fermi levels of graphene and n-type silicon. A built-in potential creates and separates electron-hole pairs when light is present While holes migrate to the p-type graphene side, electrons move towards the back contact at the n-type silicon. Consequently, a photocurrent is produced.

The device were made with and without ITO layer on top of Graphene layer (Fig. 5.13(a,b)). Fig 7(a) shows the J-V curve of the device without ITO. The device displayed J_{sc} values of 0.63 mA/cm^2 with V_{oc} of 0.3 V. The V_{oc} of ~0.3 V is quite promising when compared to values reported for directly grown graphene/silicon (Gr/Si) solar cells, where plasma exposure, interface disorder, and native oxide often limit V_{oc} to 0.1-0.4 V.[29-31] In this work, the presence of a thin native SiO_2 layer on the silicon substrate prior to graphene growth also introduces an additional tunneling barrier, which can impede carrier transport.[32] Although graphene coverage in our samples is uniform, the native oxide layer combined with plasma-induced surface modifications can lead to imperfect band alignment and reduce effective barrier height, contributing to the observed S-shaped J-V curve. [28] [31, 33]The poor J_{sc} value can be the result of poor minority charge carrier collection. To address this issue, an ITO layer was introduced on top of graphene layer to enhance the minority carrier collection probability.

This layer is deposited using RF sputtering technique. The influence of ITO has a very positive impact on the performance parameters of the device. As a result, the J_{sc} and efficiency values improved significantly to 25.52 mA/cm^2 and 1 %. However, the drop in V_{oc} from 0.3V to 0.13V is because of the damage sustained by the graphene layer during the sputtering of the ITO film on top of graphene layer. Sputtering damage of graphene layer may occur when high energy particles or plasma bombard the surface of graphene layer. These bombardment of high energy particles can also lead erosion or complete removal of graphene layer. This removal or erosion of the graphene layer can lead to decrease in shunt resistance values and hence finally negatively affecting the V_{oc} (open circuit voltage) of the device.[31, 32] However, ITO serves a dual purpose in the device. It must be sufficiently transparent to allow maximum light penetration to the absorber layer (silicon) while also being conductive enough to facilitate efficient minority charge carrier collection at the graphene/ITO interface. Additionally, ITO also acts as an antireflection coating, minimizing reflection losses and further enhancing light absorption. [34-36]These contributes to the observed increase in J_{sc} of the device.

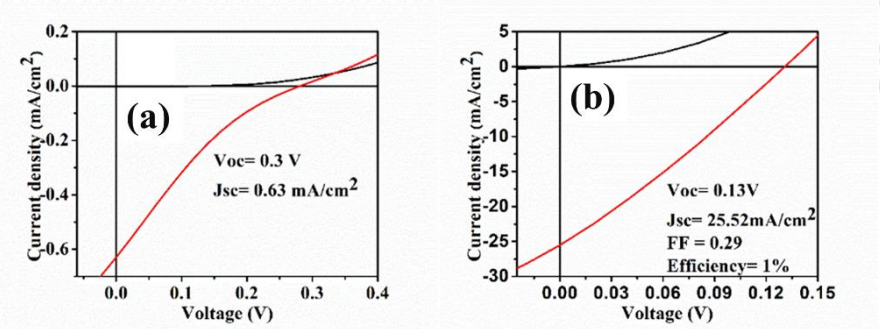

Fig. 5.13: J-V characteristics of fabricated solar cells

To summarize, without ITO we have got the V_{oc} of 0.3V but our J_{sc} value is low, so to improve it we have fabricated our device with ITO as TCO at the top and observed a significant increase in the J_{sc} value from 0.63 to 25.52mA/cm^2 with the V_{oc} of 0.13V and efficiency of 1%.

5.4. Conclusion

In this work, we report synthesis of large area Graphene sheets by HWCVD (Hot Wire Chemical Vapor Deposition) and PECVD (Plasma Enhanced Chemical Vapor Deposition) with tunable work function based on number of layers of Graphene. The work function has been measured through surface potential mapping by KPFM. We have observed the work function variation from 4.38 to 4.92eV for samples deposited by HWCVD and 4.25 eV to 4.54 eV by varying the gas flow rates of methane and hydrogen for samples deposited by PECVD. The Solar cell has been fabricated with device structure Ag/ITO/Gr/n-Si/Ag having efficiency of 1 %, current density of 25.52 mA/cm^2, V_{oc} of 0.13V and[30] FF of 0.29.

5.5. References

1. Rodriguez-Villanueva, S., F. Mendoza, B.R. Weiner, and G. Morell, *Graphene Film Growth on Silicon Carbide by Hot Filament Chemical Vapor Deposition.* Nanomaterials (Basel), 2022. **12**(17).
2. Zhang, L., H. Shen, X. Jiang, B. Qian, Z. Han, and H. Hou, *Influence of annealing temperature on the properties of polycrystalline silicon films formed by rapid thermal annealing of a-Si:H films.* Journal of Materials Science: Materials in Electronics, 2013. **24**(11): p. 4209-4212.
3. Shustin, E.G., *Preparation of Graphene: Deposition and Annealing.* Russian Microelectronics, 2024. **53**(5): p. 439-446.
4. Abubakar, Y., *Graphene Synthesis by Chemical Vapour Deposition (CVD): A Review on Growth Mechanism and Techniques.* International Journal of Engineering Research and, 2019. **V8**(05).
5. Lee, B., W. Chu, and W. Li, *Effects of Process Parameters on Graphene Growth Via Low-Pressure Chemical Vapor Deposition.* Journal of Micro and Nano-Manufacturing, 2020. **8**(3).
6. Meskinis, S., A. Lazauskas, S. Jankauskas, A. Guobiene, and R. Gudaitis, *Advancing Graphene Synthesis: Low-Temperature Growth and Hydrogenation Mechanisms Using Plasma-Enhanced Chemical Vapor Deposition.* Molecules, 2024. **30**(1).
7. Melitz, W., J. Shen, A.C. Kummel, and S. Lee, *Kelvin probe force microscopy and its application.* Surface Science Reports, 2011. **66**(1): p. 1-27.
8. Kumari, J., J.S. Bhardwaj, Rahul, and P. Agarwal, *Oxygen Plasma Treatment of Thermally Evaporated MoO3-x Films: An Approach to Tune the Work Function.* ACS Applied Electronic Materials, 2023. **5**(8): p. 4103-4113.
9. Maiti, P., P. Guha, R. Singh, J.K. Dash, and P.V. Satyam, *Optical band gap, local work function and field emission properties of MBE grown β-MoO3 nanoribbons.* Applied Surface Science, 2019. **476**: p. 691-700.
10. Kowalczyk, D.A., M. Rogala, K. Szalowski, D. Belic, P. Dabrowski, P. Krukowski, I. Lutsyk, M. Piskorski, A. Nadolska, P. Krempinski, M. Le Ster, and P.J. Kowalczyk, *Two-Dimensional Crystals as a Buffer Layer for High Work Function Applications: The Case of Monolayer MoO3.* ACS Appl Mater Interfaces, 2022. **14**(39): p. 44506-44515.
11. Robinson, J.T., J. Culbertson, M. Berg, and T. Ohta, *Work Function Variations in Twisted Graphene Layers.* Sci Rep, 2018. **8**(1): p. 2006.

12. Rut'kov, E.V., E.Y. Afanas'eva, and N.R. Gall, *Graphene and graphite work function depending on layer number on Re.* Diamond and Related Materials, 2020. **101**.
13. Garg, R., N.K. Dutta, and N.R. Choudhury, *Work Function Engineering of Graphene.* Nanomaterials (Basel), 2014. **4**(2): p. 267-300.
14. Dai, C.-Y., W.-C. Wang, C.-A. Tseng, F.-C. Ding, Y.-T. Chen, and C.-C. Chen, *Spatial Confinement Approach Using Ni to Modulate Local Carbon Supply for the Growth of Uniform Transfer-Free Graphene Monolayers.* The Journal of Physical Chemistry C, 2020. **124**(42): p. 23094-23105.
15. Sharma, I., G.S. Papanai, S.J. Paul, and B.K. Gupta, *Partial Pressure Assisted Growth of Single-Layer Graphene Grown by Low-Pressure Chemical Vapor Deposition: Implications for High-Performance Graphene FET Devices.* ACS Omega, 2020. **5**(35): p. 22109-22118.
16. Vlassiouk, I., M. Regmi, P. Fulvio, S. Dai, P. Datskos, G. Eres, and S. Smirnov, *Role of hydrogen in chemical vapor deposition growth of large single-crystal graphene.* ACS Nano, 2011. **5**(7): p. 6069-76.
17. Zhang, X., J. Ning, X. Li, B. Wang, L. Hao, M. Liang, M. Jin, and L. Zhi, *Hydrogen-induced effects on the CVD growth of high-quality graphene structures.* Nanoscale, 2013. **5**(18): p. 8363-6.
18. Li, X., W. Cai, J. An, S. Kim, J. Nah, D. Yang, R. Piner, A. Velamakanni, I. Jung, E. Tutuc, S.K. Banerjee, L. Colombo, and R.S. Ruoff, *Large-area synthesis of high-quality and uniform graphene films on copper foils.* Science, 2009. **324**(5932): p. 1312-4.
19. Bertran-Serra, E., S. Rodriguez-Miguel, Z. Li, Y. Ma, G. Farid, S. Chaitoglou, R. Amade, R. Ospina, and J.-L. Andujar, 2023.
20. Li, Z., P. Wu, C. Wang, X. Fan, W. Zhang, X. Zhai, C. Zeng, Z. Li, J. Yang, and J. Hou, *Low-temperature growth of graphene by chemical vapor deposition using solid and liquid carbon sources.* ACS Nano, 2011. **5**(4): p. 3385-90.
21. Sandoz-Rosado, E., W. Page, D. O'Brien, J. Przepioski, D. Mo, B. Wang, T.-T. Ngo-Duc, J. Gacusan, M.W. Winter, M. Meyyappan, R.D. Cormia, S. Takahashi, and M.M. Oye, *Vertical graphene by plasma-enhanced chemical vapor deposition: Correlation of plasma conditions and growth characteristics.* Journal of Materials Research, 2013. **29**(3): p. 417-425.
22. Xu, H., Q. Wang, H. Xiao, X. Li, X. Su, M. Tang, L. Chen, and S. Li, *In situ preparation of C-SiC (x) O (y) coatings with controllable composition on continuous oxygen-enriched SiC fibres.* RSC Adv, 2019. **9**(3): p. 1319-1326.
23. Wu, S., D. Huang, H. Yu, S. Tian, A. Malik, T. Luo, and G. Xiong, *Molecular understanding of the effect of hydrogen on graphene growth by plasma-enhanced chemical vapor deposition.* Phys Chem Chem Phys, 2022. **24**(17): p. 10297-10304.
24. Yoon, T., Q. Wu, D.J. Yun, S.H. Kim, and Y.J. Song, *Direct tuning of graphene work function via chemical vapor deposition control.* Sci Rep, 2020. **10**(1): p. 9870.
25. Susi, T., D.J. Mowbray, M.P. Ljungberg, and P. Ayala, *Calculation of the graphene C1score level binding energy.* Physical Review B, 2015. **91**(8).
26. Tai, L., D. Zhu, X. Liu, T. Yang, L. Wang, R. Wang, S. Jiang, Z. Chen, Z. Xu, and X. Li, *Direct Growth of Graphene on Silicon by Metal-Free Chemical Vapor Deposition.* Nanomicro Lett, 2018. **10**(2): p. 20.
27. Kim, H., E. Kim, W.-J. Lee, and J. Jung, *Effects of hydrogen in the cooling step of chemical vapor deposition of graphene.* Electronic Materials Letters, 2013. **9**(4): p. 417-420.
28. Rehman, M.A., S.B. Roy, I. Akhtar, M.F. Bhopal, W. Choi, G. Nazir, M.F. Khan, S. Kumar, J. Eom, S.-H. Chun, and Y. Seo, *Thickness-dependent efficiency of directly grown graphene based solar cells.* Carbon, 2019. **148**: p. 187-195.
29. Kong, X., L. Zhang, B. Liu, H. Gao, Y. Zhang, H. Yan, and X. Song, *Graphene/Si Schottky solar cells: a review of recent advances and prospects.* RSC Adv, 2019. **9**(2): p. 863-877.
30. Rehman, M.A., S.B. Roy, D. Gwak, I. Akhtar, N. Nasir, S. Kumar, M.F. Khan, K. Heo, S.-H. Chun, and Y. Seo, *Solar cell based on vertical graphene nano hills directly grown on silicon.* Carbon, 2020. **164**: p. 235-243.
31. Chen, Q., J. Kim, M. Choi, and S. Jeon, *Advancing solar energy applications with graphene: the potential of minimally oxidized graphene.* Nano Converg, 2025. **12**(1): p. 30.

32. Li, X., H. Zhu, K. Wang, A. Cao, J. Wei, C. Li, Y. Jia, Z. Li, X. Li, and D. Wu, *Graphene-on-silicon Schottky junction solar cells.* Adv Mater, 2010. **22**(25): p. 2743-8.
33. Bae, S., H. Kim, Y. Lee, X. Xu, J.S. Park, Y. Zheng, J. Balakrishnan, T. Lei, H.R. Kim, Y.I. Song, Y.J. Kim, K.S. Kim, B. Ozyilmaz, J.H. Ahn, B.H. Hong, and S. Iijima, *Roll-to-roll production of 30-inch graphene films for transparent electrodes.* Nat Nanotechnol, 2010. **5**(8): p. 574-8.
34. Zahid, M.A., M.Q. Khokhar, Y. Kim, and J. Yi, *Utilization of CaF2/ITO Double-Layer Anti-Reflective Coating for Increasing the Efficiency in Rear Emitter SHJ Solar Cells.* Crystal Research and Technology, 2022. **57**(8).
35. Zahid, M.A., M.Q. Khokhar, S. Park, S.Q. Hussain, Y. Kim, and J. Yi, *Influence of Al2O3/IZO double-layer antireflective coating on the front side of rear emitter silicon heterojunction solar cell.* Vacuum, 2022. **200**.
36. Singh, A., R. Ghosh, and P. Agarwal, *Selection of materials and optimization of antireflection coatings for silicon solar cells using Sentaurus TCAD.* Journal of Materials Science: Materials in Electronics, 2023. **34**(15).

Chapter 6

Role of doping concentration, thickness of intrinsic layer in Graphene-Silicon heterojunction Solar Cells

Graphene possesses the unique characteristic of a zero band-gap, allowing its electrical properties to be widely tuned by varying the number of layers or through p- or n-type doping with different materials. Due to its high electrical conductivity, excellent optical transmittance, and zero band-gap, graphene can function as both an electron and hole extraction layer. Inspired by these properties, this study simulates the Ag/ITO/n-Graphene/a-Si:H/c-Si(p)/Ag heterojunction solar cell using the AFORS-HET (Automat FOR Simulation of HETero-structures) software under AM1.5 illumination with a power density of 100 mW/cm². AFORS-HET employs one-dimensional semiconductor equations, incorporating Shockley-Reed-Hall statistics and the Lambert–Beer law for optical modelling.

The research focuses on optimizing the doping level of graphene and the thickness of intrinsic amorphous silicon (a-Si:H) to enhance cell efficiency. The thickness of the a-Si:H

layer is varied from 0 to 20 nm, while the n-type doping concentration of graphene is adjusted from 1×10^{10} cm^{-3} to 1×10^{20} cm^{-3}. The study systematically explores the independent effects of these parameters on overall device performance. Key performance indicators such as the band diagram and quantum efficiency variations are analyzed to identify the optimal configuration. The highest power conversion efficiency achieved is 18.59%, with an open-circuit voltage (V_{oc}) of 611.8 mV, short-circuit current density (J_{sc}) of 37.04 mA/cm^2, and a fill factor (FF) of 82.03%, corresponding to an a-Si:H layer thickness of 5 nm, a single-layer graphene structure, and an n-type doping concentration of 1×10^{20} cm^{-3}. This study underscores the potential of graphene-silicon heterojunction solar cells and highlights the importance of fine-tuning graphene doping levels and a-Si:H thickness for optimal efficiency.

6.1 Simulation details

In AFROS-HET, the drift-diffusion model solver and Metal-Schottky junction is utilized to describe an equivalent model for Gr/Si (2D/3D structure) heterojunction solar cell. The basic structure of graphene/silicon heterojunction solar cell considered in AFORS-HET is: Ag/ITO/n-Graphene/a-Si:H/c-Si(p)/Ag as shown in fig. 6.1.

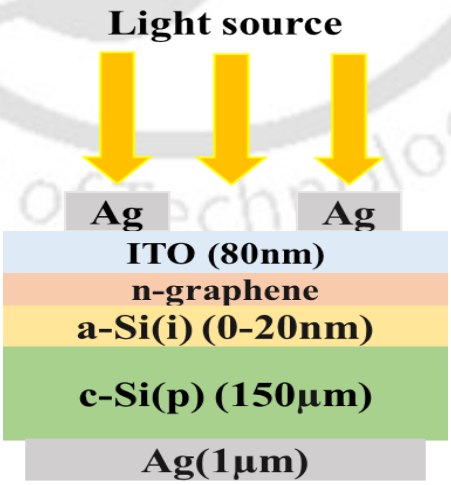

Fig 6.1: Schematic device structure of Graphene Silicon heterostructure solar cell

In the proposed device structure, firstly device structure Ag/ITO/n-Graphene/c-Si(p)/Ag is simulated. Afterwards, an intrinsic a-Si:H layer is used for surface defect passivation at graphene silicon interface. Here, Indium Tin Oxide (ITO) is used as an transparent conducting oxide front contact, while Silver is used as back contact for the device. Parameters used for different layers in the device structure are summarized in table 6.1. The C-Si(p) wafer used for simulation is considered to be of high quality with single donor type defect density in the order of 1E10 cm^{-3} at the mid of the bandgap with an electronic capture cross section of 1E−14 cm^2 for both electrons and holes.[1]

Table 6.1: Simulation Parameters

Input Parameters	n-Graphene	a-Si:H(i)	c-Si(p)
Dielectric constant	6.9	11.9	11.9
Electron affinity (eV)	4.2	3.9	4.05
Bandgap (eV)	0	1.72	1.17
Optical bandgap (eV)	0	1.72	1.17
Effective conduction band density (cm^{-3})	1×10^{22}	1×10^{22}	2.8×10^{19}
Effective valence band density (cm^{-3})	1×10^{22}	1×10^{22}	2.8×10^{19}
Effective electron mobility (cm^2/Vs)	1×10^{5}	20	1107
Effective hole mobility (cm^2/Vs)	10	5	424.6
Doping Concentration Acceptors (cm^{-3})	0	0	2×10^{15}
Doping Concentration Donors (cm^{-3})	1×10^{15} to 1×10^{20}	1000	0
Thickness (cm)	3.35×10^{-8}	5×10^{-7} to 2×10^{-6}	0.015
Mobility of electron, μ_n ($cm^2V^{-1}s^{-1}$)	200,000	20	1450
Mobility of hole, μ_p ($cm^2V^{-1}s^{-1}$)	50	5	450

The localized defects state distribution of a-Si:H(i) were assumed to be an acceptor-like state and donor-like state ,modeled by Urbach tail and gaussian mid-gap state[2] and the parameters are tabulated in table 6.2.

Table 6.2: Localized defects state distribution of a-Si:H(i)

Defects	a-Si:H(i)
Defect density at conduction (valence) band edge (cm^{-3} eV^{-1})	10^{20} (10^{20})
Urbach energy for conduction (valence) bandtail (eV)	0.03 (0.045)
σ_e (σ_h) for conduction bandtail (cm^2)	10^{-17}(10^{-15})
σ_e (σ_h) for valence bandtail (cm^2)	10^{-15}(10^{-17})
Gaussian density of states (cm^{-3} eV^{-1})	10^{16}
Gaussian peak energy for donor/acceptor (eV)	0.8 (1.0)
Standard deviation of Gaussian for donor/acceptor (eV)	0.15 (0.15)
Position of defect for donor/acceptor	E_C-0.75 eV E_V + 0.75 eV
σ_e (σ_h) for donor-like Gaussian states (cm^2)	10^{-14} (10^{-15})
σ_e (σ_h) for acceptor-like Gaussian states (cm^2)	10^{-15} (10^{-14})
Interface defect density	Gr/ p-Si(c)
defect density	1E12 (continuous distribution)

6.2 Working principle

In our device structure, the n-Gr/c-Si(p) interface forms a Schottky junction as shown in Fig 6.2, where a built-in potential develops within the depletion region at the p-Si side.[3] Under illumination, incident photons generate electron-hole (e-h) pairs within the silicon substrate. The built-in electric field at the Schottky junction facilitates the separation of these photogenerated carriers: electrons are swept towards the n-type graphene, while holes drift towards the bulk p-type c-Si region. This carrier separation contributes to the photovoltaic effect, enabling current generation in the device.[4-8] [9-12] If the graphene and semiconductor interface barrier is ideally Schottky in nature, then a Schottky barrier developed at the depletion region of silicon wafer. This Schottky barrier or barrier height (Φ_{bi}) is given by:

$$\Phi_{bi} = \Phi_G - \Phi_{Si} = \Phi_G - \chi_{Si} - kT\ ln(N_A/N_V) \qquad 6.1[13]$$

where Φ_G is the graphene work function, Φ_{Si} is the silicon work function, and χ_{Si} is the electron

affinity of silicon. Here, N_A is the acceptor doping concentration, and N_V is the effective valence band density of p-cSi.

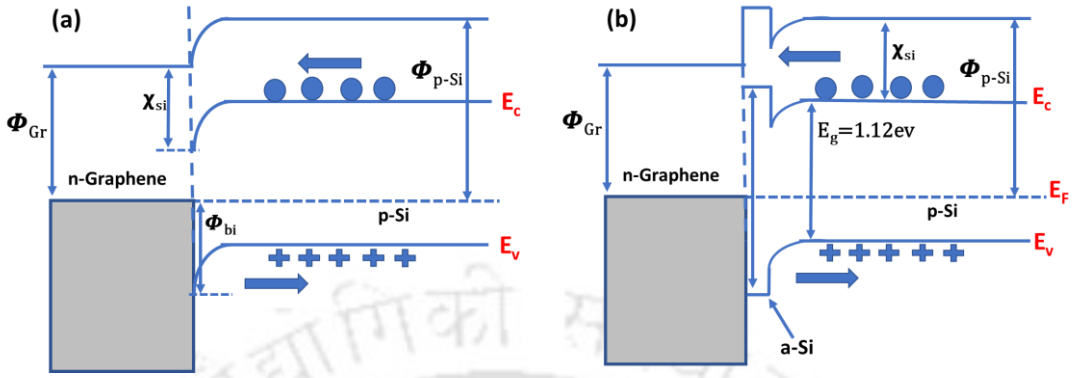

Fig 6.2: Schematic band diagram of (a) Graphene- Silicon heterojunction and (b) Graphene/a-Si(i) /p-Si(c) heterojunction

As carrier density increases in their respective regions, a photovoltage (V_{oc}) is generated under open-circuit conditions. When the device is short-circuited, these excess carriers are collected at the respective electrodes, producing a short-circuit current (J_{sc}) in the external circuit. Doping graphene with nitrogen (N) or phosphorus (P) has been reported to reduce its work function (Φ_G) from 3.8 eV to 3.6 eV[14]. The increasing donor concentration (N_D) decreases the Fermi level of graphene as well as enhances the carrier density and improves the conductivity.[5, 15] However, doping does not introduce band gap in the graphene layer.

6.3 Results and Discussion

6.3.1 Influence of amorphous silicon layer for surface passivation

In graphene/silicon heterostructures, an a-Si:H layer is crucial for passivating interface defects and minimizing recombination losses. The significant lattice mismatch and structural differences between graphene and p-Si(c) necessitate this layer. To ensure efficient carrier transport, the a-Si:H layer must be thin enough to allow minority carriers to tunnel through it. But excess thickness may absorb some photons resulting in degradation of the device performance.[16-18] To optimize the thickness of i-layer, simulation studies were performed by varying the i-layer thickness from 5-20nm. For comparison, simulations were also done for

no a-Si:H layer. The doping for graphene layer was kept 10^{20} cm^{-3} for this series.

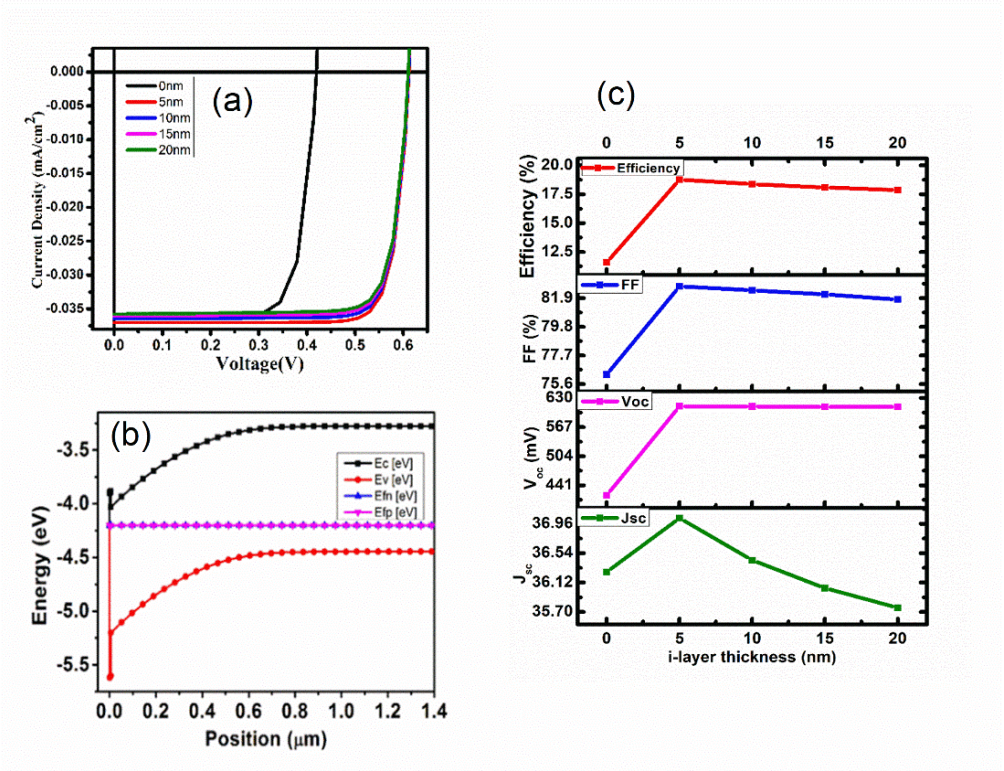

Fig 6.3: (a) J-V characteristics of graphene/silicon heterojunction solar cell with intrinsic layer thickness variation (b) Band diagram for graphene/silicon hetero-structure with intrinsic layer (c) Variation in device parameters with i-layer thickness

From the table 6.3 and J-V characteristics (fig. 6.3(a)) shown below, without intrinsic layer, the V_{oc} is 419.6 mV, J_{sc} is 36.27 mA/cm^2, FF is 76.30% and efficiency 18%. But after introducing i-layer, the open circuit voltage increased by ~200mV (fig. 6.3(c)). The i-layer has passivated interface defects resulting in lowering the recombination of photo-generated carriers and hence drastically improving the open circuit voltage. Further, when i-layer thickness is varied from 5-20nm, slight decrease in J_{sc}, V_{oc}, FF and hence in efficiency is observed. (fig. 6.3(c)). This is due to absorption of incident photons in a-Si:H layer resulting in degradation of the device performance. The best efficiency is obtained when absorber layer thickness is kept 5nm. For 5nm, V_{oc} is 611.8 mV, J_{sc} is 37.04 mA/cm^2, FF is 82.03% and efficiency 18.59%.

The J-V Characteristics of device structure, with intrinsic layer thickness variation is shown in Fig 6.3 (a).

Table 6.3: Summary of device performance by varying i-layer thickness

i-layer thickness (nm)	J_{sc} (mA/cm^2)	V_{oc} (mV)	FF (%)	Efficiency (%)
0	36.27	419.6	76.30	11.61
5	37.04	611.8	82.03	18.59
10	36.44	611.3	81.8	18.22
15	36.04	610.7	81.51	17.94
20	35.76	610.7	81.18	17.73

6.3.2 Influence of n-type doping concentration of Graphene on device performance

Since graphene is a zero band-gap material, it can be doped by n as well as p-type to vary the work function.[19-23] Here we have simulated the device structure Ag/ITO/n-Graphene/a-Si:H/c-Si(p)/Ag by doping graphene with n-type and using p-type silicon layer. The thickness of a-Si:H is 5nm for this series. We varied the doping concentration of Graphene from 1×10^{10} cm^{-3} to 1×10^{20} cm^{-3}.

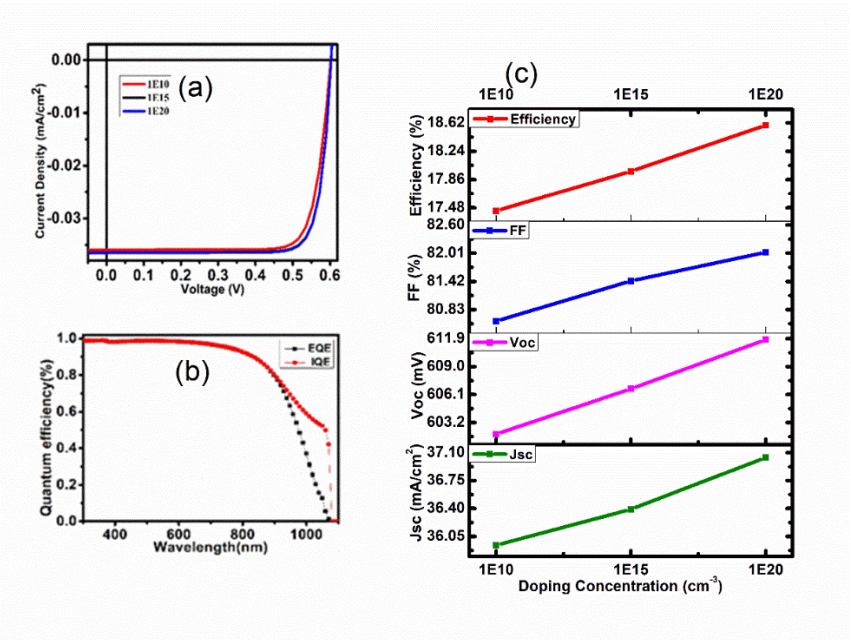

Fig 6.4: a) J-V characteristics of graphene/silicon heterojunction with graphene layer (n-type) doping variation (b) Quantum efficiency of best cell (c) Variation of device parameters with doping concentration

Fig 6.4(a) shows the J-V characteristic of n-graphene/a-Si:H/c-Si(p) structure for different

doping concentration of graphene layer A slight change in J_{sc}, V_{oc}, and FF is observed when doping concentration of graphene is increased. This increase in the performance parameters with increasing doping is because of the enhancement in n type conductivity of graphene layer.[24, 25] The External Quantum Efficiency (EQE) is shown in figure 6.4 (b). The EQE usually depends on factors such as graphene quality, doping, interface engineering, and device structure. The peak EQE falls between 95% to 85% in the visible range (400-800 nm), In the near-infrared region (800-1100 nm), EQE drops abruptly due to silicon's absorption characteristics. The best power conversion efficiency is obtained when the doping concentration is 1×10^{20} cm^{-3}. For this, V_{oc} is 611.8 mV, J_{sc} is 37.04 mA/cm^2, FF is 82.03% and efficiency 18.59% (table 6.4).

Table 6.4: n-type doping variation for graphene in the device structure

Doping Concentration (cm^{-3})	J_{sc} (mA/cm^2)	V_{oc} (mV)	FF (%)	Efficiency (%)
1×10^{10}	35.94	602	80.59	17.44
1×10^{15}	36.39	606.7	81.43	17.97
1×10^{20}	37.04	611.8	82.03	18.59

6.4. Conclusion

The basic structure of graphene/silicon heterojunction solar cell considered here is: Ag/ITO/n-Graphene/a-Si:H/c-Si(p)/Ag. we varied the thickness of a-Si:H i-layer from 0 to 20nm, the n-type doping concentration of Graphene from $1 \times 10^{10}cm^{-3}$ to $1 \times 10^{20}cm^{-3}$ to get the optimized results. Corresponding to that, we studied the band diagram and Quantum efficiency etc. The best power conversion efficiency obtained is 18.59% where the V_{oc} is 611.8 mV, J_{sc} is 37.04 mA/cm^2 and FF is 82.03% corresponding to i-layer thickness 5nm, single layer graphene and n-type doping concentration of $1 \times 10^{20}cm^{-3}$. The values are significantly high compared to reported simulation results so far. [9, 12, 14]

6.5. References

1. Deka, H., A. Sunaniya, and P. Agarwal, *Design and Simulation of Highly Efficient One-Sided Short PIN Diode Silicon Heterojunction Solar Cell.* IEEE Journal of Photovoltaics, 2022. **12**(1): p. 204-212.
2. Oppong-Antwi, L., S. Huang, Q. Li, D. Chi, X. Meng, and L. He, *Influence of defect states and fixed charges located at the a-Si:H/c-Si interface on the performance of HIT solar cells.* Solar Energy, 2017. **141**: p. 222-227.
3. Sze, S.M. and K.K. Ng, *Physics of Semiconductor Devices*. 2006.
4. Patel, K. and P.K. Tyagi, *Multilayer graphene as a transparent conducting electrode in silicon heterojunction solar cells.* AIP Advances, 2015. **5**(7): p. 077165.
5. Liu, X., X.W. Zhang, Z.G. Yin, J.H. Meng, H.L. Gao, L.Q. Zhang, Y.J. Zhao, and H.L. Wang, *Enhanced efficiency of graphene-silicon Schottky junction solar cells by doping with Au nanoparticles.* Applied Physics Letters, 2014. **105**(18): p. 183901.
6. Meng, J.-H., X. Liu, X.-W. Zhang, Y. Zhang, H.-L. Wang, Z.-G. Yin, Y.-Z. Zhang, H. Liu, J.-B. You, and H. Yan, *Interface engineering for highly efficient graphene-on-silicon Schottky junction solar cells by introducing a hexagonal boron nitride interlayer.* Nano Energy, 2016. **28**: p. 44-50.
7. Liu, X., X.W. Zhang, J.H. Meng, Z.G. Yin, L.Q. Zhang, H.L. Wang, and J.L. Wu, *High efficiency Schottky junction solar cells by co-doping of graphene with gold nanoparticles and nitric acid.* Applied Physics Letters, 2015. **106**(23): p. 233901.
8. Pu, D., M.A. Anwar, J. Zhou, R. Mao, X. Pan, J. Chai, F. Tian, H. Wang, H. Hu, and Y. Xu, *Enhanced photovoltaic effect in graphene–silicon Schottky junction under mechanical manipulation.* Applied Physics Letters, 2023. **122**(4): p. 041102.
9. Ye, Y. and L. Dai, *Graphene-based Schottky junction solar cells.* Journal of Materials Chemistry, 2012. **22**(46): p. 24224.
10. Li, X., H. Zhu, K. Wang, A. Cao, J. Wei, C. Li, Y. Jia, Z. Li, X. Li, and D. Wu, *Graphene-on-silicon Schottky junction solar cells.* Adv Mater, 2010. **22**(25): p. 2743-2748.
11. Kong, X., L. Zhang, B. Liu, H. Gao, Y. Zhang, H. Yan, and X. Song, *Graphene/Si Schottky solar cells: a review of recent advances and prospects.* RSC Adv, 2019. **9**(2): p. 863-877.
12. Dell'Olio, F., M. Palmitessa, and C. Ciminelli, *Modeling and Design of a New Flexible Graphene-on-Silicon Schottky Junction Solar Cell.* Electronics, 2016. **5**(4): p. 73.
13. Mao, L.F., H. Ning, Z.L. Huo, and J.Y. Wang, *Physical Modeling of Gate-Controlled Schottky Barrier Lowering of Metal-Graphene Contacts in Top-Gated Graphene Field-Effect Transistors.* Sci Rep, 2015. **5**: p. 18307.
14. Kuang, Y., Y. Liu, Y. Ma, J. Xu, X. Yang, X. Hong, and J. Feng, *Modeling and Design of Graphene GaAs Junction Solar Cell.* Advances in Condensed Matter Physics, 2015. **2015**: p. 1-7.
15. Bulusheva, L.G., V.E. Arkhipov, K.M. Popov, V.I. Sysoev, A.A. Makarova, and A.V. Okotrub, *Electronic Structure of Nitrogen- and Phosphorus-Doped Graphenes Grown by Chemical Vapor Deposition Method.* Materials (Basel), 2020. **13**(5): p. 1173.
16. Panigrahi, J. and V.K. Komarala, *Progress on the intrinsic a-Si:H films for interface passivation of silicon heterojunction solar cells: A review.* Journal of Non-Crystalline Solids, 2021. **574**: p. 121166.
17. Ge, J., Z.P. Ling, J. Wong, T. Mueller, and A.G. Aberle, *Optimisation of Intrinsic a-Si:H Passivation Layers in Crystalline-amorphous Silicon Heterojunction Solar Cells.* Energy Procedia, 2012. **15**: p. 107-117.
18. Wong, H., J. Zhang, J. Liu, and M.A. Anwar, *On the Current Conduction and Interface Passivation of Graphene–Insulator–Silicon Solar Cells.* Nanomaterials, 2025. **15**(6): p. 416.
19. Talukder, N., Y. Wang, B.B. Nunna, and E.S. Lee, *Nitrogen-doped graphene nanomaterials for electrochemical catalysis/reactions: A review on chemical structures and stability.* Carbon, 2021. **185**: p. 198-214.
20. Wu, Y., W. Jiang, Y. Ren, W. Cai, W.H. Lee, H. Li, R.D. Piner, C.W. Pope, Y. Hao, H. Ji, J. Kang, and R.S. Ruoff, *Tuning the doping type and level of graphene with different gold*

configurations. Small, 2012. **8**(20): p. 3129-3136.
21. Meng, X., S. Tongay, J. Kang, Z. Chen, F. Wu, S.-S. Li, J.-B. Xia, J. Li, and J. Wu, *Stable p- and n-type doping of few-layer graphene/graphite.* Carbon, 2013. **57**: p. 507-514.
22. Lee, H., K. Paeng, and I.S. Kim, *A review of doping modulation in graphene.* Synthetic Metals, 2018. **244**: p. 36-47.
23. Dey, A., P. Ghosh, J. Bowen, N.S.J. Braithwaite, and S. Krishnamurthy, *Engineering work function of graphene oxide from p to n type using a low power atmospheric pressure plasma jet.* Phys Chem Chem Phys, 2020. **22**(15): p. 7685-7698.
24. Alavi, M., R. Rahimi, Z. Maleki, and M. Hosseini-Kharat, *Improvement of Power Conversion Efficiency of Quantum Dot-Sensitized Solar Cells by Doping of Manganese into a ZnS Passivation Layer and Cosensitization of Zinc-Porphyrin on a Modified Graphene Oxide/Nitrogen-Doped TiO(2) Photoanode.* ACS Omega, 2020. **5**(19): p. 11024-11034.
25. Jun, G.H., S.H. Jin, B. Lee, B.H. Kim, W.-S. Chae, S.H. Hong, and S. Jeon, *Enhanced conduction and charge-selectivity by N-doped graphene flakes in the active layer of bulk-heterojunction organic solar cells.* Energy & Environmental Science, 2013. **6**(10): p. 3000.

Chapter 7

Conclusion and future scope

This chapter summarizes the work presented in the present thesis providing a detailed and technical exploration of the synthesis, characterization, and application of graphene-based materials, focusing on their potential for energy storage and optoelectronic applications. The study starts with the synthesis of graphene oxide (GO) through the Modified Hummers method, followed by its reduction to reduced graphene oxide (r-GO) using thermal annealing and chemical reduction techniques. The chapter compares the effects of these reduction methods on the materials' properties. Further boron doping is done in GO and r-GO using boric acid as boron source. The electrochemical performance is evaluated through cyclic voltammetry (CV) to determine the materials' suitability for supercapacitor applications. Afterwards, the growth of high-quality graphene films on nickel substrate using Hot wire Chemical Vapor Deposition (HWCVD) is discussed in detail, particularly the optimization of deposition parameters and its impact on number of layers of graphene. The transfer process of graphene film from nickel foil to silicon substrate is also discussed. Later, the challenges of direct graphene growth on silicon

substrates using Hot Wire CVD (HWCVD) and Plasma Enhanced CVD (PECVD) without metal catalysts are addressed. Here the work function variation of directly grown graphene films based on deposition parameters are studied. Graphene-silicon heterojunction solar cells are fabricated for optimised graphene film. Later, the photovoltaic performance of Graphene-silicon heterojunction solar cells is studied using AFORS-HET software.

7.1. Conclusion

- The synthesis of graphene oxide (GO) from graphite was successfully achieved using the Modified Hummers method, providing a reliable base material for subsequent reduction and modification processes.
- Two reduction methods were explored for converting GO into reduced graphene oxide (r-GO) - thermal annealing and chemical reduction using hydrazine hydrate.
- Thermal reduction (T-rGO) exhibited superior properties compared to chemical reduction (C-rGO), particularly in terms of specific surface area and electrical conductivity. T-rGO had a surface area of 74.78 m^2/g and conductivity of 2.28 S/cm, while C-rGO had a surface area of 17.35 m^2/g and conductivity of 0.049 S/cm. Despite the enhanced properties, the high temperature required for thermal reduction remains a significant challenge for large-scale and cost-effective production.
- Bulk synthesis of boron-doped reduced graphene oxide (B-rGO and r-BGO) was achieved using boric acid (H_3BO_3) as a boron source. The doping was confirmed using XRD, Raman spectroscopy, EDAX, and FETEM techniques.
- Electrochemical studies revealed that r-BGO exhibited the highest capacitance (326.56 ± 3.1 F/g), outperforming B-rGO (170.46 ± 2 F/g), GO (137.88 ± 1.8 F/g), and r-GO (108.85

± 1.6 F/g). This demonstrated the effectiveness of boron doping before reduction in enhancing charge storage properties.

- High-quality graphene was successfully grown on nickel substrates using Hot Wire CVD (HWCVD) which varied from bi-layer to multi-layer graphene. However, further transfer of graphene film from nickel to silicon substrate introduced breaking of graphene film and introduction of impurities in it. Since the deposition rate of HWCVD is high, the number layers increased with deposition time and decreased with increase in hydrogen dilution of methane due to better dissociation of methane with increase in hydrogen. A decrease in the number of graphene layers with increasing annealing temperature is observed, which may be attributed to the diffusion of carbon atoms into the nickel substrate.
- The direct growth of graphene on silicon substrates without metal catalysts using PECVD and HWCVD was explored. This approach solves challenges associated with the transfer process of graphene film from metal substrate to silicon, offering new opportunities for semiconductor applications.
- The work function of graphene films was tuned by adjusting the number of layers and deposition parameters. This optimization is crucial for integrating graphene into various electronic devices, including solar cells.
- The work function has been measured through surface potential mapping by KPFM. We have observed the work function variation from 4.38 to 4.92eV for samples deposited by HWCVD and 4.25 eV to 4.54 eV by varying the rf power and gas flow rates of methane and hydrogen for samples deposited by PECVD.
- The Solar cell has been fabricated with device structures Ag/Gr/n-Si/Ag and Ag/ITO/Gr/n-Si/Ag. Without ITO we have got the V_{oc} of 0.3V but our J_{sc} value is low, so to improve it we have fabricated our device with ITO as TCO at the top and observed a significant

increase in the J_{sc} value from 0.63 to 25.52mA/cm^2 with the V_{oc} of 0.13V and efficiency of 1% demonstrating the potential for integrating graphene in solar energy applications.

- Simulations using AFORS-HET software indicated a simulated efficiency of 18.59% under optimized conditions, providing insights into the potential for improving graphene-based solar cell efficiency.

- The difference between the simulated (~18%) and experimental (~1%) efficiencies mainly reflects the idealised assumptions in AFORS-HET. The simulator treats graphene using a simplified flat-band model and cannot capture its Dirac dispersion, or Fermi-level shifts, nor the interfacial defects and oxide-mediated barriers present in the real device. As a result, the simulations represent a nearly "perfect" interface, whereas the fabricated cell operates with non-ideal band alignment and carrier transport, explaining the observed performance gap. Reducing native-oxide effects, improving surface passivation and using tools that better describe graphene should narrow this discrepancy.

7.2. Scope and future work

- Optimizing Doping Strategies: Future research should focus on refining doping concentrations and techniques to enhance graphene's performance. This includes incorporating additional heteroatoms such as nitrogen and phosphorus to improve electronic and electrochemical properties.

- Improving Graphene Transfer Methods: While this study employed polymer-assisted transfer techniques, challenges like polymer residue contamination and film breakage were encountered. To address these issues, future work can explore electrochemical delamination for cleaner transfers with minimal residue or dry PDMS-assisted stamping to reduce mechanical damage and improve graphene integrity.

- Flexible Substrate Integration: Developing reliable processes for transferring directly grown graphene onto flexible substrates such as PET or polyimide to enable applications in wearable electronics, foldable displays, and stretchable sensors.
- Growth Process Optimization: Fine-tuning critical growth parameters including temperature, precursor gas composition, pressure, and rf power to achieve uniform, high-quality graphene films with controlled thickness and minimal defects. Additionally, exploring in-situ doping of graphene (p- and n-type) during growth can help tailor its electronic, optical, and electrochemical properties for specific applications.
- Enhancing Graphene-Silicon Solar Cell Efficiency: Continued research in interface engineering, surface passivation, and optimized doping strategies is essential to improving the efficiency and stability of graphene-silicon heterojunction solar cells.
- Optimizing ITO Deposition: Implementing thermal evaporation for Indium Tin Oxide (ITO) deposition can help prevent damage to graphene films, by rf-sputtering for improved structural integrity and performance in graphene-silicon heterojunction solar cells.
- Future work should explore the diverse uses of graphene-based materials for applications such as in flexible electronics, sensors, and biomedical devices.

List of publications

*1 **Jai Shree Bhardwaj**, Anterdipan Singh, Pratima Agarwal, "Work function tuning of directly grown multi-layer graphene on silicon by PECVD and fabrication of Ag/ITO/Gr/n-Si/Ag solar cell" ***Diamond and Related Materials*** (2025) 155.

*2 **Jai Shree Bhardwaj**, Pratima Agarwal, "Synthesis of Boron doped reduced Graphene Oxide as electrode material for Supercapacitor Applications" ***Journal of Material Science: Materials in Electronics 35*** (2024) 1944.

*3 **Jai Shree Bhardwaj**, Pratima Agarwal, "Role of doping concentration, thickness of intrinsic layer and number of layers of Graphene in Graphene-Silicon heterojunction Solar Cells" ***Materials Today Proceedings*** (2023) (in press).

*4 **Jai Shree Bhardwaj**, Pilik Basumatary, Ankit Kumar Singh, "Comparative study of chemically and thermally reduced graphene oxide based on their specific surface area" ***AIP Conference Proceedings*** (2020) 2220, 020157.

5 Niharika Gogoi, **Jai Shree Bhardwaj**, and Pratima Agarwal, "Study of laser induced micro-structural changes in reduced graphene oxide", ***AIP Conference Proceedings*** (2019) 2091, 020023.

6 Rahul, Juhi Kumari, **Jai Shree Bhardwaj**, Pratima Agarwal, "Work function tuning of thermally evaporated V2Ox films using UV-Ozone treatment and its influence on V2Ox/c-Si(n) solar cells" ***Materials Science in Semiconductor Processing*** (2025) 109217.

7 Juhi Kumari, **Jai Shree Bhardwaj**, Rahul, Pratima Agarwal, "Oxygen Plasma Treatment of thermally evaporated MoO3-x films: an approach to tune the work function" ***ACS applied electronic materials*** (2023) 5, 4103-4113.

*Related to this thesis work

List of papers presented in International/National conferences

1. **Jai Shree Bhardwaj** and Pratima Agarwal, *"Synthesis of Boron-doped reduced Graphene Oxide as electrode materials for Supercapacitor Application",* 34th ICDCM (International Conference on Diamond and Carbon Materials) 2024, Hilton, Germany Sep 01-05, 2024

2. **Jai Shree Bhardwaj** and Pratima Agarwal, *"Work function tunning of directly grown multi-layer Graphene on Silicon by PECVD and fabrication of Ag/ITO/Gr/n-Si/Ag Solar cell",* 34th ICDCM (International Conference on Diamond and Carbon Materials) 2024, Hilton, Germany Sep 01-05, 2024

3. **Jai Shree Bhardwaj** and Pratima Agarwal, *"Graphene as emitter layer in Silicon heterojunction Solar Cell",* ISSMD (International Symposium on Semiconductor Materials and Devices) 2022, KIIT Bhubaneshwar, Dec 16-18, 2022

4. **Jai Shree Bhardwaj** and Pratima Agarwal,*"Role of number of layers and n-type doping concentration of Graphene in ITO/n-Graphene/a-Si:H/C-Si(p)/Ag heterojunction Solar Cells",* NERC (North-East Research Conclave) 2022, IIT Guwahati, Assam, May 20-22, 2022

5. **Jai Shree Bhardwaj** and Pratima Agarwal,*"Role of number of layers and n-type doping concentration of Graphene in ITO/n-Graphene/a-Si:H/C-Si(p)/Ag heterojunction Solar Cells",* IWPSD (XXIst International Workshop of Semiconductor Devices) 2021, IIT Delhi, December 14-17, 2021

6. **Jai Shree Bhardwaj** and Pratima Agarwal,*"Role of doping concentration, thickness of intrinsic layer and number of layers of Graphene in Graphene-Silicon heterojunction Solar Cells",* RAISE (Recent advances and Innovations in Solar Energy) 2021, IIT Madras, Chennai, December 2-3, 2021

7. **Jai Shree Bhardwaj**, Pilik Basumatary, Ankit Kumar Singh and Pratima Agarwal *"Comparitive study of chemically and thermally reduced graphene oxide on the basis of their specific surface area, structural and electrical properties",* ICC 2019 International Conference on Condensed Matter and Applied Physics)., Govt. Engineering College, Bikaner, Rajasthan, October 14-15,2020

List of workshops/webinars attended

1. *"One day national webinar on optical and electrical modelling and simulation for organic semiconductor devices using setfos"*, School of Studies in Electronics and Photonics & Institute of Renewable Energy Technology and Management in association with Impulse technology, Gurgaon, Haryana, February, 5, 2021

2. *"Patent Protection for Innovation Driven Educational Institute",* Turnip Innovations, August 29, 2020

3. *"Advances in Functional Materials",* Department of Physics, School of Applied Science, KIIT University, August 26-28, 2020

4. *"2-Day Familiarization Workshop on Nanofabrication Technologies",* NIT Silchar, Assam, January 28-29, 2019

5. *"National Workshop on NEMS/MEMS and Theranostic Devices",* Centre for Excellence in Nanoelectronics & Theranostic Devices under the aegis of Centre for Nanotechnology, Indian Institute of Technology Guwahati, 26th-28th February, 2018

6. *"One-Day Workshop on Vacuum Technology and Its application In Optical Science"*, SPIE IITG Student Chapter and Pfeiffer Vacuum in association with Department of Physics, IIT Guwahati, 19th August, 2017